

# NAVAL POSTGRADUATE SCHOOL MONTEREY, CALIFORNIA



19960223 077

## THESIS

**CALIBRATION OF A COHERENT ACOUSTIC  
SEDIMENT PROFILER (CASP)  
AND ANALYSIS OF SEDIMENT  
DISTRIBUTION FROM DUCK94**

by

Karen Marie Kohanowich

September 1995

Thesis Advisor:  
Co-Thesis Advisor:

Timothy P. Stanton  
Edward B. Thornton

Approved for public release; distribution is unlimited.

DTIC QUALITY INSPECTED 3

REPORT DOCUMENTATION PAGE			Form Approved OMB No. 0704-0188	
Public reporting burden for this collection of information is estimated to average 1 hour per response, including the time for reviewing instruction, searching existing data sources, gathering and maintaining the data needed, and completing and reviewing the collection of information. Send comments regarding this burden estimate or any other aspect of this collection of information, including suggestions for reducing this burden, to Washington Headquarters Services, Directorate for Information Operations and Reports, 1215 Jefferson Davis Highway, Suite 1204, Arlington, VA 22202-4302, and to the Office of Management and Budget, Paperwork Reduction Project (0704-0188) Washington DC 20503.				
1. AGENCY USE ONLY (Leave blank)		2. REPORT DATE September 1995		3. REPORT TYPE AND DATES COVERED Master's Thesis
4. TITLE AND SUBTITLE CALIBRATION OF A COHERENT ACOUSTIC SEDIMENT PROFILER (CASP) AND ANALYSIS OF SEDIMENT DISTRIBUTION FROM DUCK94			5. FUNDING NUMBERS	
6. AUTHOR(S) Karen Marie Kohanowich				
7. PERFORMING ORGANIZATION NAME(S) AND ADDRESS(ES) Naval Postgraduate School Monterey CA 93943-5000			8. PERFORMING ORGANIZATION REPORT NUMBER	
9. SPONSORING/MONITORING AGENCY NAME(S) AND ADDRESS(ES)			10. SPONSORING/MONITORING AGENCY REPORT NUMBER	
11. SUPPLEMENTARY NOTES The views expressed in this thesis are those of the author and do not reflect the official policy or position of the Department of Defense or the U.S. Government.				
12a. DISTRIBUTION/AVAILABILITY STATEMENT Approved for public release; distribution is unlimited.			12b. DISTRIBUTION CODE	
13. ABSTRACT (maximum 200 words) The Coherent Acoustic Sediment Profiler (CASP) uses four acoustic beams at two frequencies (1.3 and 5.3 MHz) to measure the backscatter from sediments and infer concentrations in 1.68 cm bins to one meter range. It also measures three velocity components and sediment concentration in the same intersecting volume ( $O(1 \text{ cm}^3)$ ) at a sampling frequency of 36 Hz. Empirical calibration of the sediment profiling capability of the CASP has been performed with sediment sampled from the nearshore zone at Duck, N.C. The sediment is characterized by a lognormal distribution with a mean grain size diameter of 0.18 mm, and standard deviation of 1.2. The 1.3 MHz sonar measures sediment concentrations of $O(1 \times 10^{-4} \text{ kgm}^{-3})$ to $25 \text{ kgm}^{-3}$ , and the 5.3 MHz sonar measures concentrations of $O(1 \times 10^{-5} \text{ kgm}^{-3})$ to $8 \text{ kgm}^{-3}$ , both with an accuracy of 10%. A grain size discrimination capability, based on comparison of measurements by the two frequencies and the assumption of a lognormal sand size distribution, can detect variations of $\pm 0.05 \text{ mm}$ mean geometric radius between the calibration sand and the sediment measured in the field. Field data from a day characterized by narrow banded, nonlinear wave forcing during the DUCK94 experiment show that episodes of high sediment concentration correlate well with the maximum onshore velocities within 2 cm of the bottom, but decorrelate above this level. Data is ensemble averaged with a phase mapping technique to illustrate this correlation. Sediment flux calculations reveal strong shoreward transport at the boundary layer, and weaker seaward transport higher in the water column.				
14. SUBJECT TERMS acoustic calibration, sediment flux, acoustic backscatter, acoustic sediment flux probe			15. NUMBER OF PAGES 106	
			16. PRICE CODE	
17. SECURITY CLASSIFICATION OF REPORT Unclassified	18. SECURITY CLASSIFICATION OF THIS PAGE Unclassified	19. SECURITY CLASSIFICATION OF ABSTRACT Unclassified	20. LIMITATION OF ABSTRACT UL	



Approved for public release; distribution is unlimited.

**CALIBRATION OF A COHERENT ACOUSTIC SEDIMENT PROFILER (CASP) AND  
ANALYSIS OF SEDIMENT DISTRIBUTION FROM DUCK94**

Karen M. Kohanowich  
Lieutenant Commander, United States Navy  
B.S., Vanderbilt University, 1982

Submitted in partial fulfillment  
of the requirements for the degree of

**MASTERS OF SCIENCE IN METEOROLOGY  
AND PHYSICAL OCEANOGRAPHY**


from the

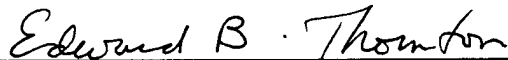
**NAVAL POSTGRADUATE SCHOOL  
September 1995**

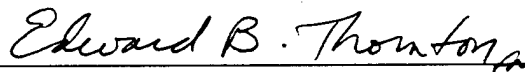
Author: \_\_\_\_\_

  
Karen M. Kohanowich

Approved by: \_\_\_\_\_

  
Timothy P. Stanton, Thesis Advisor

  
Edward B. Thornton, Second Reader

  
Robert H. Bourke, Chairman

Department of Oceanography



## ABSTRACT

The Coherent Acoustic Sediment Profiler (CASP) uses four acoustic beams at two frequencies (1.3 and 5.3 MHz) to measure the backscatter from sediments and infer concentrations in 1.68 cm bins to one meter range. It also measures three velocity components and sediment concentration in the same intersecting volume ( $O(1 \text{ cm}^3)$ ) at a sampling frequency of 36 Hz. Empirical calibration of the sediment profiling capability of the CASP has been performed with sediment sampled from the nearshore zone at Duck, N.C. The sediment is characterized by a lognormal distribution with a mean grain size diameter of 0.18 mm, and standard deviation of 1.2. The 1.3 MHz sonar measures sediment concentrations of  $O(1 \times 10^{-4} \text{ kgm}^{-3})$  to  $25 \text{ kgm}^{-3}$ , and the 5.3 MHz sonar measures concentrations of  $O(1 \times 10^{-5} \text{ kgm}^{-3})$  to  $8 \text{ kgm}^{-3}$ , both with an accuracy of 10%. A grain size discrimination capability, based on comparison of measurements by the two frequencies and the assumption of a lognormal sand size distribution, can detect variations of  $\pm 0.05 \text{ mm}$  mean geometric radius between the calibration sand and the sediment measured in the field. Field data from a day characterized by narrow banded, nonlinear wave forcing during the DUCK94 experiment show that episodes of high sediment concentration correlate well with the maximum onshore velocities within 2 cm of the bottom, but decorrelate above this level. Data is ensemble averaged with a phase mapping technique to illustrate this correlation. Sediment flux calculations reveal strong shoreward transport at the boundary layer, and weaker seaward transport higher in the water column.



## TABLE OF CONTENTS

I. INTRODUCTION .....	1
II. BACKGROUND THEORY .....	3
III. CALIBRATION .....	13
A. CASP DESCRIPTION .....	13
B. CALIBRATION THEORY .....	15
C. LABORATORY DESCRIPTION .....	19
1. Tank .....	19
2. Sediment .....	19
3. Procedure .....	21
4. Calibration Method Sensitivities .....	21
D. COEFFICIENT DETERMINATION .....	29
1. Aslope Coefficient .....	30
a. Calculation .....	30
b. 1.3 MHz Beam Attenuation .....	32
c. 5.3 MHz Beam Attenuation .....	45
2. $C_m$ Coefficient .....	45
a. Calculation .....	45
b. 1.3 MHz Mass .....	52
c. 5.3 MHz Mass .....	58
3. Full Optimization .....	61
E. GRAIN SIZE DISCRIMINATION .....	64
IV. FIELD DEPLOYMENT.....	71
A. SITE DESCRIPTION.....	71
B. SEDIMENT VS VELOCITY PHASE ANALYSIS.....	73
1. Background Theory.....	73
2. Phase Mapping Method.....	76
3. Concentration Data.....	79
4. Sediment Flux.....	85
C. GRAIN SIZE DISCRIMINATION.....	85



V. CONCLUSIONS.....	91
LIST OF REFERENCES.....	93
INITIAL DISTRIBUTION LIST.....	95

## ACKNOWLEDGEMENTS

Several people are responsible for the successful completion of this work. I would like to express my gratitude to Tim Stanton for his innovation and expertise. I would also like to thank Ed Thornton, not only for his attentive editing skills, but especially for giving me the opportunity to experience all aspects of nearshore science firsthand, from dragging scientific equipment across hot sand beaches to making international conference presentations. It is impossible to quantify the importance of the support I received from my mother, Harriet Longuet. Through it all, she was there to help me stay sane, balanced, and smiling.

## I. INTRODUCTION

The ability to model sediment transport in the surf zone is important to both scientists and engineers. For the military, it is an integral concern for the planning of amphibious operations. The mechanisms responsible for this sand transport under breaking waves, however, are still poorly understood. Among the most elusive problems is a satisfactory description of the small scale processes in the boundary layer, a deficiency in large part due to a lack of sufficient spatial and temporal resolution of sediment flux measurements.

A variety of instruments have been used to measure sediment concentrations in the surf zone, including physical collection of sand by "sand socks", direct siphoning, and optical and acoustic backscatter sensors. Physical collection techniques are limited in volume resolution, extremely limited in temporal resolution, and can disturb the in situ flow. Optical backscatter sensors (OBS) use scattered infrared radiation to measure suspended particle concentrations, and are often coupled with nearby current meter measurements to estimate flux. Although the temporal resolution is on the order of 10 Hz, the sample volume depends on the concentration of the sediments being measured, and as a result is poorly defined. The frame on which the instruments are mounted in the field also tends to perturb the flow, and the dual instrument technique cannot measure concentration and velocity in the same volume. Laser Doppler Velocity (LDV) measurements have been limited due to the high cost and complexity of the optical systems, and are usually limited to two velocity components. The sample volume of the LDV is only 100  $\mu\text{m}$  by 1 mm, which makes calibration for concentration profiling very difficult. Hot film anemometers provide extremely high resolution measurements of current speed within the bottom boundary layer, which makes them ideal for the study of turbulence length scales. They cannot sense direction of the flow or measure sediment concentrations, however, so they are of limited value in sediment flux studies. Acoustic instruments are able to make non invasive, high resolution measurements of sediment concentration. They have been operated successfully

in the field for several years (Hanes and Huntley (1986), Hay (1985), Thorne et al. (1991), Young (1982)) and typically profile sediment concentrations to a range of one meter with one cm and one second resolution. Sediment concentrations are retrieved from backscatter signals through empirical and/or analytical calibration techniques. Limitations in acoustic profiling systems occur at high sediment concentration as multiple scattering effects begin to occur. Single frequency instruments and collocated multiple frequency arrays have not provided a coincident velocity measurement.

The acoustic instrument used in this research was designed to address the above limitations (Stanton 1993). The Coherent Acoustic Sediment Probe (CASP) consists of a forward looking 1.3 MHz beam surrounded by three 5.3 MHz beam positioned so that the four beams intersect approximately 25 cm in front of the instrument. Using coherent doppler techniques, three-dimensional sediment velocities are measured in this intersection volume. A mean grain size estimate can be made by comparing the backscatter characteristics of sand from the two frequencies, so that violations of homogeneous sand size assumptions can be detected. As with previous instruments, sand concentration is also measured along the length of the beam. During the DUCK94 field experiment, the CASP was mounted on a hydraulic arm so that measurements could be made at various heights above the bed.

The background theory for use of acoustic techniques to measure nearshore sediment profiles is presented in Chapter II. Chapter III describes the calibration of all four sonars for measurement of sand concentrations, including analysis of concentration limits, and the capabilities of the grain size discriminator. Field data from a day characterized by narrow band wave forcing during DUCK94 is presented to demonstrate the capabilities of the CASP in Chapter IV. Utilizing a phase mapping technique, vertical sediment distribution is correlated with cross-shore velocity phase. The performance of the grain size discriminator in the field is also analyzed. Chapter V presents conclusions and areas of future research.

## II. BACKGROUND THEORY

Hay (1991) has shown that the pressure amplitude returned from an acoustic beam illuminating sand particles is directly related to the square root of the concentration of the particles. Other factors involved in this relation are the decay of the amplitude of the signal due to spreading of the sound beam, absorption of sound energy by the water, and attenuation of the signal due to scattering by particles. The measured acoustic power is also affected by the frequency and beam characteristics of the instrument, and by the composition, shape, and size distribution of the sand particles. There are essentially two approaches to inverting the signal return to provide sand concentration estimates. One is an empirical method, in which laboratory derived calibration coefficients describe the attenuation and the proportionality between the square of the acoustic pressure and the mass concentration. An assumption necessary for this method is that the size distribution of the sand used for the laboratory calibration is the same as that of the sand measured in the field. The second approach is analytical, and seeks to quantify the acoustic response in terms of particle behavior. This method uses a frequency dependent acoustic form factor, which accounts for phase shifts, grain diameter, and grain size distribution, to describe the total scattering cross section and scattering attenuation. The absolute backscatter sensitivity response of the system is then scaled to a given lognormal sediment mass concentration. The aim of the analytical approach has been to exploit frequency dependent acoustic characteristics in order to provide estimates of sand concentration assuming a lognormal distribution with an unknown mean grain size.

In the literature, Young, et al (1982), and Tamura and Hanes (1986) have used the empirical approach. Sheng and Hay (1988), Hay (1991), and Hay and Sheng (1992), have described a series of analytical models for multi-frequency backscatter and the response to variable mean grain size and lognormal distribution width. Thorne et al (1991, 1993) have used a combination of analytical and empirical techniques.

Young et al (1982) first calibrated a 3 MHz acoustic backscattering profilometer with three sizes of sand (120  $\mu\text{m}$ , 200  $\mu\text{m}$ , and 450  $\mu\text{m}$ ) in a laboratory tank. Concentrations of from .001 to 0.1  $\text{kg m}^{-3}$  were compared with profiles calculated using the relation :

$$I_s = K_o r^{-2} \exp(-0.6r) \quad (2.1)$$

where  $I_s$  is the backscattered intensity, or voltage squared,  $K_o$  is a reference concentration,  $r^{-2}$  corrects for spherical spreading with range  $r$ , and the fixed exponential term corrects for attenuation (attenuation coefficient = 1.2 db/m). Application of this formula to backscatter profiles confirmed a linear relationship for each of the sand sizes to accuracies within a factor of two, but underestimated the concentration of the largest sand particles.

Tamura and Hanes (1986) conducted further calibrations with the same 3 MHz instrument. They used full range and sifted samples of sand collected from their experiment site, Stanhope Lane, in concentrations of from 0.23  $\text{kg m}^{-3}$  to 5.7  $\text{kg m}^{-3}$ . They determined the semi-empirical relationship between the backscattered intensity  $I_b(y)$  and the sand concentration  $C(y)$ :

$$I_b(y) = AC(y) * \exp\left(-\int_y^0 (B_0 + B_1 C(y)) dy\right) \quad (2.2)$$

where the constants  $A$ , a function of the acoustic backscatter cross section,  $B_0$ , the loss due to water absorption, and  $B_1$ , the acoustic forward scattering cross section of the sediment water mixture, were determined from the laboratory experiments. The values for constants differed between the full range and sifted sand samples, indicating an acoustic response dependence on grain size and distribution. The calibration using the full range samples was corrected for observed attenuation along the beam and was accurate to within  $\pm 10\%$ .

Investigation into temporal resolution indicated that a time average of as short as 0.5 seconds still produced accurate concentration estimates. The analytical method strives to predict acoustic backscatter by sediment by describing all aspects of sound behavior in the presence of particles. The general acoustic equation, which describes pressure amplitude of sound waves in a sample volume, is:

$$P = P_0 \frac{r_0}{r} e^{-\alpha_w r} \quad (2.3)$$

where  $P_0$  is the pressure amplitude at the reference distance  $r_0$ ,  $r$  is the distance from the transducer to the detected volume, and  $\alpha_w$  is the attenuation due to water absorption. To apply this relation to the more specific problem of sand concentration measurement, factors are added to account for beam spreading, attenuation due to scattering by particles, loss through the measured volume, and the response of the acoustic beam itself to the particle population. Through such applications, Hay (1991) and Hay and Sheng (1992) derived the following acoustic model:

$$\bar{V} = S * \sqrt{\frac{M}{\rho_s}} * F[n(a), f_\infty(x)] * \sqrt{\sinh \frac{\xi}{\xi}} * e^{-2 \int_0^r \alpha_s dr} \quad (2.4)$$

where  $\bar{V}$  is the output voltage of the receiver, and  $S$  is a system constant, or sensitivity, which depends on the receiver directivity, lobe half width, reference range and output pressure. In their system, the time variable gain (TVG) of the receiver compensates for the  $r_0/r$  spreading loss and loss due to absorption by water,  $\alpha_w$ .  $M$  is the mass concentration in  $\text{kg m}^{-3}$ , and  $\rho_s$  is the particle density.  $F[n(a), f_\infty(x)]$  is an empirical function which includes the effects of a frequency dependent acoustic form factor,  $f_\infty(x)$ , and the size spectral density,  $n(a)$ . Here,  $x$  is the nondimensional particle radius,  $k_c a$ , where  $k_c$  is the wavenumber of the

sound wave in the fluid, and  $a$  is the equivalent radius of the particle. The  $\sqrt{\sinh \xi / \xi}$  term corrects for attenuation across the detected volume;  $\xi = c\tau(\alpha_w + \bar{\alpha}_s)$  where  $c$  is sound speed,  $\tau$  is pulse length, and  $\alpha_s$  is attenuation due to water and sediment, respectively. The exponential term,  $\exp[-2 \int_0^r \bar{\alpha}_s dr]$  describes the return path integrated loss due to scattering from particles,  $\bar{\alpha}_s$ .

Of the above variables, the sensitivity  $S$  can be measured in the laboratory for each instrument. The form factor and the attenuation due to scattering by particles are complex functions of the compressibility and density of the particles, fluid shape of the particles, and  $x$ . The form factor here describes the acoustic response of an irregularly shaped sand grain and was derived semi-empirically from the form factor for spherical quartz grains. This spherical form factor has been described by Faran (1962) as a function of wavenumber, particle radius, phase shift, and reflection angle, and by Gaunard and Uberall (1983) as a function of wavenumber, particle radius, the velocity of sound in water, compression and shear wave velocities of the sphere, and water and sphere densities. This form factor for spheres was translated into one for irregular particles first through a high pass model for backscattered intensity developed by Johnson (1977). This model uses a polynomial that fits backscatter behavior in the Rayleigh and geometric regions. Sheng and Hay (1988) expanded the high pass model, based on Faran's (1962) description, by including angular dependence, to give:

$$|f_{\infty}(\theta)| = \frac{K_f x^2}{(1 + K_f x^2)} \quad (2.5 \text{ a})$$

$$\text{where} \quad K_f = 2/3 |\gamma_k + \gamma_p \cos \theta| \quad (2.5 \text{ b})$$



$$\text{and} \quad \gamma_{\kappa} = \frac{(\kappa_s - \kappa_w)}{\kappa_w}, \quad \gamma_{\rho} = \frac{3(\rho_s - \rho_w)}{(2\rho_s + \rho_w)} \quad (2.5 \text{ c,d})$$

where  $\kappa_s$ ,  $\kappa_w$ ,  $\rho_s$ ,  $\rho_w$  are compressibility and density of sediment and water, respectively.

A semi-empirical fit to experimental measurements is given by Sheng (1991):

$$|f_{\infty}(x)| = \frac{1 + 1.25x^4}{1 + x^4} \sqrt{|f_{\infty}(x)_{rm}|^2} \quad (2.6)$$

Here,  $|f_{\infty}(x)_{rm}|$  is the theoretical form factor for a rigid, mobile (finite bulk density) spherical particle with the density of quartz (Hay and Mercer, 1985). The attenuation coefficient  $\alpha_s$  is described as

$$\alpha_s = \frac{N}{2} \Sigma_s \quad (2.7)$$

where  $N$  is the total number of particles, and  $\Sigma_s$  is the total backscatter cross section of the particles, which describes both scattering and absorption effects.  $\Sigma_s$  can be represented as an explicit function of the spherical form factor (Sheng and Hay 1988), or as a function of  $x$  and compressibility and density of water and sediment (Thorne et al 1993). The high pass model for the attenuation coefficient constructed by Sheng and Hay (1988) is expressed as:

$$\alpha_s \left( \frac{a\rho_s}{M} \right) = \frac{K_{\alpha} x^4}{[1 + \frac{4}{3} K_{\alpha} x^4 + \xi x^2]} \quad (2.8 \text{ a})$$

$$\text{where} \quad K_{\alpha} = \frac{(\gamma_{\kappa}^2 + \gamma_{\rho}^2/3)}{6} \quad (2.8 \text{ b})$$

and  $\xi$  is an adjustable constant  $\geq 1$ . The  $\xi x^2$  term improves the fit to the data between Rayleigh and geometric ranges. From the known values and from laboratory measured attenuation, the total cross section can be calculated, and then applied to the forward problem to determine attenuation in the field.

Hay (1991) used three frequencies (1, 2.25, and 5 MHz) to examine scattering behavior in the laboratory. To avoid nearfield complications, the instruments were aimed perpendicularly into a jet of sediment, and corrections were applied for the jet characteristics. Results for  $|f_{\infty}|$  calculations show very good agreement with theory at  $x < 1$ , but give values of  $|f_{\infty}(x)|$  higher than expected for  $x > 1$ . The curvature of the fit is somewhat similar to theory between  $1 < x < 2$ , but departs for  $x > 2$ . Values of  $\Sigma_s$  for sand particles was calculated using direct hydrophone measurements of sound propagating through the sediment plume. Although subject to statistical scatter, the data clearly fits the modified high pass model better than the rigid sphere theory. Also using the above semi-empirical expressions, Thorne et al (1993) found values of  $|f_{\infty}(x)|$  and  $\Sigma_s$  calculated from measurements to be 25% more than those predicted by theory.

The limits of the linear response of voltage squared to mass concentration were found to be  $24 \text{ kg m}^{-3}$  (1 MHz),  $12 \text{ kg m}^{-3}$  (2.25 MHz), and  $8 \text{ kg m}^{-3}$  (5 MHz). The limit for the linear response of attenuation to mass concentration was determined by hydrophone measurements to be  $24 \text{ kg m}^{-3}$  for the 2.25 MHz sonar (and its 4.5 MHz harmonic), and for the 5 MHz beam. Attenuation was not corrected for in the case of the 1 MHz sonar. Measured attenuation values were used to correct the  $V^2$  readings for the 2.25 and 5 MHz transducers. This linearized the 2.25 MHz values, but overcorrected the 5 MHz readings for concentrations greater than  $\sim 10 \text{ kg m}^{-3}$ . The explanation for this is postulated to be averaging of a non-linear process; i.e. that instantaneous attenuation must be applied to the instantaneous backscatter before averaging in order to correctly model the behavior.

Thorne et al (1991) used 3.0 and 5.65 MHz sonars in a combined empirical and analytical approach. The transducers were aimed longitudinally through a cylinder of well mixed sediment in the lab, and corrections were made for nearfield complications. Attenuation was calculated following Sheng and Hay (1988), but, rather than calculate  $|f_{\infty}(x)|$ , a calibration constant was determined from a single range and concentration. Overall accuracy of measurements using this technique was  $\pm 20\%$ . They point out that attenuation along a beam dominates the acoustic response to increasing concentrations at higher concentrations, so that the variation in  $\langle P_b \rangle$  with  $\sqrt{M}$  is no longer linear. In fact, the function becomes double valued, and linear empirical calibrations techniques are no longer valid. Their investigation also demonstrated that a 10 second average of 10 Hz signals clearly presents a more coherent profile than the signal from a single cycle. Their calibrations are performed using the 10 second average.

Later, Thorne et al (1993) use the more analytical approach, and include field testing. They illustrate the sensitivity of the attenuation integration technique by performing the integration through a constant sediment concentration of  $2.2 \text{ kg m}^{-3}$ . A 5-10% underestimate of the initial concentration led to an order of magnitude error at 105 cm. Backscatter results from field deployment compared with pumped samples from the same locations yielded agreement to  $\sim 10\%$ . Errors at higher concentrations were less than laboratory results, presumably because the concentration was not as consistently high throughout the beam as it was in the laboratory.

It has been recognized by the above workers that the use of more than one frequency may enable grain size estimation through the response of the form factor  $f_{\infty}$  and thus more accurate concentration inversion procedures. Hay and Sheng (1992) address this issue using again the 1, 2.25, and 5 MHz sonars. When the assumption is made that scattering attenuation is small, or corrected for, Equation (2.4) can be expressed as:

$$\overline{V}_i = S_i \sqrt{M/\rho_s} F(X_i, \sigma_g) \quad i=1,2,5 \quad (2.9)$$

where  $F(X_i, \sigma_g)$  is the representation of  $F[n(a), f_\infty(x)]$  under the assumption of a lognormal sediment distribution. The subscript  $i$  represents the different frequencies,  $X_i = k_c a_g$  (*acoustic wavenumber and geometric mean radius*) and  $\sigma_g$  = the standard deviation of the lognormal distribution. The ratios of signals from the different frequencies can then be written to eliminate the dependence on  $M$ :

$$\frac{F(X_i, \sigma_g)}{F(X_j, \sigma_g)} = \frac{S_j \overline{V_i}}{S_i \overline{V_j}} \quad i \neq j, i=1,2,5; j=1,2,5 \quad (2.10)$$

Since  $\overline{V}$  is measured and  $S$  is calculated independently, the left hand side can be computed using a semi-empirical expression for  $|f_\infty|$  which assumes a lognormal sediment (Hay and Sheng (1992) Equation (7)). To solve for both unknowns,  $a_g$  and  $\sigma_g$ , two independent ratios, and therefore three different frequencies, are required. Since the ratio for  $F_5/F_2$  is multi-valued at sand diameters less than 100  $\mu m$ , and the slope of  $F_2/F_1$  tends to 0 over 100  $\mu m$ , the procedure to calculate both variables is often indeterminate. Therefore, an independent measurement of  $\sigma_g$  was made on sand from the field experiment area, and used for the calculation. Once the value of  $a_g$  is determined, the concentration  $M$  can be estimated from:

$$M = \frac{\rho_s}{2} \left[ \frac{\overline{V_2^2}}{S_2^2 F^2(X_2, \sigma_g)} + \frac{\overline{V_i^2}}{S_i^2 F^2(X_i, \sigma_g)} \right] \quad \begin{array}{l} i=1 \text{ for } a_g \leq 100 \mu m \\ i=5 \text{ for } a_g > 100 \mu m \end{array} \quad (2.11)$$

Attenuation is addressed with a bin to bin integration technique that incorporates a modified high-pass model for  $\alpha_s$  introduced by Sheng and Hay (1988). Attenuation for the 1 MHz beam is assumed to be negligible.

In the laboratory, measurements of concentrations up to  $23 \text{ kg m}^{-3}$  of particles of from 90 to 430  $\mu\text{m}$  diameter were accurate within 10% using the three frequency algorithm. The algorithm underestimated grain size by 10% at concentrations above  $0.8 \text{ kg m}^{-3}$ , and 20% at lower concentrations. This error was presumed to be caused by weak 1 MHz signal at low concentrations, possible deposition of coarser materials in the jet mechanism, and/or systematic differences between the measured form factor for sand and the calculated value.

Acoustic measurements made in the field underestimated concentration by 20% when compared with measurements made by OBS instruments. This difference was less in low energy conditions. The near bottom acoustic estimates of grain size in the field were within 6-18% of the mean bottom sediment size, and showed a vertical decrease in sand size of 25% over 50 cm, which is consistent with other field studies.



### III. CALIBRATION

#### A. CASP DESCRIPTION

The Coherent Acoustic Sediment Probe (CASP) is a sediment flux sensor which was designed and built by Timothy P. Stanton of the Naval Postgraduate School, Monterey, CA, in 1992/1993. The instrument is both a coherent acoustic doppler velocity meter and a sediment profiler. The velocity measurements are made with three 5.2 MHz transducers mounted so that the beams intersect 25 cm in front of the instrument (Figure 3.1). Operation in both monostatic and bistatic modes allows measurement of all three components of velocity at 8 mm resolution (Stanton 1993). A 1.4 MHz transducer located in the center of the instrument and the three slanted beam 5.2 MHz transducers provide a sediment profiling capability in 1.68 cm bins to a range of 1 m. Sediment size discrimination can be inferred by comparison of the 5.2 and 1.4 MHz signals at the intersection point.

Several other instruments are located within the CASP transducer head to ensure correct interpretation of the data. A  $0.1^\circ$  accuracy two-axis tilt sensor enables vertical transformation of vector quantities into an earth referenced coordinate system, and a three axis accelerometer detects vibrations or other contaminating movement of the sensor. Finally, a high resolution pressure transducer provides instrument depth and wave height.

The data frames output from the CASP contain a complex pattern of both monostatic and bistatic sampling modes. In the bistatic mode, a burst of 32 short (0.8 cm length in seawater) pulses are transmitted by a single 5.2 MHz transducer, while the other two 5.2 MHz transducers "listen" to the backscattered energy from the beam intersection. This continues in round robin sequence for each of the three 5.2 MHz transducers (See Stanton 1993, section 3 for complete coverage of velocity measurements). A monostatic sample for each of the four beams is interleaved within this sequence. A triplet of longer (1.7 cm) bursts is transmitted by each of the four transducers in sequence, and the complex backscatter

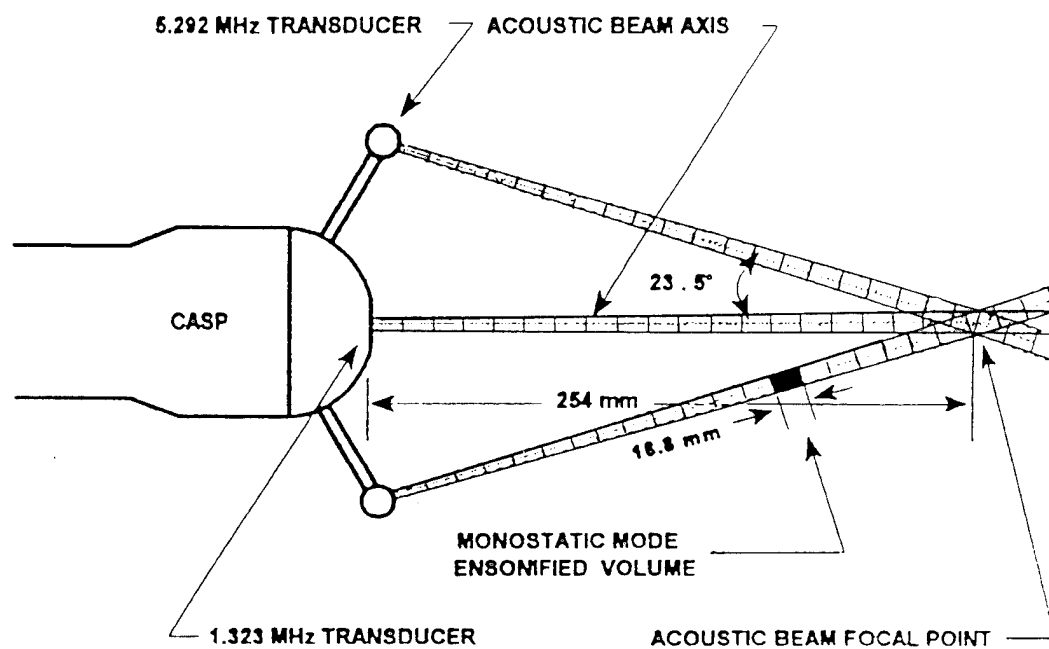


Figure 3.1 Schematic of the CASP acoustic beam geometry. (Stanton, 1993)



amplitudes are sampled every 1.68 cm out to a range of 1.2 m. The full sequence of 3 bistatic and 3 monostatic transmissions is repeated at a rate of 36 Hz. In the monostatic data record, every fourth 1.68 cm "bin" is used to store other information, so that the actual sampling profile appears as in Figure 3.2.

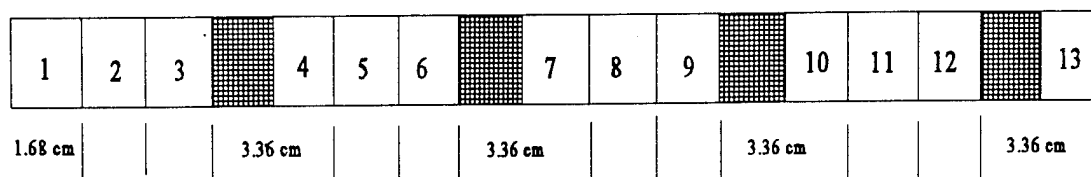


Figure 3.2 CASP Bin Map

The backscattered signals pass through a high gain, wide dynamic range amplifier and mixer which shift the ultrasonic signals to base band frequencies. The complex amplitude signals are then sampled at pre-programmed delays to form the raw, digitized, coherently sampled acoustic data stream. The resulting processed power data is stored as 1000 times the base ten logarithm of the counts (voltage) squared. In the following sections,  $C$  (counts) is used as the analogue for sound pressure amplitude, in contrast to  $V$  (volts) as used in the previous "background" section.

## B. CALIBRATION THEORY

As discussed in the background, inversion of backscatter signals to sediment concentration measurements can be approached either empirically or through more analytical acoustic modeling. Because the sand at Duck, N.C. is historically homogeneous at the bar, and samples are easily taken, and an empirical technique is used for this calibration. For low concentrations (approximately  $10 \text{ kg m}^{-3}$ ), the dual frequency profiler will allow some discrimination of changes in mean grain size.

In the laboratory, measurements of known concentrations of sample sand (from 0.13 to 98.9 kg m<sup>-3</sup>) are made in the farfield of the acoustic transducer. The sand is contained in a cylindrical test vessel and the concentration is kept homogenous by vigorous mixing (see laboratory description). Calibration and attenuation coefficients are determined for each frequency from the backscatter levels at each range.

The governing equation for acoustic behavior through a water/sand medium can be expressed as:

$$\bar{C} = S \sqrt{\frac{M}{\rho_s}} F[n(a), f_{\infty}(x)] \frac{r}{r_0} \exp[-2 \int_0^r \alpha_t dr] \quad (3.1)$$

This equation differs from Equation 2.4 in the inclusion of the range spreading term and the exclusion of the sinh term. The within-bin attenuation represented by the sinh term is instead compensated for during the integration algorithm by integrating through one half of the bin undergoing calculation. The acoustic response function  $F[ ]$  has a frequency dependent behavior due to the size distribution and backscatter form function,  $f_{\infty}(x)$ , which was determined empirically by Hay (1991). For a lognormal sediment size distribution, the final response function can be expressed (Hay and Sheng, 1992) in terms of the geometric mean radius of the particles,  $a_g$ , the acoustic wave number  $k_c$ , and the grain size distribution  $\sigma_g$ :

$$F(X, \sigma_g) = k_c^{-1/2} \sqrt{\frac{\int_0^{\infty} a^2 |f_{\infty}(x)|^2 \exp\left[-\frac{(\ln a - \ln a_g)^2}{2 \ln^2 \sigma_g}\right] d \ln a}{\int_0^{\infty} a^3 \exp\left[-\frac{(\ln a - \ln a_g)^2}{2 \ln^2 \sigma_g}\right] d \ln a}} \quad (3.2)$$

where  $a$ =equivalent radius of the particle and  $X=k_c a_g$  and  $|f_{\infty}(x)|$  is as described in Equation 2.7.

The response functions for both CASP operating frequencies are illustrated for varying mean sediment sizes and lognormal distribution widths ( $\sigma$ ) in Figure 3.3. The sand sampled from the bar and trough area of Duck, NC, and used for the calibration has a mean geometric radius of .09 mm and a standard deviation of 1.2. Note that for sand of these characteristics, the 5.3 MHz response is largely constant with radius, but can vary as much as 10% with the distribution width. The 1.3 MHz beam response is more susceptible to variations in mean particle size, and can vary up to 20% with standard deviation. The calibration is made assuming a constant grain size distribution with fixed mean and width so that this form factor is empirically represented by the single frequency calibration coefficient,  $C_m$ . Similarly, since the instrument characteristics are the same in the laboratory and the field, the instrument sensitivity,  $S$ , which depends on frequency, directivity and beam characteristics, and on the form function of the object illuminated, will also be represented in the calibration coefficient.

Once these simplifications are applied, the resulting calibration equation is:

$$M = C^2 * \frac{C_m}{A_{(r, \alpha_w, \alpha_s)}^2} \quad \text{where} \quad A = \frac{r_0}{r} * e^{-2 \int_0^r (\alpha_w + \alpha_s) dr} \quad (3.3 \text{ a, b})$$

$M$  is the mass concentration ( $\text{kgm}^{-3}$ ),  $C$  is measured counts,  $C_m$  is the calibration coefficient, and  $A$  is the integrated compensation factor integrated from the transducer face to the measurement bin at range  $r$ .

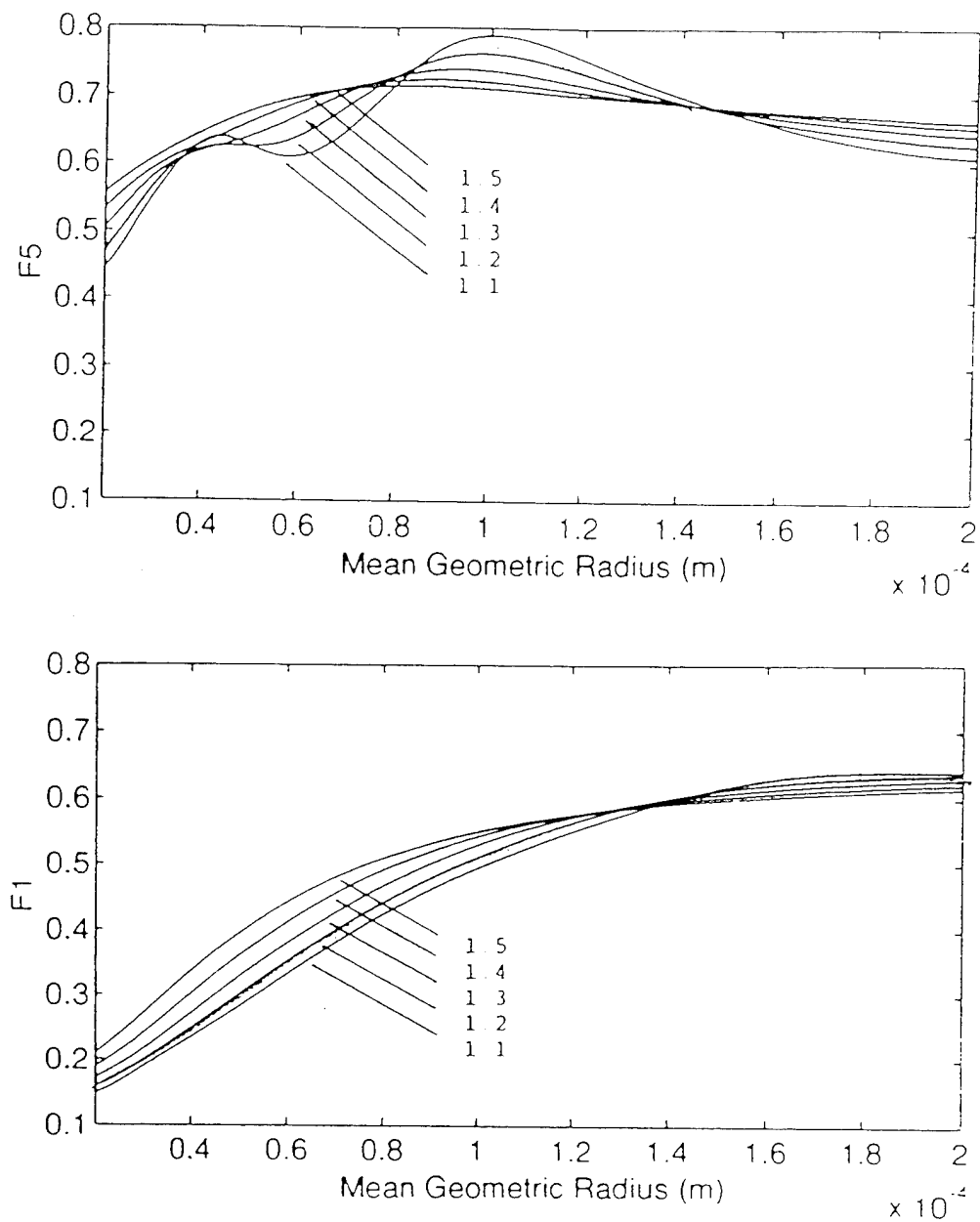


Figure 3.3 Response functions for 1.3 MHz and 5.3 MHz, assuming a lognormal particle size distribution, as a function of the particle mean geometric radius for values of  $\sigma = 1.1, 1.2, 1.3, 1.4, 1.5$ .

## C. LABORATORY DESCRIPTION

### 1. Tank

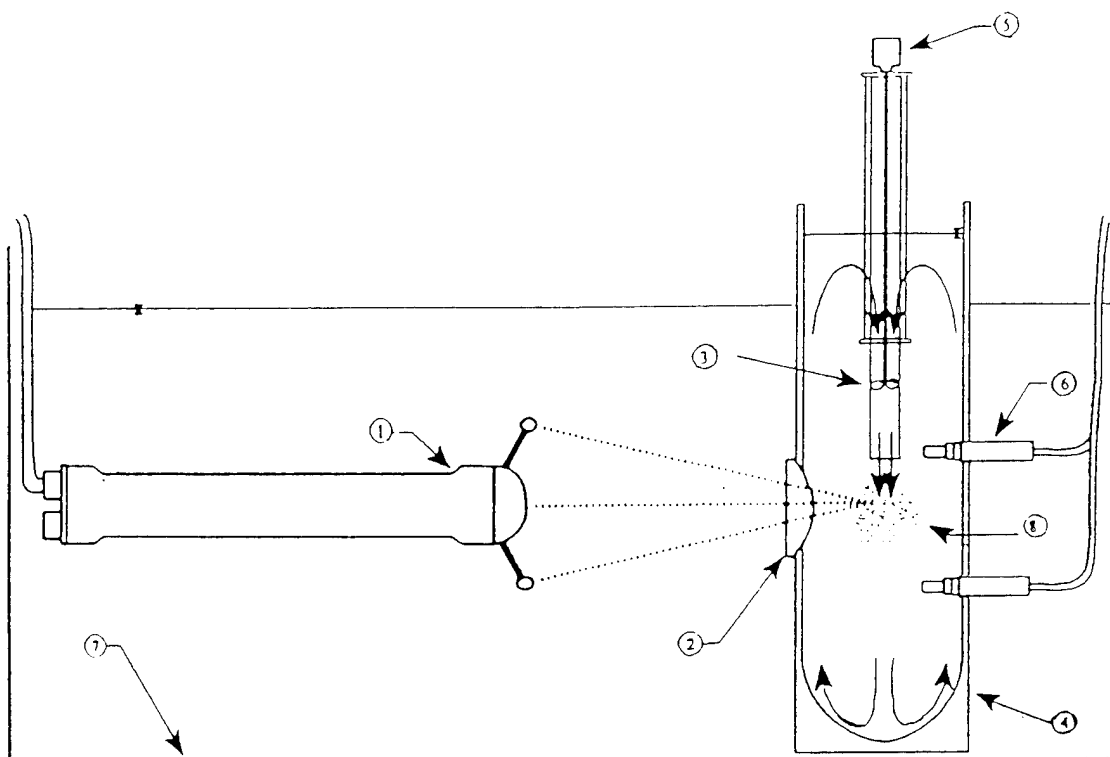
The CASP was immersed in a 600 gallon acrylic tank filled with fresh, filtered water for the calibration procedures. A 16 liter cylindrical acrylic test vessel, positioned inside the large tank, was used to contain controlled masses of sample sediment (Figure 3.4). The test vessel was equipped with an acoustically transparent plastic film window, a controllable speed propeller stirrer, and two downward facing OBS's inserted in an O ring sealed sidewall opening. The vessel was designed so that the measured masses of sand were homogeneously mixed throughout the volume with no level surfaces or stagnation points. The CASP was aimed at the transparent window so that the beam intersection point was approximately 2 cm inside the test vessel.

### 2. Sediment

Sand was obtained from the trough and bar (top) region of the nearshore zone at the CERC-FRF in Duck, N.C. in both August, 1994, and June, 1995. During the DUCK94 experiment, sand was sampled 20 October 10 meters south of where the CASP operated (Stauble, 1995). Results of the grain size lognormal distributions are summarized in Table 3.1.

Bar/Trough	B-Oct 94	B-Aug 94	B-Jun 95	T-Oct 94	T- Jun 95
Mean	.142 mm	.184 mm	.191 mm	.144 mm	.192 mm
Sigma	1.25	1.23	1.2	1.36	1.2

Table 3.1 Lognormal Mean Diameter and Standard Deviation of Sand from Duck, NC



1. COHERENT ACOUSTIC SEDIMENT PROBE (CASP)
2. ACOUSTICALLY TRANSPARENT MEMBRANE
3. ACRYLIC NOZZLE AND DUCTED PROPELLER
4. ACRYLIC TEST VESSEL
5. VARIABLE SPEED MOTOR
6. OPTICAL BACKSCATTER SENSOR
7. ACRYLIC LABORATORY ACOUSTIC TEST TANK
8. SUSPENDED SEDIMENT

Figure 3.4 Schematic of the test tank, CASP, and the mixing vessel with propeller stirrer (Stanton, 1993).

The lognormal fit of the sand used for the calibrations is shown in Figure 3.5. The calibration sand was sifted to eliminate particles larger than .85 mm to prevent interference with the propeller mechanism. After drying, the sand was weighed in roughly sub octave increments so that the concentration in the test vessel would increase slowly to  $25 \text{ kg m}^{-3}$ , then more rapidly to  $100 \text{ kg m}^{-3}$ .

### **3. Procedure**

Once the CASP and test vessel were positioned, a dry run was made to ensure proper alignment and check for acoustic reverberation interference. The calibration began with two cases of no sediment, one still and one stirred, and continued with incremental additions of sand. Each increment was measured for three minutes, and one to two minutes were taken between increments for addition of sand and stirring. Several calibration runs were conducted with both August 1994 and June 1995 sand samples.

### **4. Calibration Method Sensitivities**

The consistency of the calibration data was affected significantly by two experimental variables: (1) the entrainment of micro-bubbles on the sand particles as they were added to the test vessel; and (2) the position of the test vessel window within the CASP data bin map. These considerations will be discussed here. The performance of the stirrer and the resulting homogeneity of the mixture, and the consistency between runs using the two sand samples is also addressed.

Rapid addition of sand to the test vessel resulted in an unacceptable degree of scatter due to microbubble entrainment, even after a one to two minute settling/stirring period between recordings. Even after rinsing the sand with a chemical wetting agent, the most consistent runs were made when the sand was carefully and slowly tapped into the cylinder.

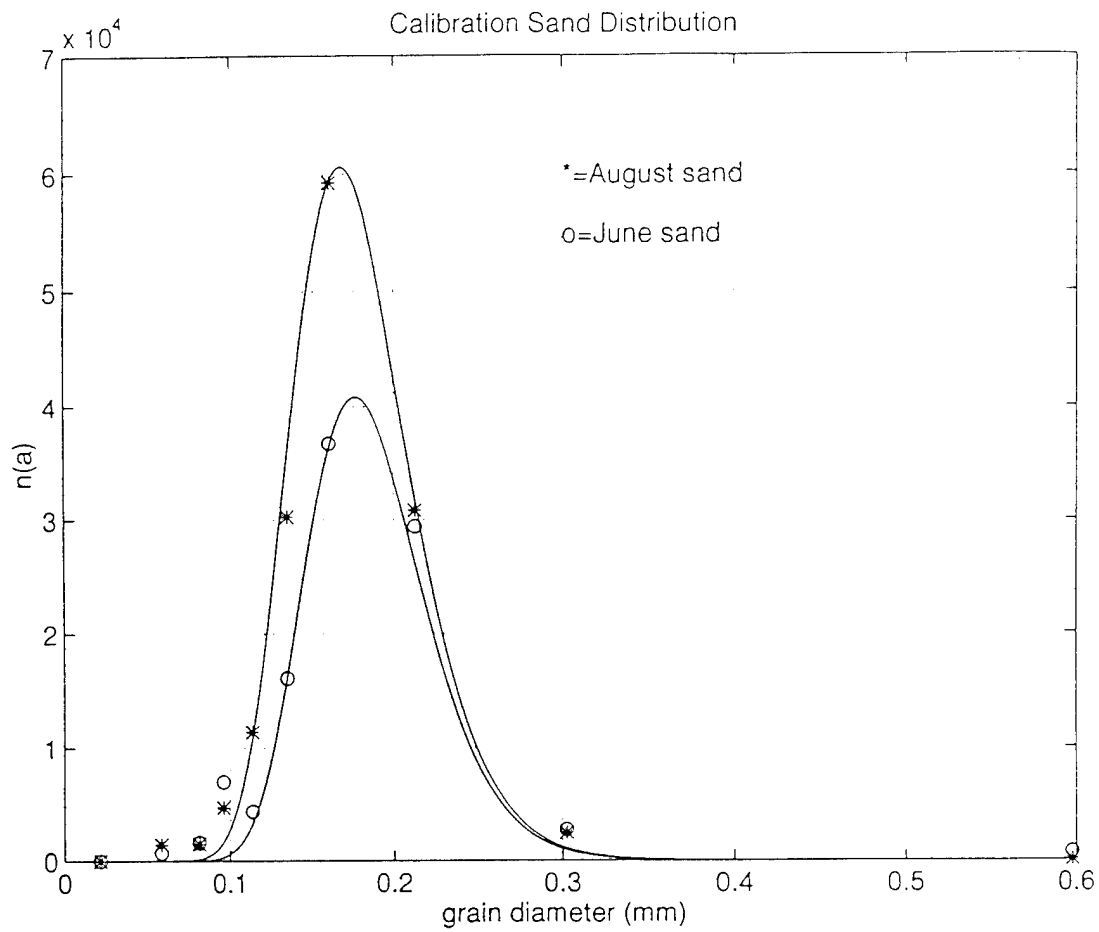


Figure 3.5 Lognormal distribution of sand used for calibration.



An extreme example of the effect of this on the attenuation coefficient is shown in Figure 3.6. This effect can also be observed when the three minute recording time is divided into one min segments. As seen in Figure 3.7, the attenuation coefficient (especially at higher concentrations) decreases with time, suggesting the gradual dissipation of bubbles during the stirring process.

To examine the effect of the window position within the bin map, the CASP was run through a computer controlled grid pattern in front of the test vessel while a concentration of  $10 \text{ kg m}^{-3}$  was maintained in the vessel. Figure 3.8 is a three dimensional representation of the backscatter power ( $\text{counts}^2$ ) response as the CASP backs away from the center of the window. The window is located between 0.25 and 0.50 meters as the CASP retreats. The rear peak is the back of the test vessel, and the peaks in front of the window represent reverberation responses. Although these reverberations do not affect the voltage level received in the test vessel segment of the beam, they must be corrected for when the data is used for the along-beam calibration integration. When the window is within one of the large bins of the map, the voltage reading can be divided between two bins to an unknown degree (Figure 3.9). Although this percentage can be estimated, the situation causes an uncertainty factor in the calculation of the  $C_m$  coefficient. This will be discussed further in the  $C_m$  calculation section.

The performance of the stirrer and the resulting homogeneity of the mixture were also investigated as possible sources of error. The absolute concentration is verified by readings from two OBS's, mounted one above the other at the level of the window and just below the surface of the water. OBS measurements of sediment concentration for each calibration run agree well with controlled sediment concentrations (Figure 3.10). The one minute averaged OBS measurements were consistent within  $1 \text{ kg m}^{-3}$  below  $50 \text{ kg m}^{-3}$ , and varied less than  $5 \text{ kg m}^{-3}$  from  $50$  to  $100 \text{ kg m}^{-3}$ , indicating that the mixture was indeed homogeneous. If the stirrer was offset within the test vessel, an inconsistent gradient through the beam would result. This condition could be detected in the data by varying the number of bins through

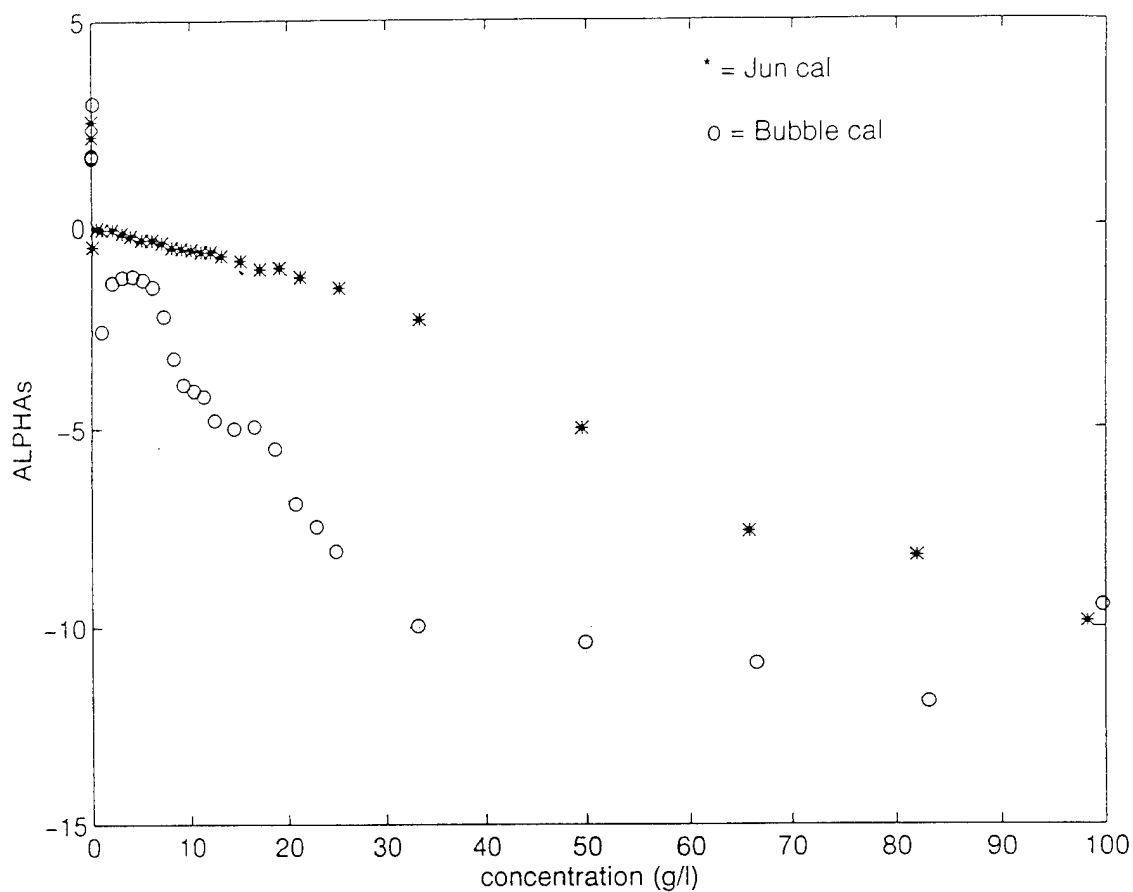


Figure 3.6 Affect of microbubble entrainment on  $\alpha_s$ . The June calibration shows the expected linear increase of  $\alpha_s$  with concentration to  $25 \text{ kg m}^{-3}$ ; for the "bubble" calibration,  $\alpha_s$  values increase unpredictably, and are higher than the values expected for the 1.3 MHz beam.

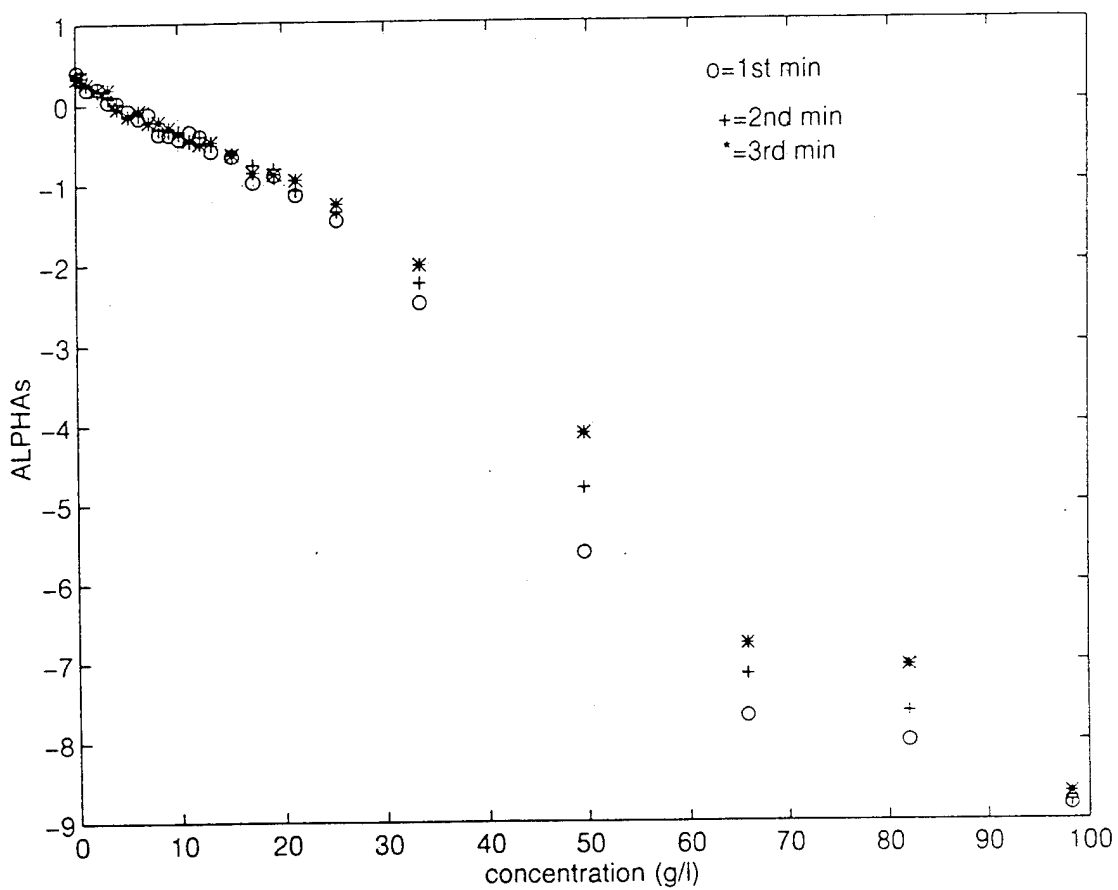


Figure 3.7 Evidence of microbubble dissipation with time for June calibration, Beam 1.

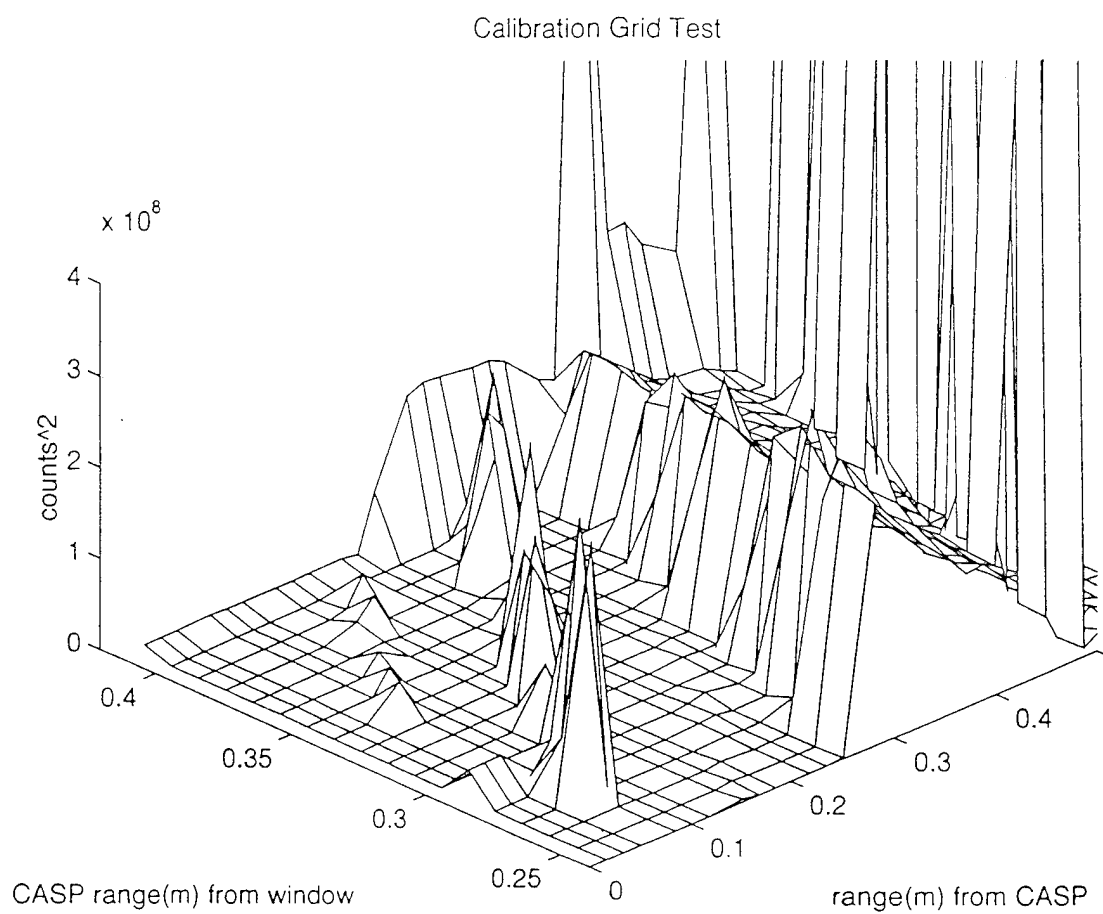


Figure 3.8 Three dimensional representation of backscattered power during computer controlled grid pattern.

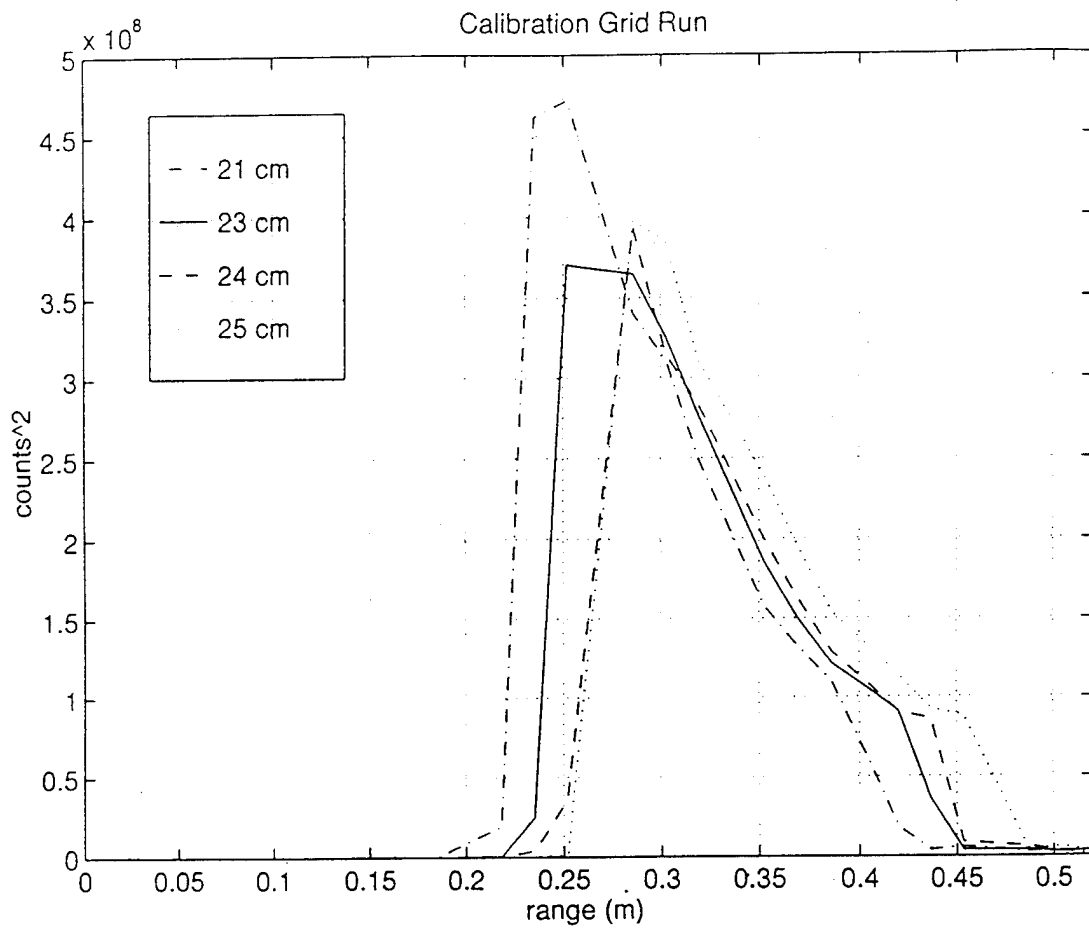


Figure 3.9 Backscatter profile for 1.3 MHz during calibration grid test. A single peak indicates that the first bin is completely full of sediment; a sloped peak occurs when the window intersects the first bin. The linestyles represent different CASP-to-window ranges.

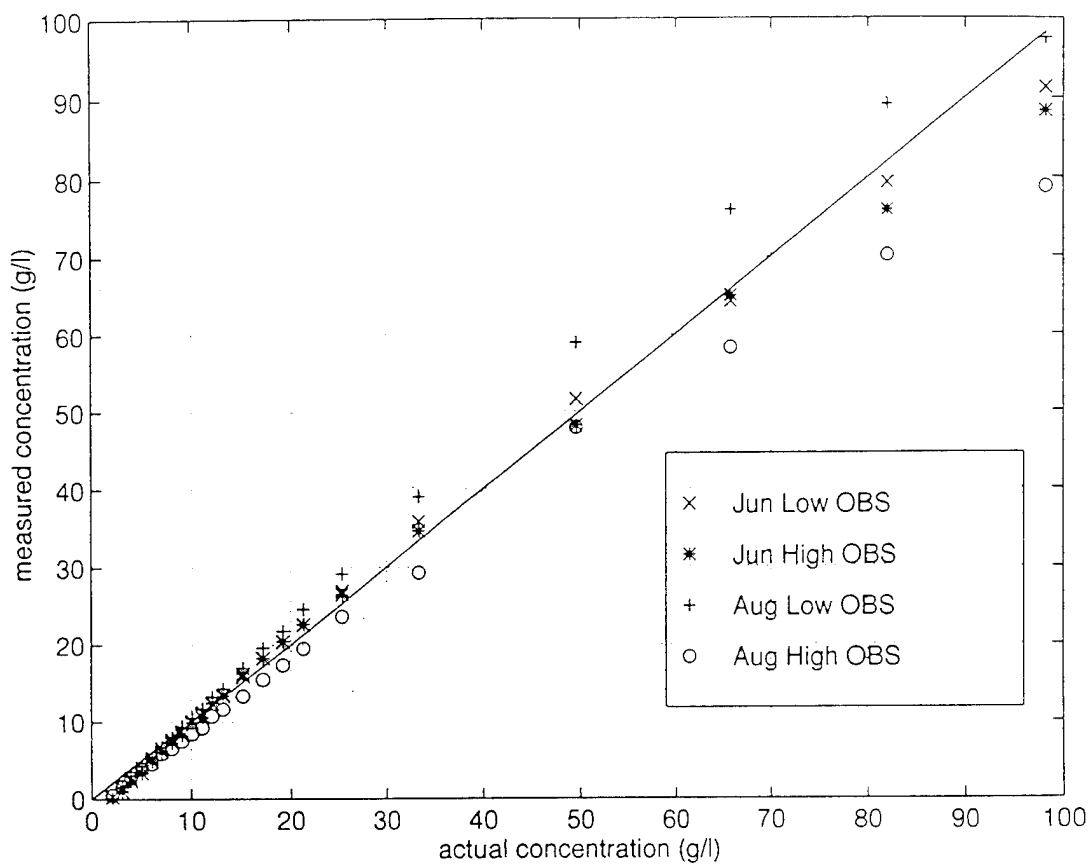


Figure 3.10 OBS readings for June and August calibration runs.

which the attenuation coefficient was calculated and noting inconsistencies, but careful placement of the stirrer avoided this situation. The experimental design and resulting homogeneity of the sand volume was therefore considered sufficient for the calibration technique.

Any variation between calibration runs using each of the two sand samples could be accounted for by the above considerations; minor differences in the distribution of the grain sizes were not resolved in the calibration. Two calibration runs, one using August sample bar sand and the other June sample trough sand (hereon referred to as Aug and Jun cal runs), are presented to illustrate the procedure and analyze its effectiveness.

#### D. COEFFICIENT DETERMINATION

The piece-wise bin integration form of Equation 3.3b is:

$$A = \frac{r_0}{r} \exp\left(-2 \int_0^r \alpha_w + aslope * mass(bin-1) * dr\right) \quad (3.4)$$

where  $dr = 1/2 * length(bin-1) + 1/2 * length(bin)$  and the *aslope* coefficient is applied to the mass calculated for the previous bin to determine the appropriate  $\alpha_w$  value for the compensation. Two implementations of the integration routine are used. First, an attenuation-only correction can be applied to the counts<sup>2</sup> values. In this case, known concentration is used for the “*mass(bin-1)*” of the compensation *A* of Equation (3.4). No  $C_m$  coefficient is applied, so that *M* equates to corrected counts<sup>2</sup> vice corrected mass. The second implementation uses the mass calculated from the previous bin as would be used in actual measurements without known sediment concentrations.

An additional procedure within the integration was developed to correct for the situation where a given bin spanned the test vessel acoustic window. This window bin

correction was implemented with a conditional loop in the integration routine which identified the affected bin (due to the ½ bin to ½ bin procedure, the bin beyond the window is affected for window percentages <.5) and appropriately adjusted the  $dr$  and  $mass$ . For the corrected mass integration technique, known mass is used for the window bin compensation.

The data were also corrected for system noise. The backscatter field in counts for the June calibration of the 1.3 MHz beam is depicted in Figure 3.11. The square root of the actual power was used to best identify areas of reverberation interference. A noise floor was calculated by averaging the values in the bins not affected by reverberation peaks, and the square of this value was subtracted from the raw backscattered power record. The noise floor averaged 4000 counts<sup>2</sup>. Readings between the CASP and the test vessel face were zeroed.

## 1. *Aslope Coefficient*

### *a. Calculation*

Figure 3.12a portrays the reading in counts (volts) along the CASP 1.3 MHz beam while the vessel concentration was held at 6 kg·m<sup>-3</sup>. The six measurements in the center of the test volume were used to calculate the attenuation coefficient,  $\alpha_s$ . The measured change in backscattered power vs. range in a constant concentration follows a logarithmic decay due to attenuation of pure water and scattering by the sand particles, superimposed on a 1/r radial beam spreading:

$$C = C_0 \frac{r_0}{r} e^{-2\alpha_t \Delta r} \quad \text{where} \quad \alpha_t = \alpha_w + \alpha_s \quad (3.5 \text{ a, b})$$

Here  $C$  (counts)  $\propto$  acoustic pressure, and total attenuation  $\alpha_t$ , is the contribution due to fresh water absorption and particle scattering, respectively.



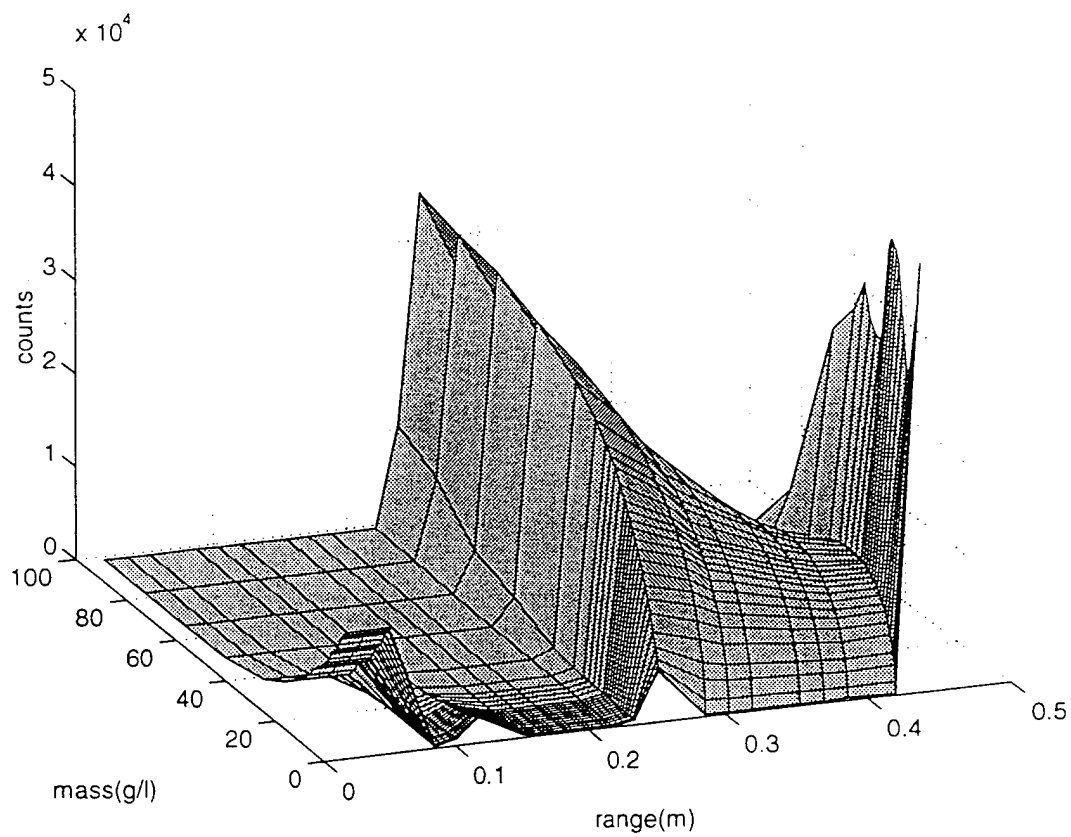


Figure 3.11 June calibration backscatter field in counts for Beam 1.

Therefore,

$$\alpha_s = \frac{\ln\left(\frac{C}{C_0} \frac{r}{r_0}\right)}{-2\Delta r} - \alpha_w \quad (3.6)$$

and  $\alpha_s$  is calculated for each concentration as the rate of the decay of the range-corrected natural logarithm of counts over range (Figure 3.12b). The value of each  $\alpha_s$  is then plotted versus concentration, and the calibration attenuation coefficient *aslope*/(m\*kg·m<sup>-3</sup>) is determined by linear regression. To integrate a sediment measurement profile using Equation (3.4), the *aslope* coefficient is applied to the concentration of the previous bin to determine the  $\alpha_s$  value, and the  $\alpha_w$  and *1/r* spreading corrections are reapplied to calculate the compensation factor for that bin.

The  $\alpha_w$  value does not vary significantly between seawater and freshwater for either frequency, but does change with frequency and temperature. Values were calculated from Fisher and Simmons (1988) and are shown in Table 3.2:

Temp/Freq	1.3 MHz	5.3 MHz
15 C	0.0503	0.8369
20C	0.0414	0.6884
23C	0.0371	0.6166

Table 3-2.  $\alpha_w$  Values for Frequency and Temperature Variations

#### b. 1.3 MHz Beam Attenuation

Attenuation coefficients for the 1.3 MHz beam for the full range of concentrations for the June and August calibrations are shown in Figure 3.13. A common characteristic

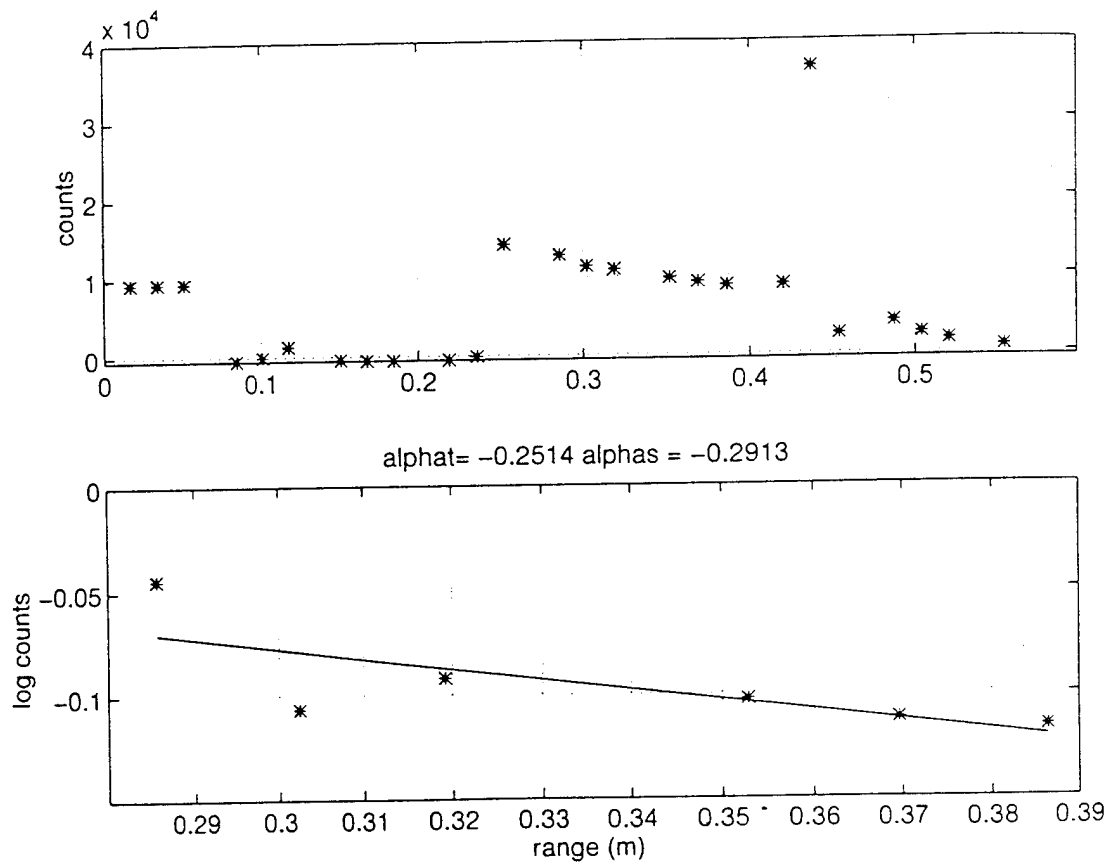


Figure 3.12 a) Profile of recorded counts along Beam 1 at  $6 \text{ kg m}^{-3}$ . The test vessel is between ranges .23 and .40 m. b)  $\alpha_s$  calculation as fit of log of counts.

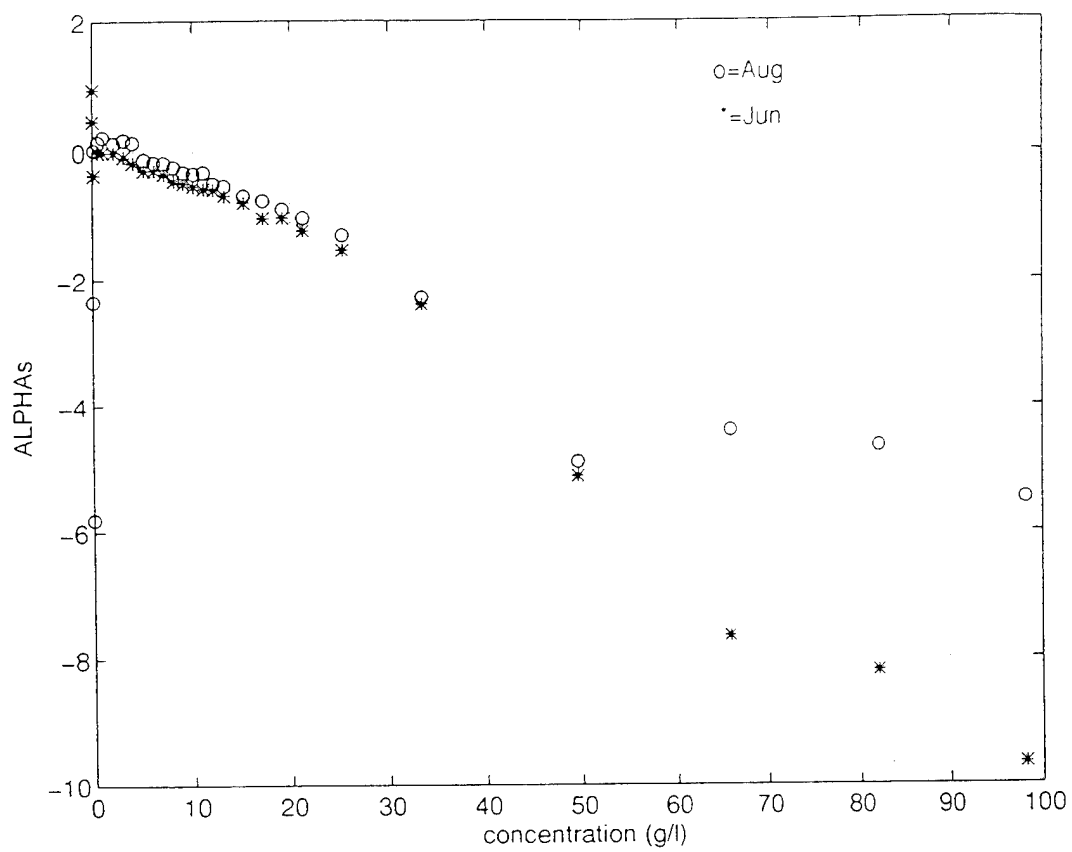


Figure 3.13 Beam 1 sediment attenuation for June and August calibrations.

of all calibration runs was the nonlinearity of values above  $33 \text{ kg m}^{-3}$ . Further analysis of corrected sediment profiles confirmed a breakdown of predictable behavior at this point, indicating the onset of multiple scattering. The first three anomalous points are due to residual background particles at the 0 and  $0.13 \text{ kg m}^{-3}$  concentrations. The calibration calculations therefore used concentrations from .5 to  $25 \text{ kg m}^{-3}$  (Figure 3.14). The *aslope* values differed slightly ( $<0.005 /(\text{m kg m}^{-3})$ ) when four to six bins beyond the window were used for the calculation; therefore the mean of these values is used for the calibration (Table 3.3). Other calibration runs with minimal micro-bubble contamination yielded values within  $.005 /(\text{m kg m}^{-3})$  of this value.

The attenuation-only integration technique was applied to the counts<sup>2</sup> calibration data to evaluate the performance of the calculated *aslope* coefficient. Figures (3.15a-g) illustrate this correction for each concentration. At bin 18 (13 cm within the volume), the attenuation correction equates to a 60 to 80% correction in mass from the lightest to heaviest ( $25 \text{ kg m}^{-3}$ ) concentrations. The integration performs well through the entire 13-15 cm range; standard deviation along the line averaged less than 0.1 (counts<sup>2</sup>/1e8) up to  $15 \text{ kg m}^{-3}$ , and less than 0.3 (counts<sup>2</sup>/1e8) up to  $25 \text{ kg m}^{-3}$ . The instability of the correction at  $33 \text{ kg m}^{-3}$  attests to the onset of multiple scattering effects.

CAL / BEAM	1	2	3	4
JUNE	-0.0588	-1.113	-1.147	-1.117
AUGUST	-0.0574	-1.123	-1.197	-1.161
CALIBRATION	-0.058	-1.14	-1.14	-1.14

Table 3.3. *Aslope* Coefficients

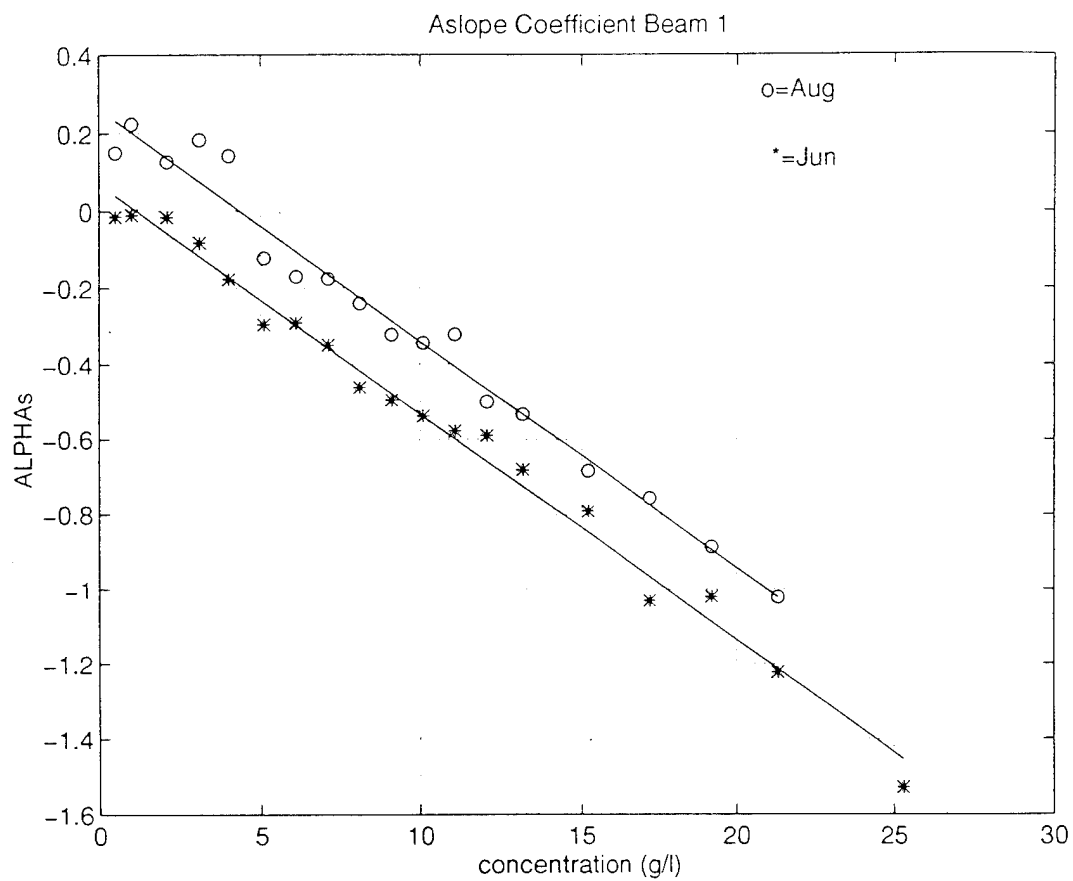


Figure 3.14 *Aslope* coefficient calculations for 1.3 MHz June and August calibrations. See Table 3.3 for *aslope* values.

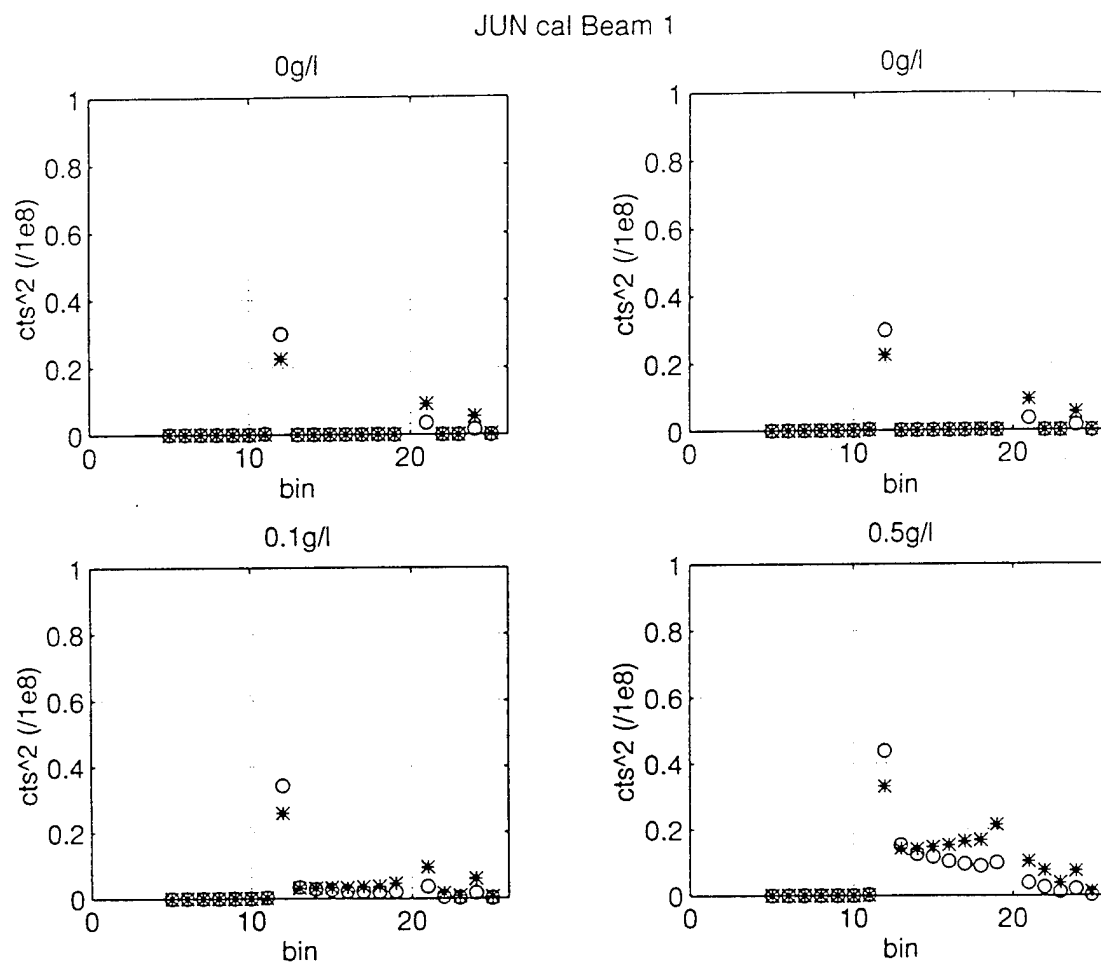


Figure 3.15a 1.3 MHz backscatter voltage corrected for attenuation; o=uncorrected counts<sup>2</sup>, \*=corrected counts<sup>2</sup>. The two 0 g/l examples are for an empty test vessel first unstirred and then stirred.

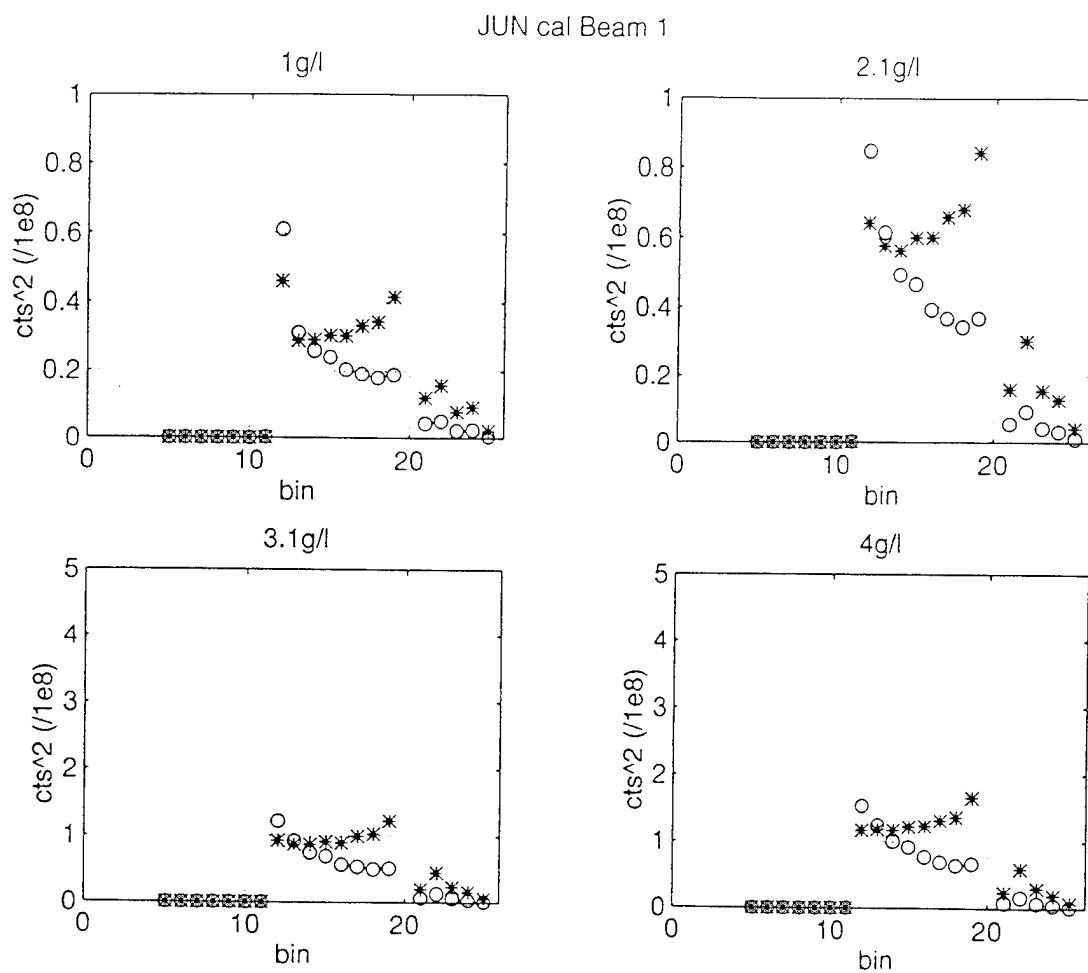


Figure 3.15b 1.3 MHz backscatter voltage corrected for attenuation; o=uncorrected counts<sup>2</sup>, \*=corrected counts<sup>2</sup>.



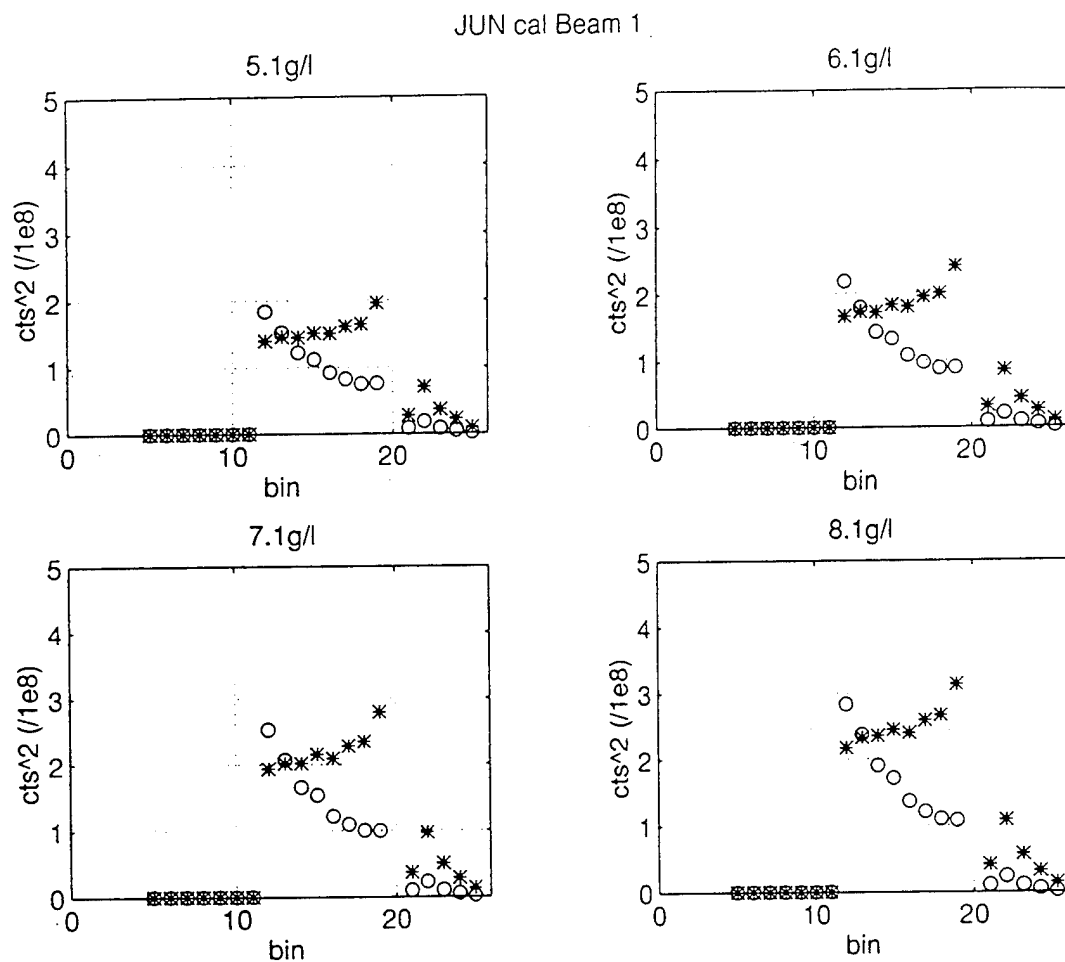


Figure 3.15c 1.3 MHz backscatter voltage corrected for attenuation; o=uncorrected counts<sup>2</sup>, \*=corrected counts<sup>2</sup>.

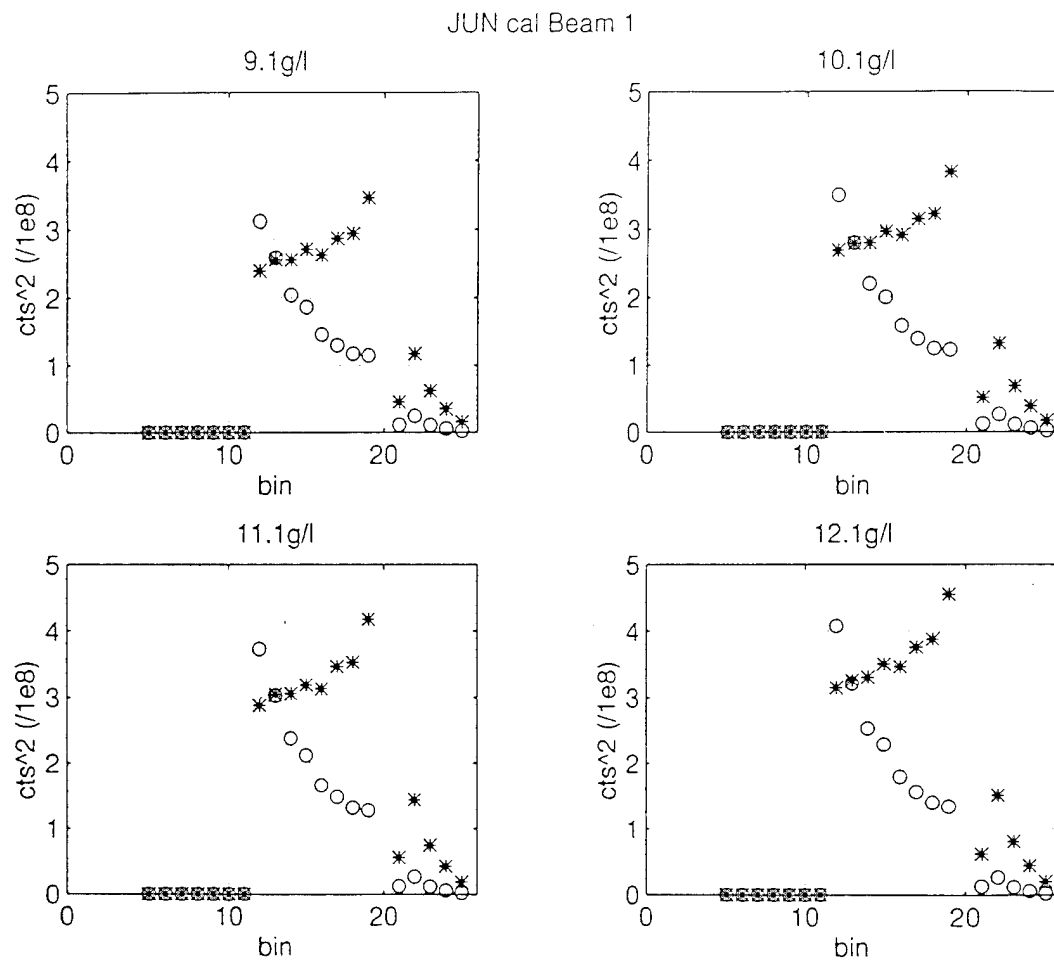


Figure 3.15d 1.3 MHz backscatter voltage corrected for attenuation; o=uncorrected counts<sup>2</sup>, \*=corrected counts<sup>2</sup>.

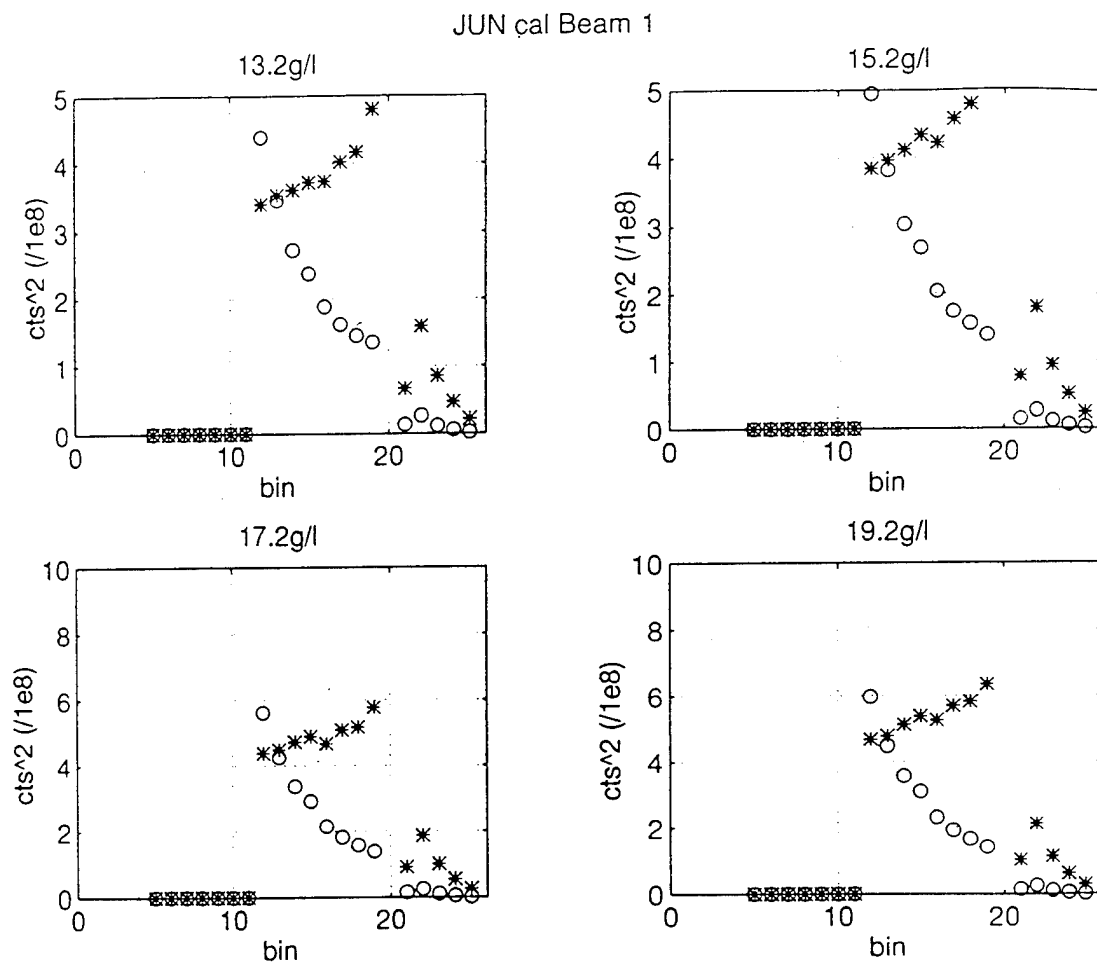


Figure 3.15e 1.3 MHz backscatter voltage corrected for attenuation; o=uncorrected counts^2, \*=corrected counts^2.

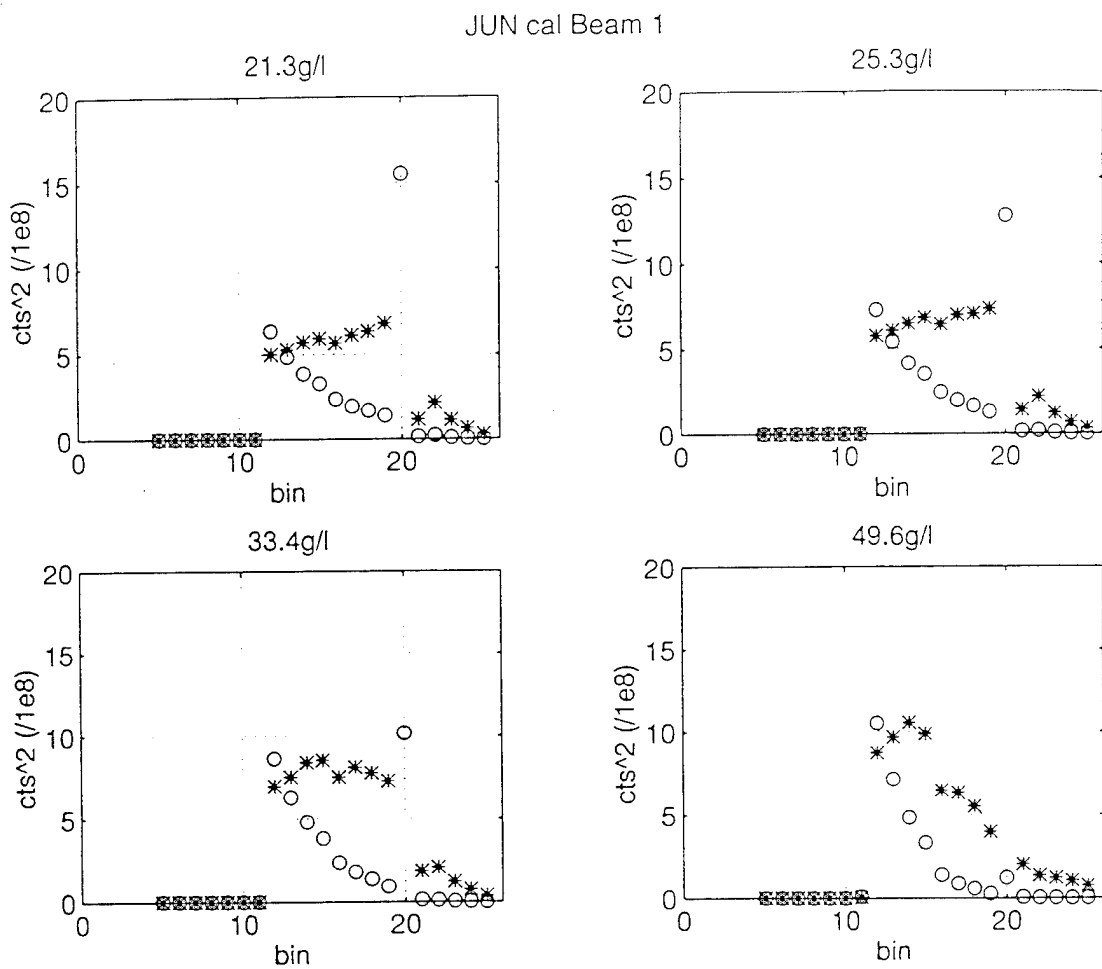


Figure 3.15f 1.3 MHz backscatter voltage corrected for attenuation; o=uncorrected counts<sup>2</sup>, \*=corrected counts<sup>2</sup>.

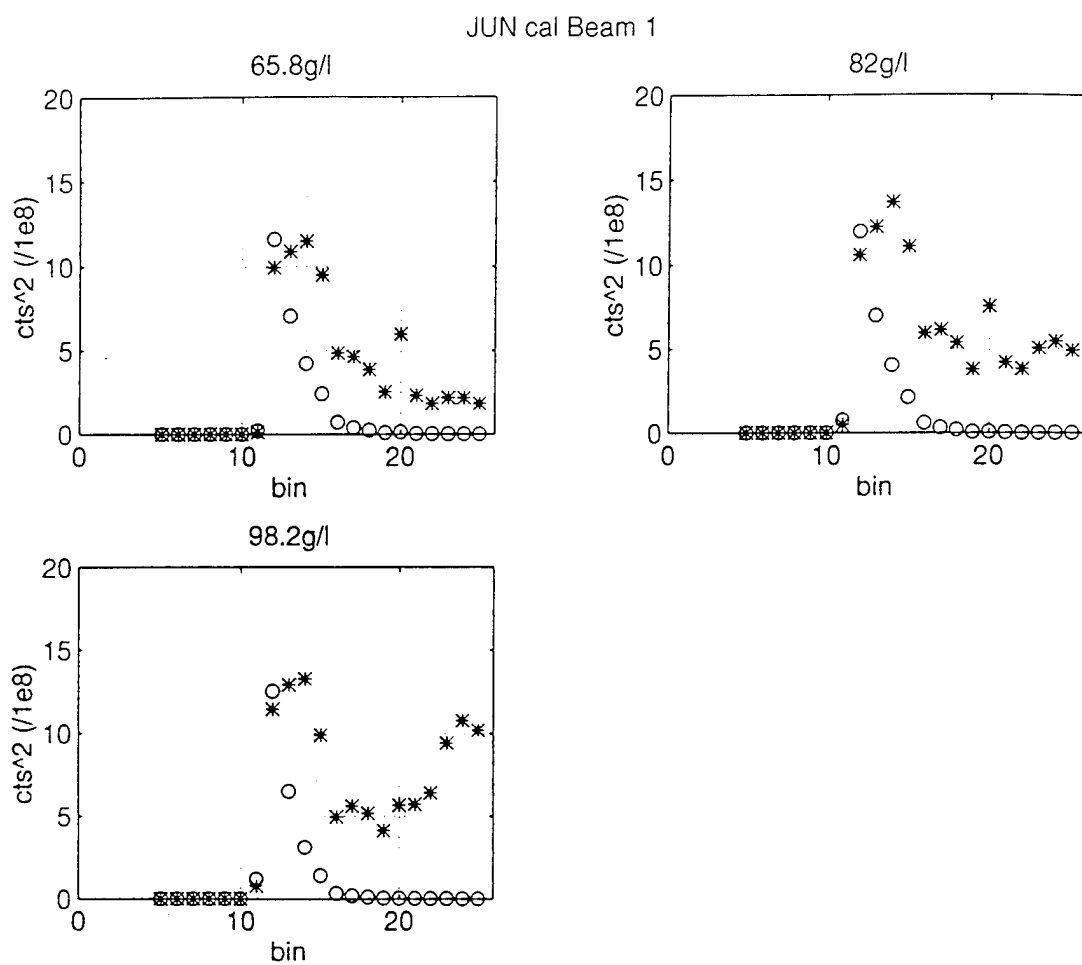


Figure 3.15g 1.3 MHz backscatter voltage corrected for attenuation; o=uncorrected counts<sup>2</sup>, \*=corrected counts<sup>2</sup>.

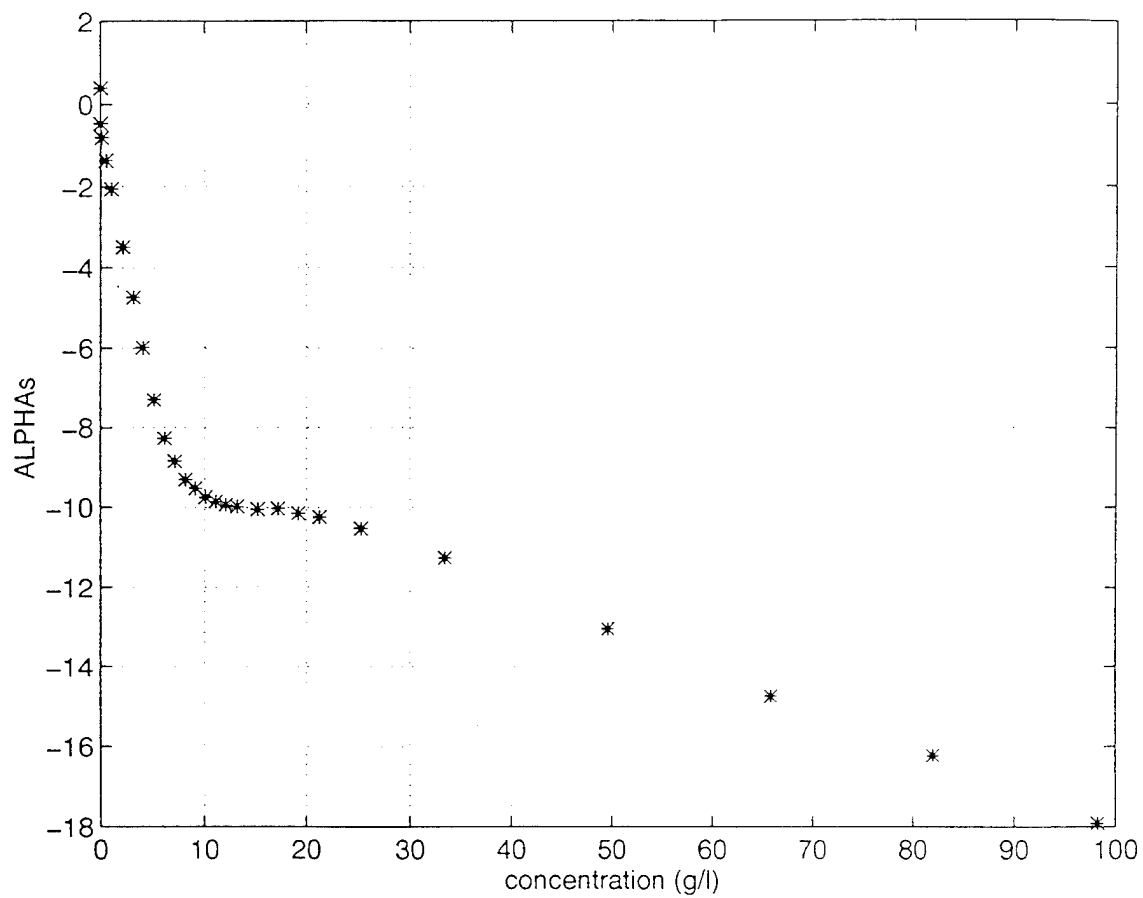


Figure 3.16 Beam 2  $\alpha_s$  values for 5.3 MHz June calibration.

### c. 5.3 MHz Beam Attenuation

The effectiveness of the 5.3 MHz beams suffers from multiple scattering at a much lower particle concentration (Figure 3.16); the *aslope* calculations were therefore limited to  $8 \text{ kg}\cdot\text{m}^{-3}$ . The *aslope* values in Table 3.3 are again the mean of the values calculated using four to six bins beyond the window (these values varied an average of  $.03/(\text{m}\cdot\text{kg}\cdot\text{m}^{-3})$  from one another). The attenuation integration was conducted with the partial window modification; Figures 3.17a-d show the results of this correction through the beam. The 5.3 MHz attenuation correction is consistent only 3 bins (5-7 cm) into the medium once concentrations exceed  $4 \text{ kg}\cdot\text{m}^{-3}$ .

## 2. $C_m$ Coefficient

### a. Calculation

The calibration coefficient (Equation 3.3a), quantifies the linear proportionality of mass to the square of pressure amplitude counts measured by the instrument (corrected by spreading and attenuation.). Several methods exist to calculate this proportionality and include direct fit, attenuation-corrected fit, and optimization fit techniques.

First, and most simply, is the direct linear fit of the  $\text{counts}^2$  reading in the first bin of the test vessel to the known concentration. As this fit is made to increasing maximum concentrations (4 to  $25 \text{ kg}\cdot\text{m}^{-3}$ ), its value changes slightly, a behavior attributed to the approach of the multiple scattering regime. Ideally, the window of the test vessel is located at the very beginning of a data bin, so that the first bin for calculation is represented by a full bin of sediment. In this case, the values for this first bin need only be corrected for the water attenuation to the window, and then fit to the known concentration. The experimental technique emphasized correct positioning of the 1.3 MHz beam window bin, which

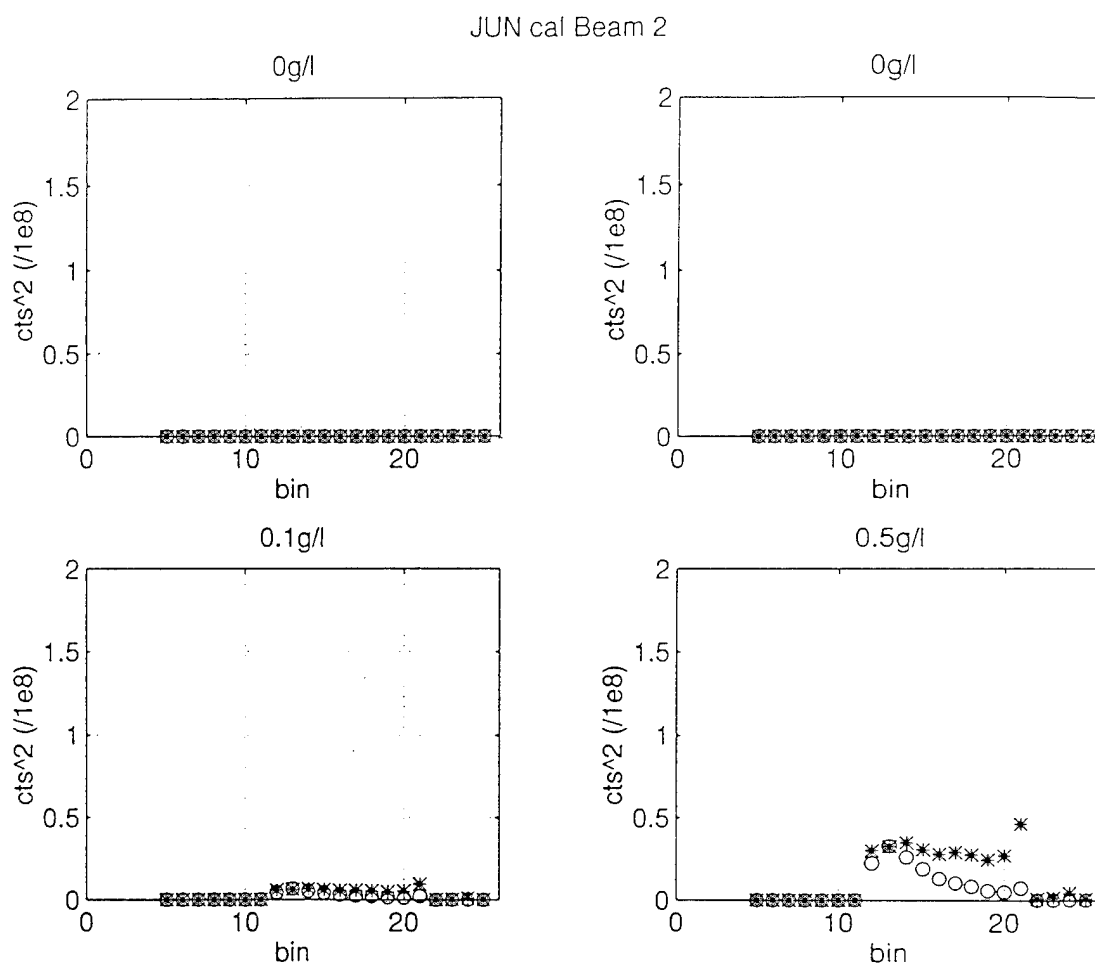


Figure 3.17a 5.3 MHz backscatter voltage for Beam 2 corrected for attenuation; o=uncorrected counts<sup>2</sup>, \*=corrected counts<sup>2</sup>. The two 0 g/l examples are for an empty test vessel unstirred and stirred.



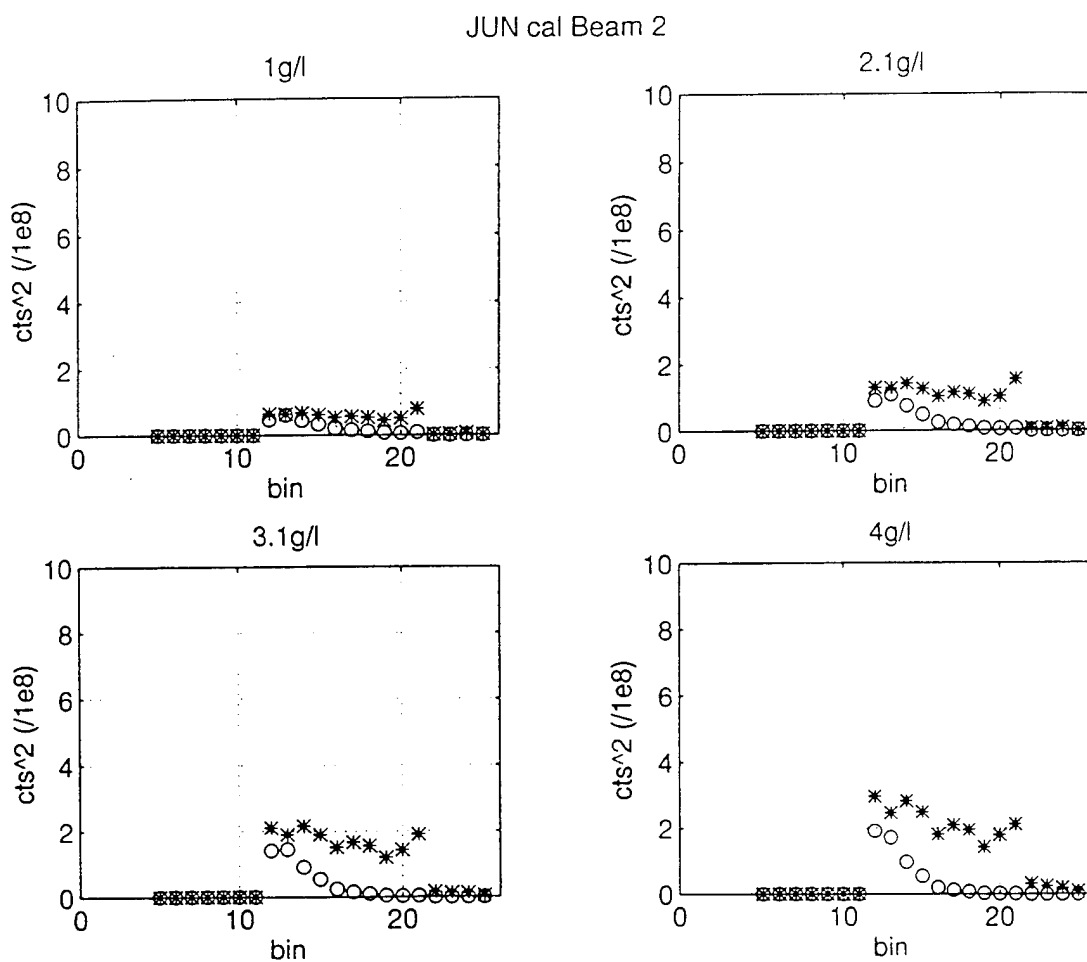


Figure 3.17b 5.3 MHz backscatter voltage for Beam 2 corrected for attenuation; o=uncorrected counts<sup>2</sup>, \*=corrected counts<sup>2</sup>.

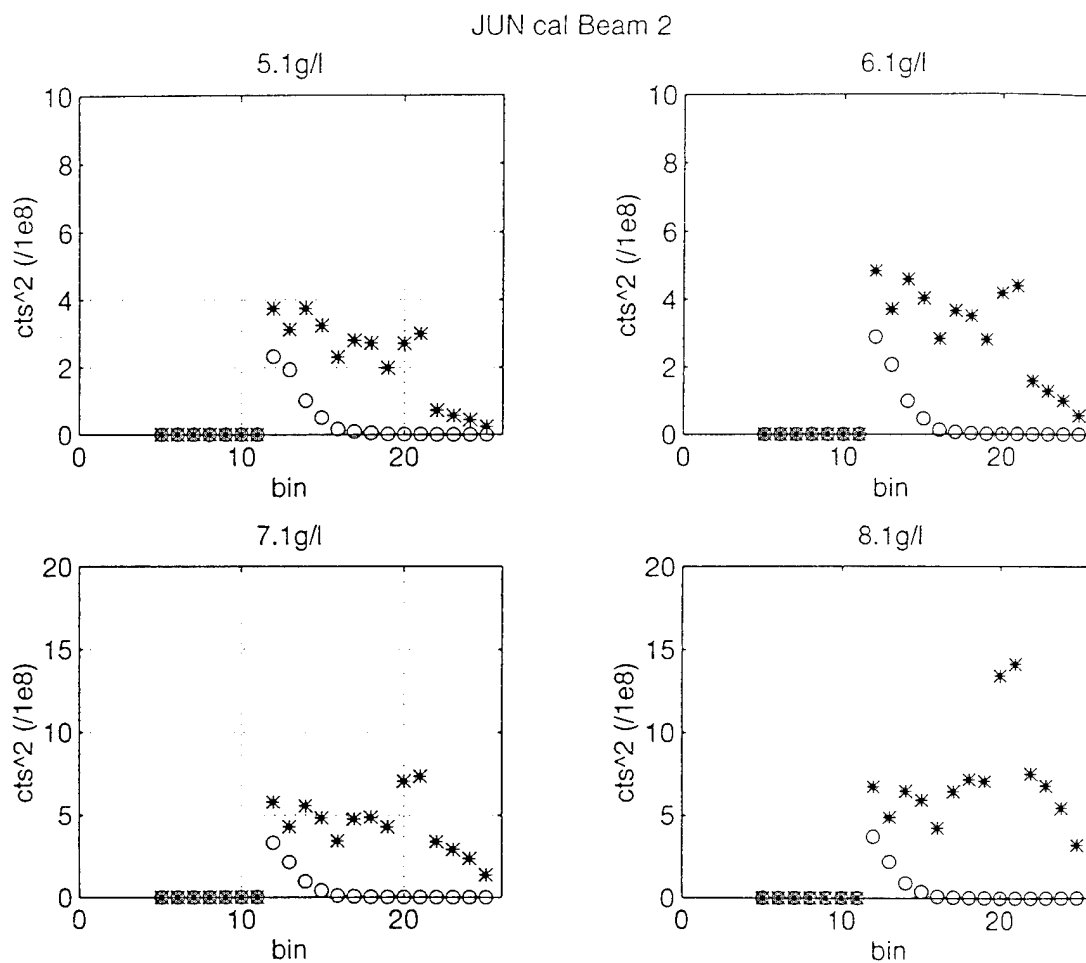


Figure 3.17c 5.3 MHz backscatter voltage for Beam 2 corrected for attenuation; o=uncorrected counts<sup>2</sup>, \*=corrected counts<sup>2</sup>.

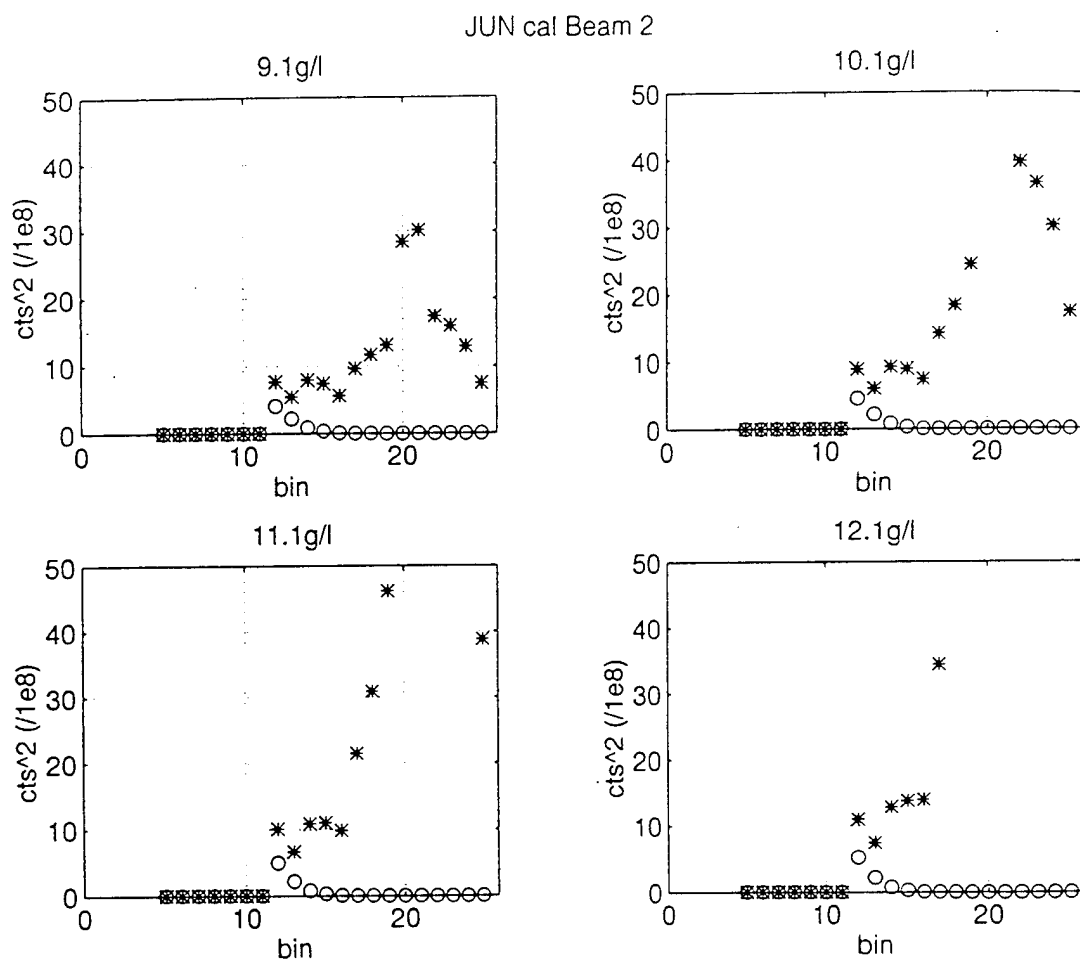


Figure 3.17d 5.3 MHz backscatter voltage for Beam 2 corrected for attenuation; o=uncorrected counts<sup>2</sup>, \*=corrected counts<sup>2</sup>.

facilitated the 1.3 MHz calculations, but because of the geometry of the instrument, resulted in a 50 to 80% window position for each of the 5.3 MHz beams (Figure 3.18a). An estimate of this window percentage was made by extrapolating the  $\alpha_s$  log-linear attenuation fit back to the window bin for each concentration (Figure 3.18b), and comparing this value (in counts space) with the actual counts reading in the window bin (Figure 3.18c). This extrapolated window bin value was also examined for use in the direct calculation method. Some error exists because the attenuation experienced in the first partial bin lowers the counts in the subsequent bins from which the extrapolation is performed; therefore the correction is not a completely true representation of absolute counts read by the instrument at higher concentrations.

The attenuation-corrected fit calibrates known mass with the attenuation-corrected counts<sup>2</sup> values described above. The calibration coefficient, again a linear regression to concentration, can be calculated using either a single value of the window bin or one bin beyond the window, or an average of the values in a selected number of bins beyond the window. The main advantage to this technique is its ability to correct for within-bin and partial window attenuation.

The optimization fit technique applies a range of  $C_m$  coefficients to the mass calculation in order to determine which value best corrects the data to the known sediment concentrations. The problem is two-dimensional; the performance of the coefficient must be satisfactory for the range of concentration at the first bin, and at bins further within the test volume. Therefore the optimization criteria selected is the average least squares fit of corrected to actual concentration for the three bins beyond the window. Results are described below.

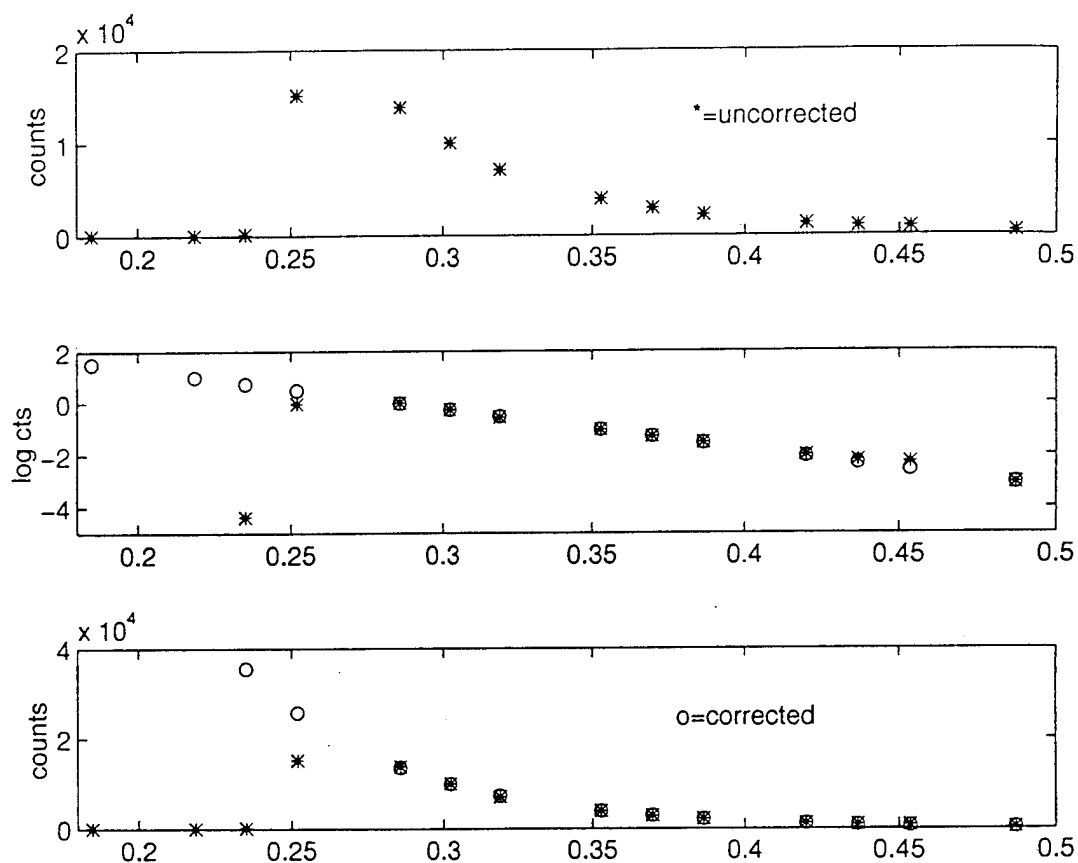


Figure 3.18 a) Recorded counts along Beam 2, 5.3 MHz profile. The window bin is at .25 m. b) Log of counts of the same profile ; 'o' = fit and back-extrapolation correction for ranges less than .28 m. c) Extrapolation correction in counts space. The partial window percentage is the ratio of the two values at .25 cm.

### **b. 1.3 MHz Mass**

Table 3-4 lists the  $C_m$  values calculated from the three methods. The window-bin counts<sup>2</sup> values used for the direct fit calculation are shown in Figure 3.19. The window bin for the 1.3 MHz calibration runs was examined for partial window effects with the back-extrapolation method described previously. At concentrations above 5 kg·m<sup>-3</sup>, calculations indicate that the instrument was seeing a full window of sediment. Below 5 kg·m<sup>-3</sup>, however, the reading is greater than the expected value. This effect is thought to be due to side lobe or small scale reverberation interference, and would cause the calculated  $C_m$  coefficient to be less than its actual value, especially when the fit is done only to these low concentrations.

The attenuation-corrected fit method used the counts<sup>2</sup> value one bin beyond the window, and the average of the values in four bins beyond the window (Figure 3.20). Because of the consistency of the attenuation correction through the medium, the averaging technique with more data points is favored.

The  $C_m$  values from the optimization technique were in close agreement and values ranged from 3.6 to 3.9 for fits from 4 to 25 kg·m<sup>-3</sup>. The corrected mass accuracy for the three bins beyond the window (approximately 7 cm) averaged 8% for the calculation to 8 kg·m<sup>-3</sup> and 11% for the calculation to 25 kg·m<sup>-3</sup> (Figure 3.21). The appropriate correction was therefore chosen to be 3.7 (x 10<sup>-8</sup> /kg·m<sup>-3</sup>); the corrected surfaces for both calibrations using this value are presented in Figures 3.22 and 3.23. Application of this coefficient to the noise floor backscatter level produced a minimum measurable concentration of 0 (1x10<sup>-4</sup> kg·m<sup>-3</sup>).

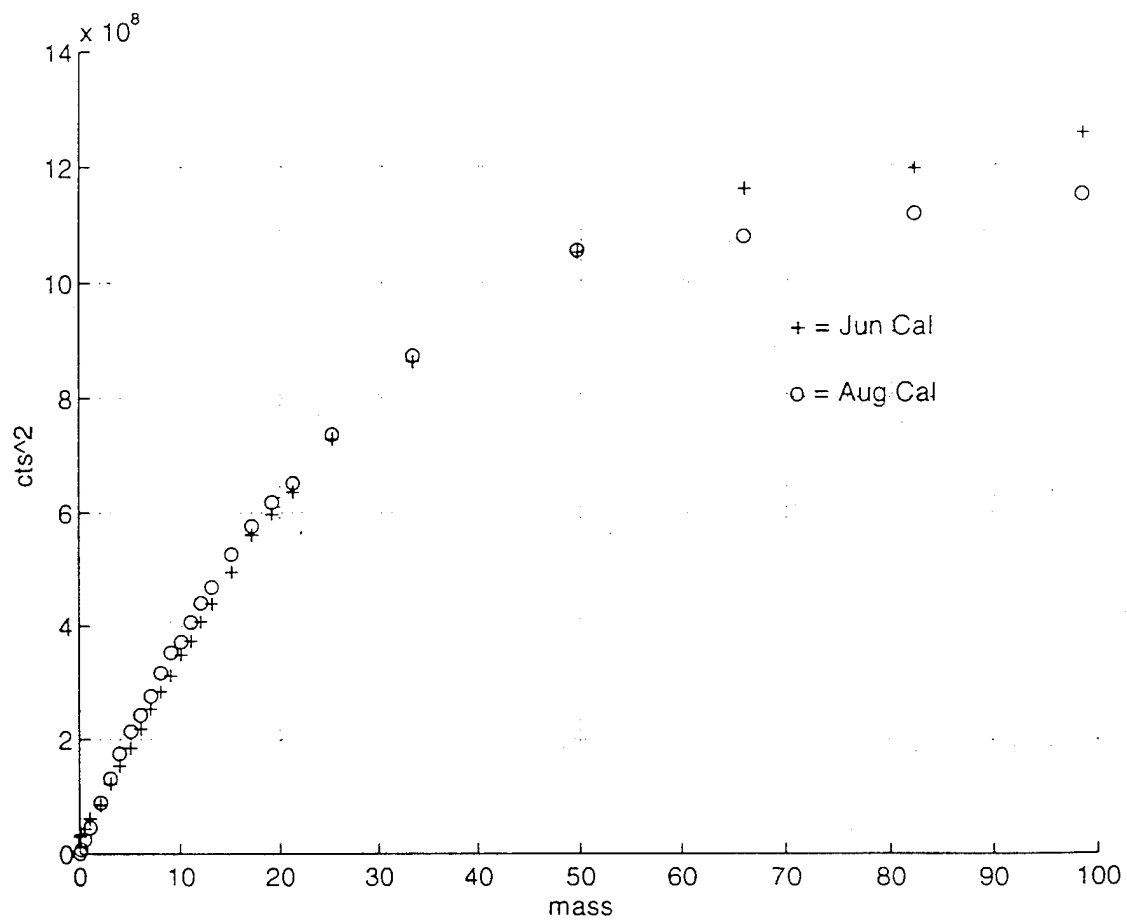


Figure 3.19 Direct fit method window bin values for 1.3 MHz.

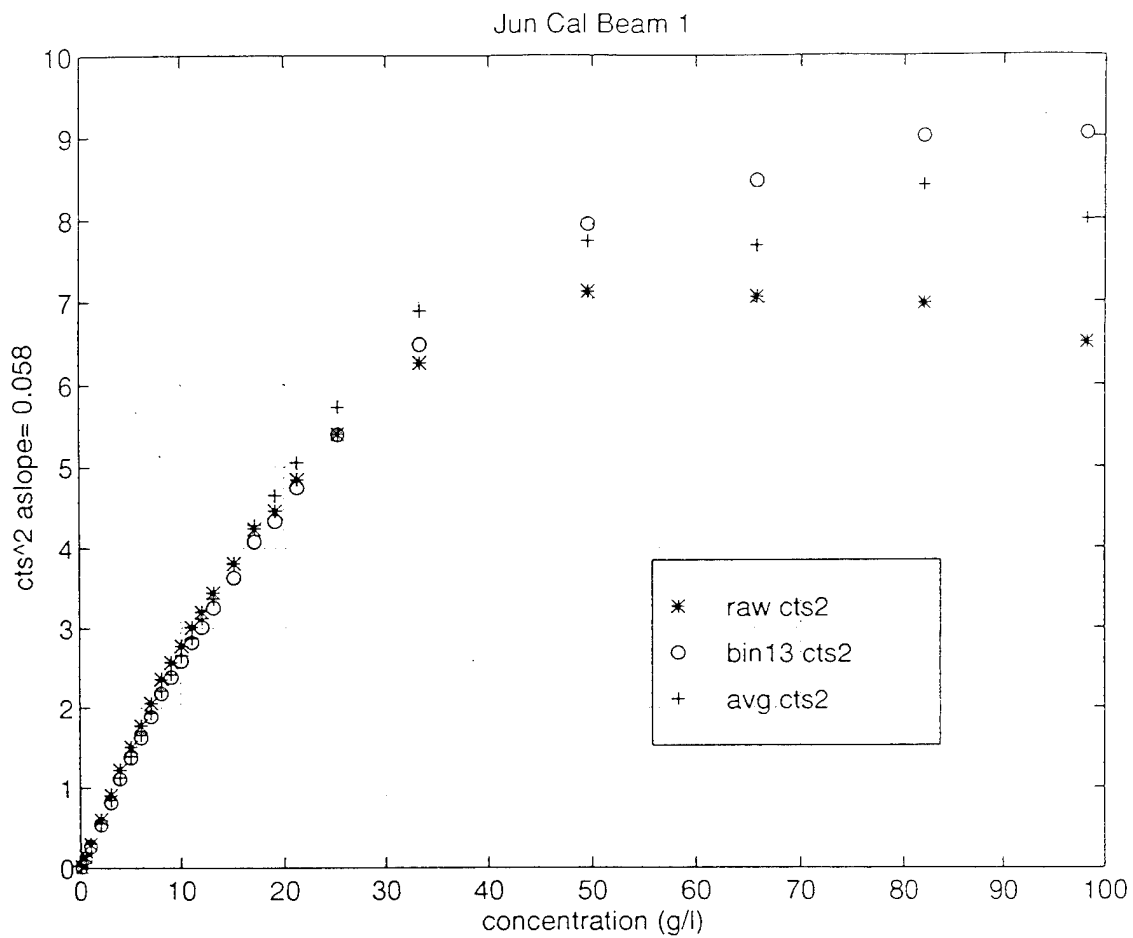


Figure 3.20 Attenuation-Correction method backscatter values for 1.3 MHz.



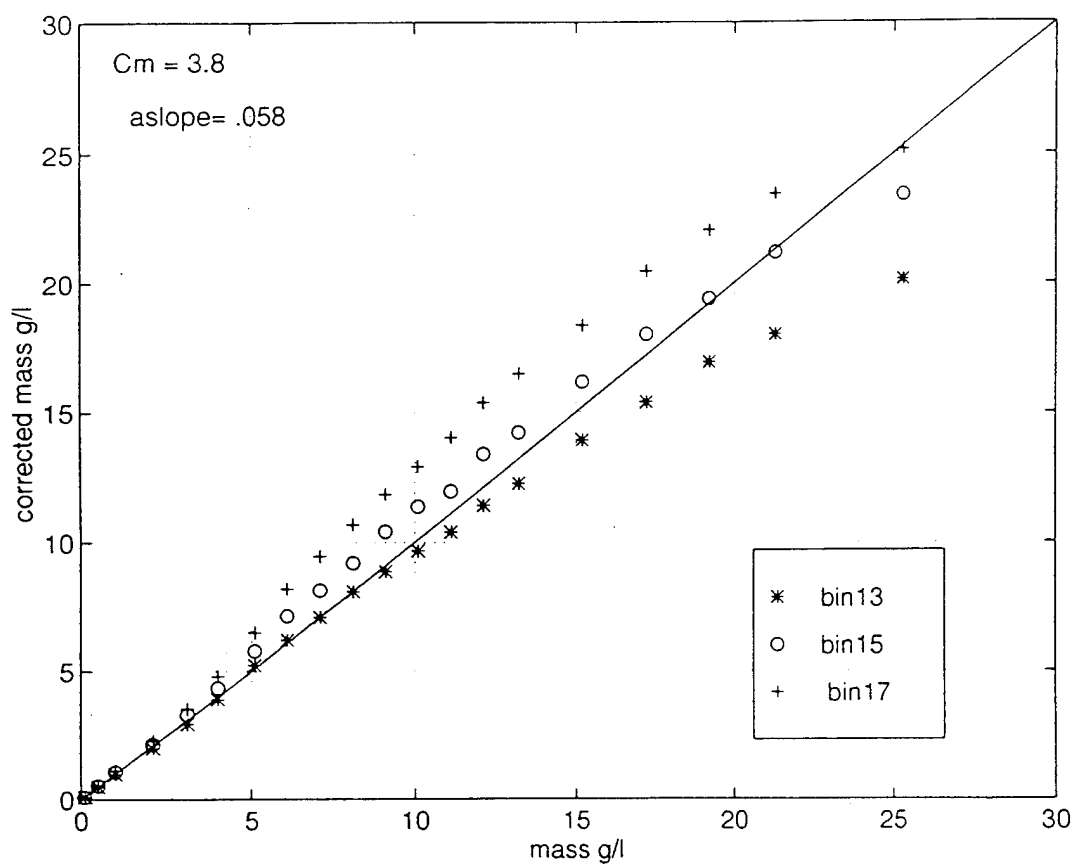


Figure 3.21 Optimization correction for Beam 1, August calibration.

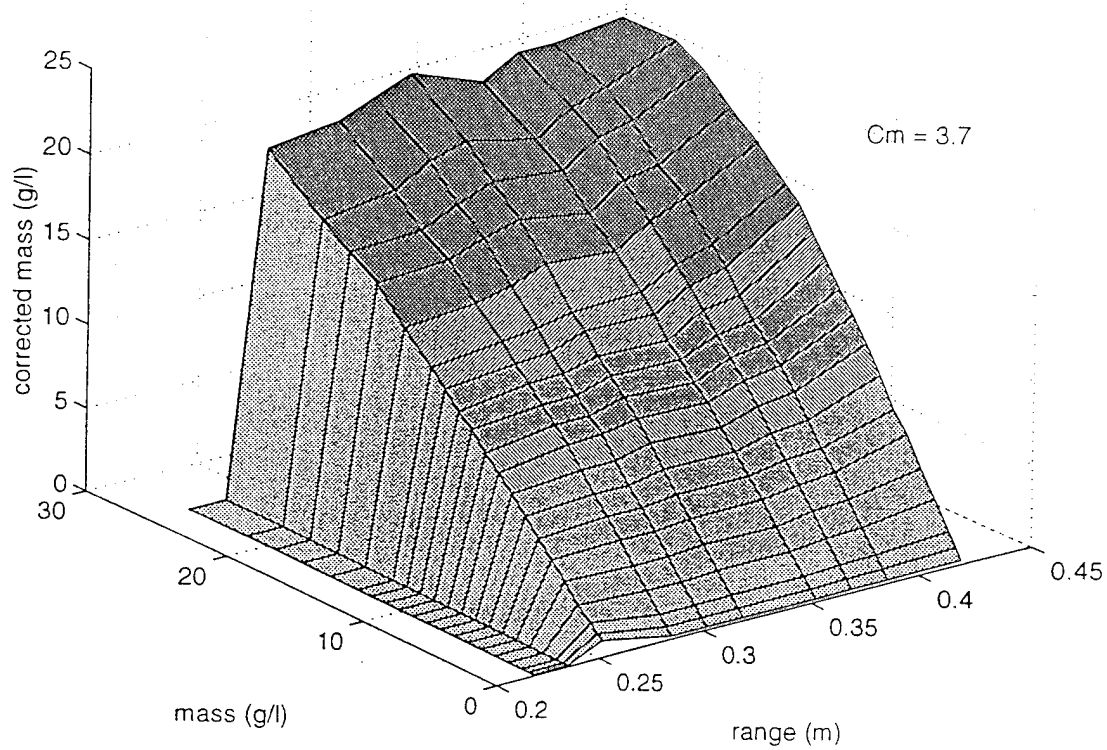


Figure 3.22 Corrected mass for Beam 1 June run using calibration  $C_m$ .

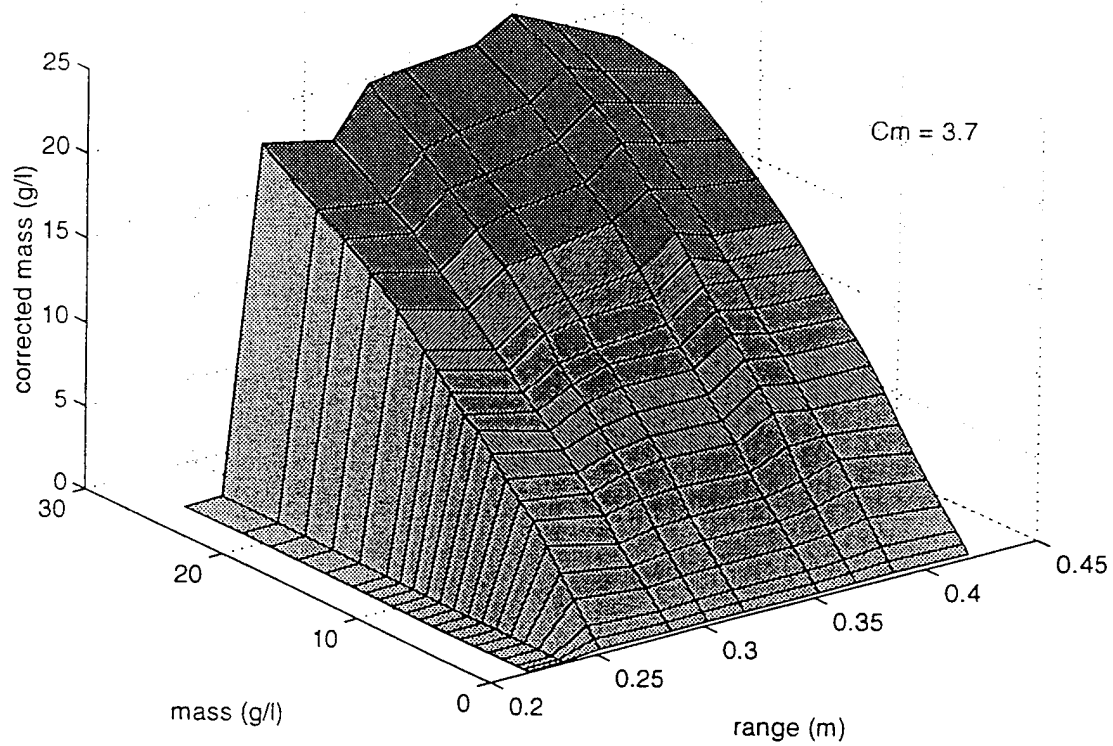


Figure 3.23 Corrected mass for Beam 1 August run using calibration  $C_m$ .

Method:	Direct		Att-Corr (bin)		Att-Corr (avg)		Optimization	
Limit:	8 g/l	25 g/l	8 g/l	25 g/l	8 g/l	25 g/l	8 g/l	25 g/l
June	2.7	3.1	4.1	4.4	3.3	3.8	3.6	3.9
August	2.8	3.2	3.8	4.2	3.3	3.6	3.5	3.9

Table 3.4 Beam 1  $C_m$  Coefficient Calculated Values

**c. 5.3 MHz Mass**

$C_m$  values for the 5.3 MHz calculations are given in Table 3.5. The procedures for the 5.3 MHz beams were complicated by the partial window geometry of the experiment configuration, as described above. Figure 3.24 displays the window bin, bin beyond the window, and corrected window bin readings for beam 2 of the June calibration. Direct fits done to the corrected data yielded values less than those of the optimization method, which would follow from the inaccuracy of the extrapolation method which was discussed above.

Attenuation-correction fit method calculations were sensitive to the partial window value, and to the choice of single or averaged bin technique. The results of this computation are illustrated in Figure 3.25. The 3-bin average method yielded a coefficient 1/10 lower than the single bin beyond the window calculation. Examination of the counts<sup>2</sup> corrections (Figures 3.17a-d ) suggests that, due to the spread of the corrected values, the single bin method is more reliable. Values in Table 3.5 were calculated using the single bin method and the window percentage calculated from the back-extrapolation method. An inaccuracy of this technique which may have more effect on the 5.3 MHz than the 1.3 MHz instrument is the introduction of the known mass at the window bin; if this value is higher than the concentration actually seen at the window interface, the difference could cause a low  $C_m$  coefficient.

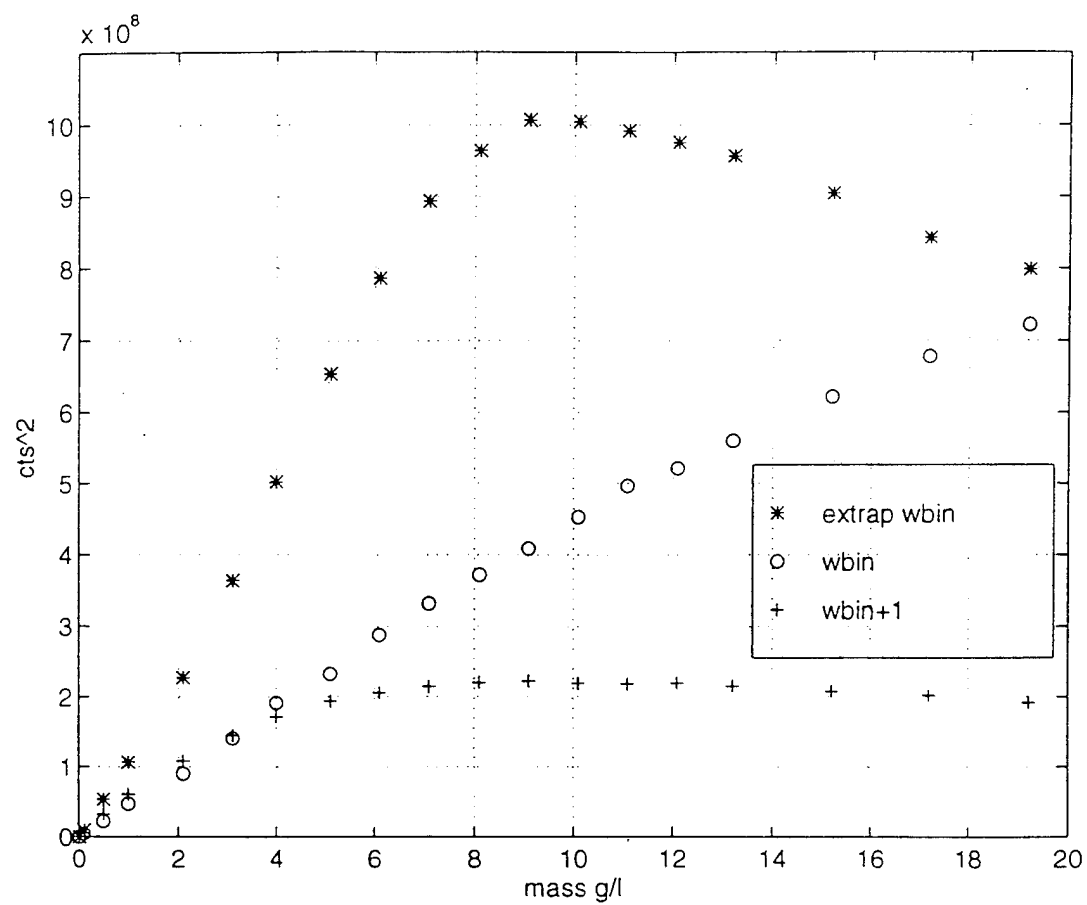


Figure 3.24 Beam 2, June calibration values of backscatter pressure at the window bin and one bin beyond, and corrected window bin values used in the direct fit method.

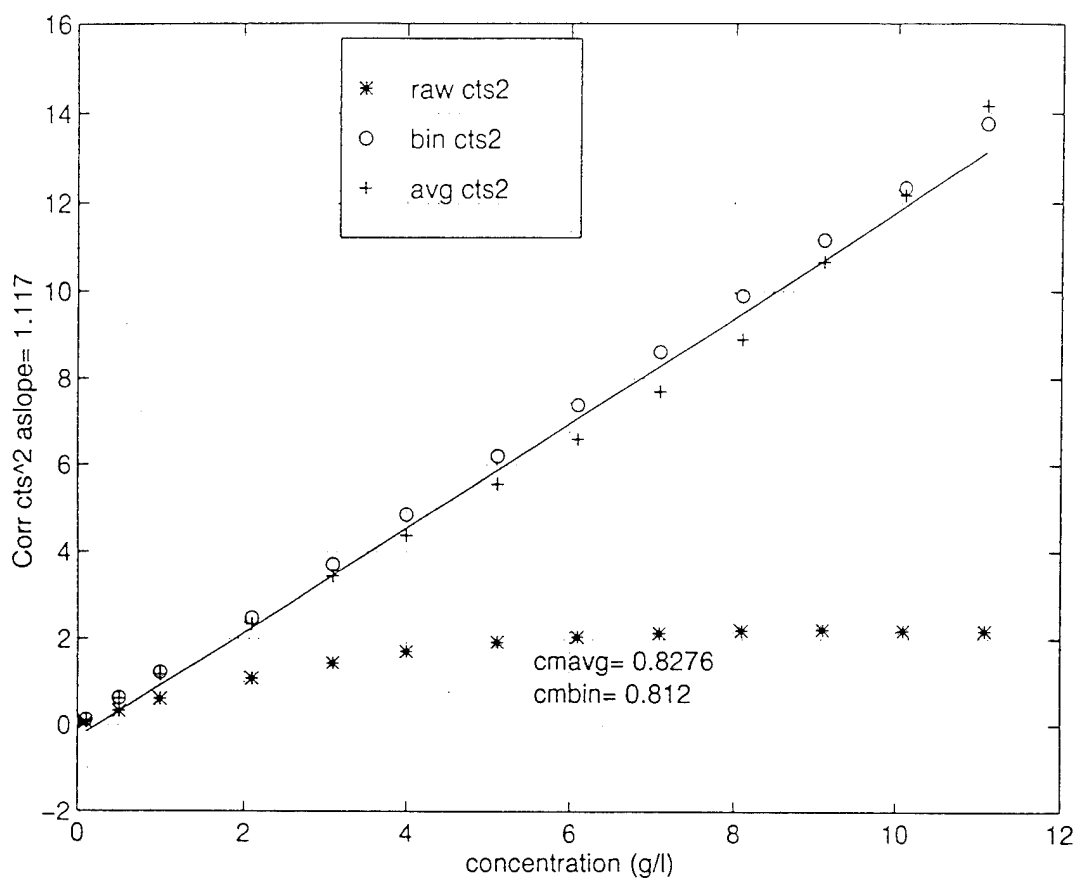


Figure 3.25 Beam 2 June calibration attenuation-correction backscatter values.

The optimization method proved to be the most reliable technique for deriving an accurate  $C_m$  for the 5.3 MHz beams. The method was used with a window correction, and best fits made to  $4 \text{ kgm}^{-3}$  (Table 3.5). Best fits to  $8 \text{ kgm}^{-3}$  varied only .01 ( $\times 10^{-8} / \text{kgm}^{-3}$ ) from these values. The corrections were consistent to 3 bins beyond the window (Figure 3.26). Both the June and August calibrations were accurate to 7-8% of the actual concentration to  $8 \text{ kgm}^{-3}$ . The values selected as the calibration coefficients were therefore an average of these coefficients. The coefficients for the different beams differ due to transducer and electronic-specific gain characteristics; beam 4 was consistently lower than the other two beams in all calibration derivations. A representative corrected surface for the 5.3 MHz calibration is presented in Figure 3.27. The minimum measurable concentration for the 5.3 MHz beams is  $O(1 \times 10^{-5} \text{ kgm}^{-3})$ .

Method:	Direct	Att-Corr	Optimum	Calibration	%Wbin
B2 June	0.80	0.78	0.95	0.93	0.62
B2 August	0.96	0.84	0.90	0.93	0.82
B3 June	0.86	0.81	1.00	0.98	0.58
B3 August	0.87	0.88	0.97	0.98	0.73
B4 June	0.67	0.64	0.78	0.77	0.66
B4 August	0.69	0.68	0.76	0.77	0.74

Table 3.5 5.3 MHz Beam  $C_m$  Coefficient Calculated Values to  $4 \text{ kgm}^{-3}$

### 3. Full Optimization

The successful use of the  $C_m$  optimization routine leads to the speculation that a double-optimization, which also includes likely values of *aslope*, would confirm the

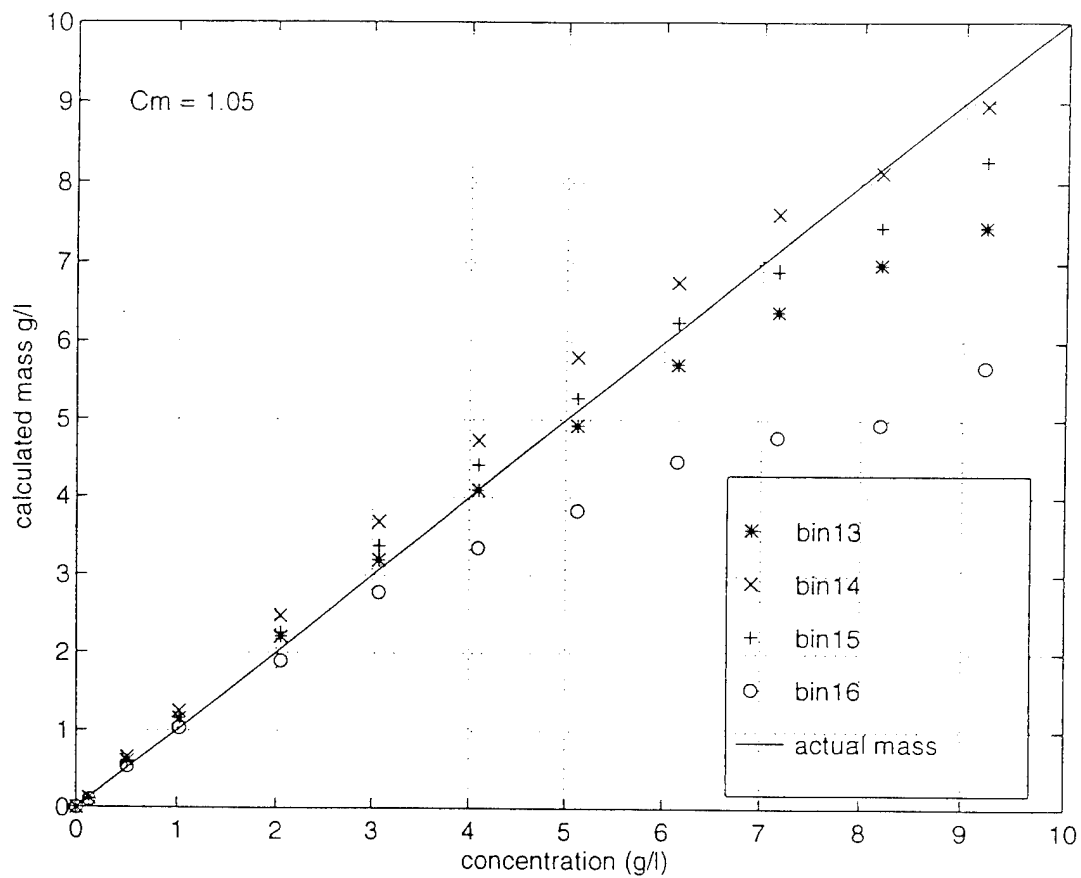


Figure 3.26 Optimization results for Beam 2.



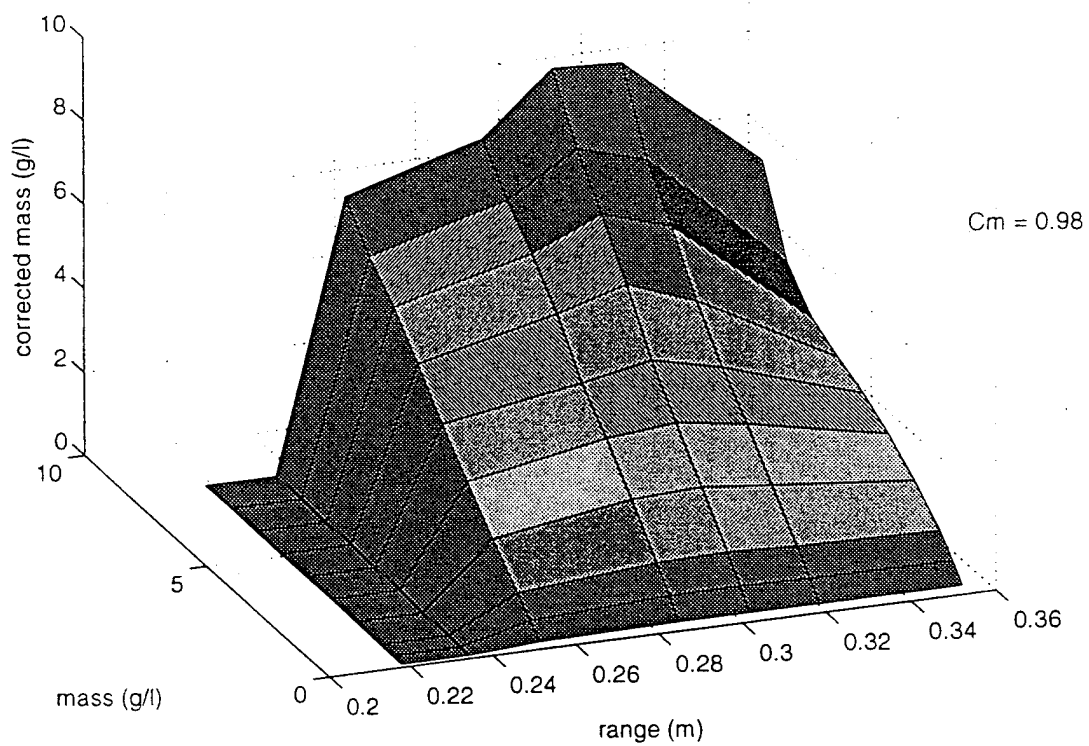


Figure 3.27 Corrected mass for Beam 3, August run using calibration  $C_m$ .

calibration. For the 1.3 MHz beam, this appears to be so, (Figure 3.28), although the spread of satisfactory *aslope* coefficients is quite broad. On the other hand, the optimization map for the 5.3 MHz beam is a multi-valued surface (Figure 3.29). This is attributed to the nonlinear form of the integration (Equation 3.3), and the high attenuation values for the higher frequency beam. The optimization evaluates the fit of a data line which originally curves downward toward higher concentration values; the  $C_m$  coefficient determines the slope of the corrected line, and the *aslope* coefficient determines the degree to which the data points are brought up to that line. It is therefore conceivable that more than one set of values would optimize the correction, especially in the heavily attenuated 5.3 MHz case. Because the attenuation correction described here is considered appropriate, and the precise optimization values depend upon the criteria chosen for optimization (averaged number of bins beyond the window, etc), the double optimization is not used for attenuation coefficient calculation.

## E. GRAIN SIZE DISCRIMINATION

The grain size discrimination capability of the CASP is based on the implicit inclusion of the form factor  $F[\lambda]$  in the calibration coefficient  $C_m$ . Because both sonar frequencies were calibrated to the same sand sample, the ratio of the corrected masses should be unity. If we assume that the sand size spectrum is represented by a lognormal distribution, the absolute ratio of the actual form factors, (Figure 3.30), would then be normalized by a secondary calibration coefficient,  $F_{cal}$ , (in this case equal to 0.625) so that the ratio at 0.09 mm radius, 1.2 standard deviation (i.e. calibration sand) would be one. Should the ratio in the field deviate from unity, this secondary coefficient would be reapplied to estimate the actual grain size. It follows from the above calibration description that the performance of the grain size discriminator will be limited by the 5.3 MHz beam. Figures 3.31 and 3.32 show that this is the case. For both calibration runs, the mass ratio is

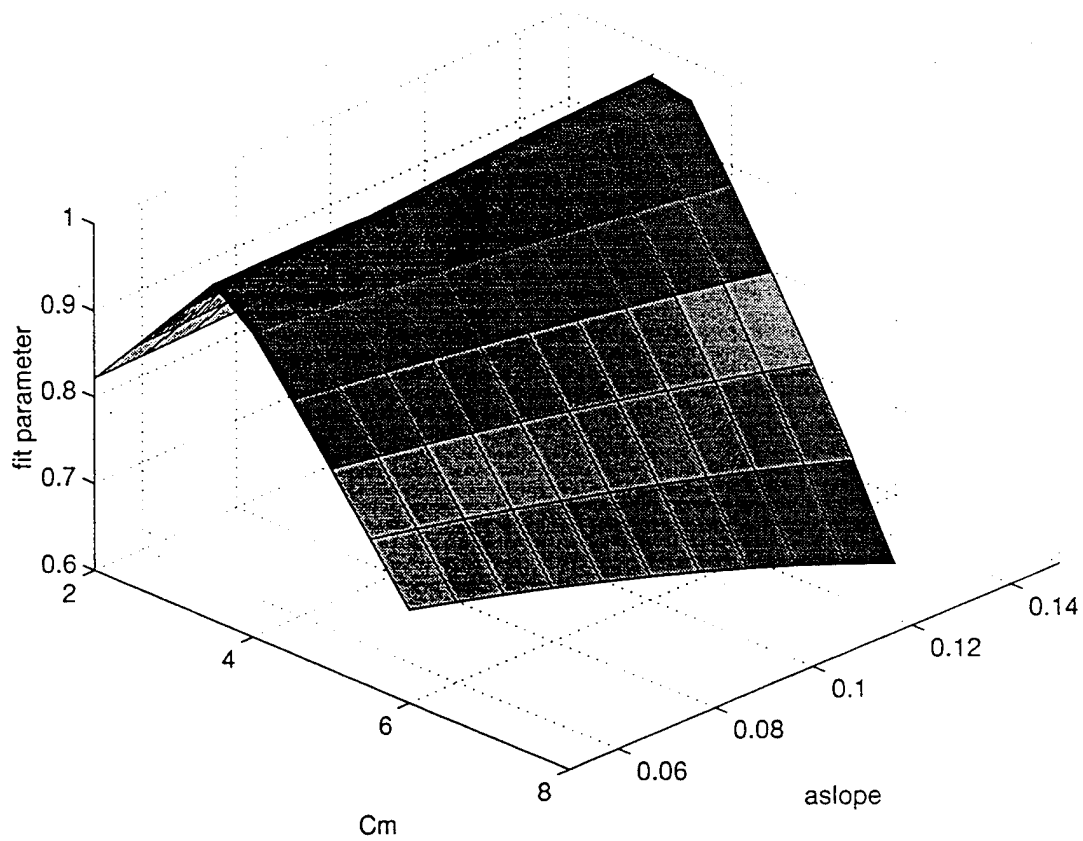


Figure 3.28 Full optimization of 1.3 MHz beam.

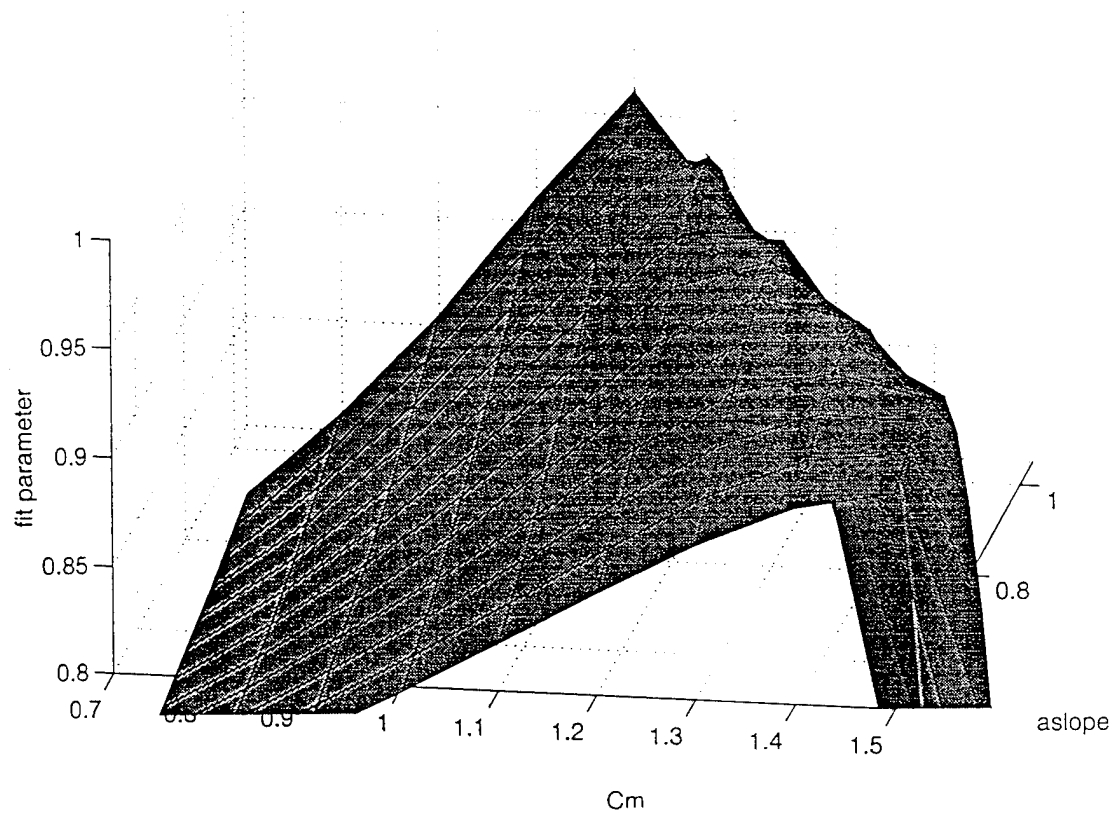


Figure 3.29 Full optimization of 5.3 MHz beam.

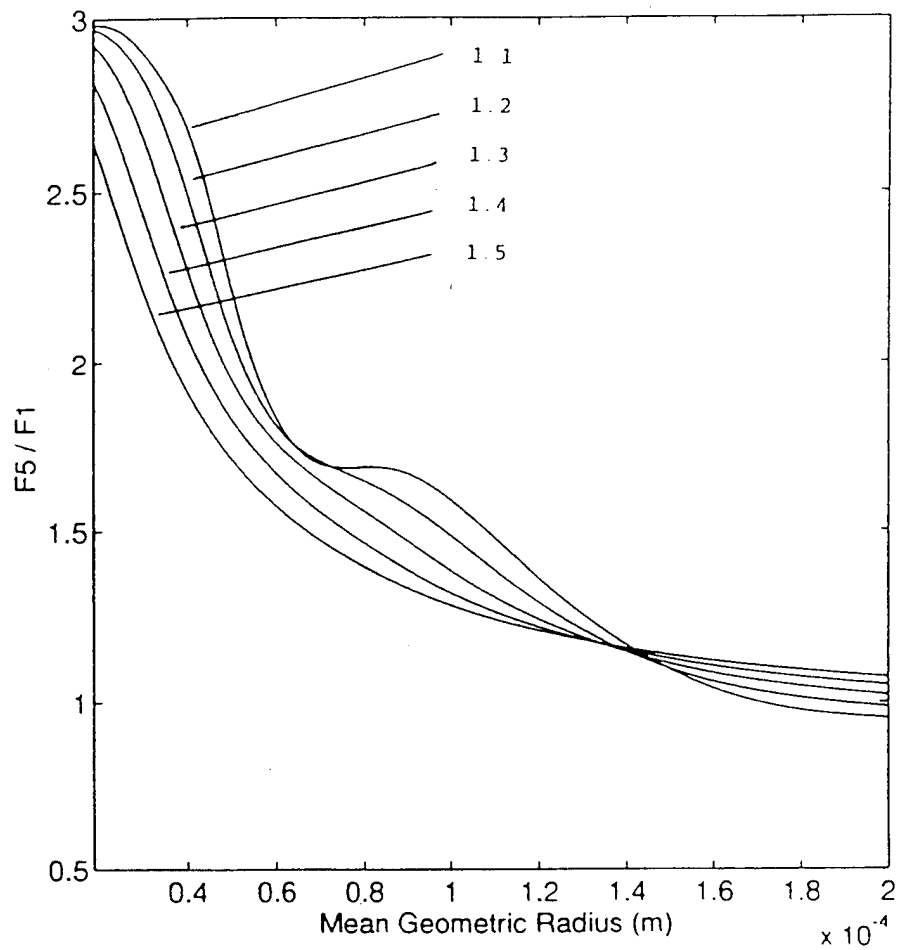


Figure 3.30 Theoretical values of  $F(X_5, \sigma_g)/F(X_1, \sigma_g)$  as a function of  $a_g$  for  $\sigma_g = 1.1, 1.2, 1.3, 1.4, 1.5$ .

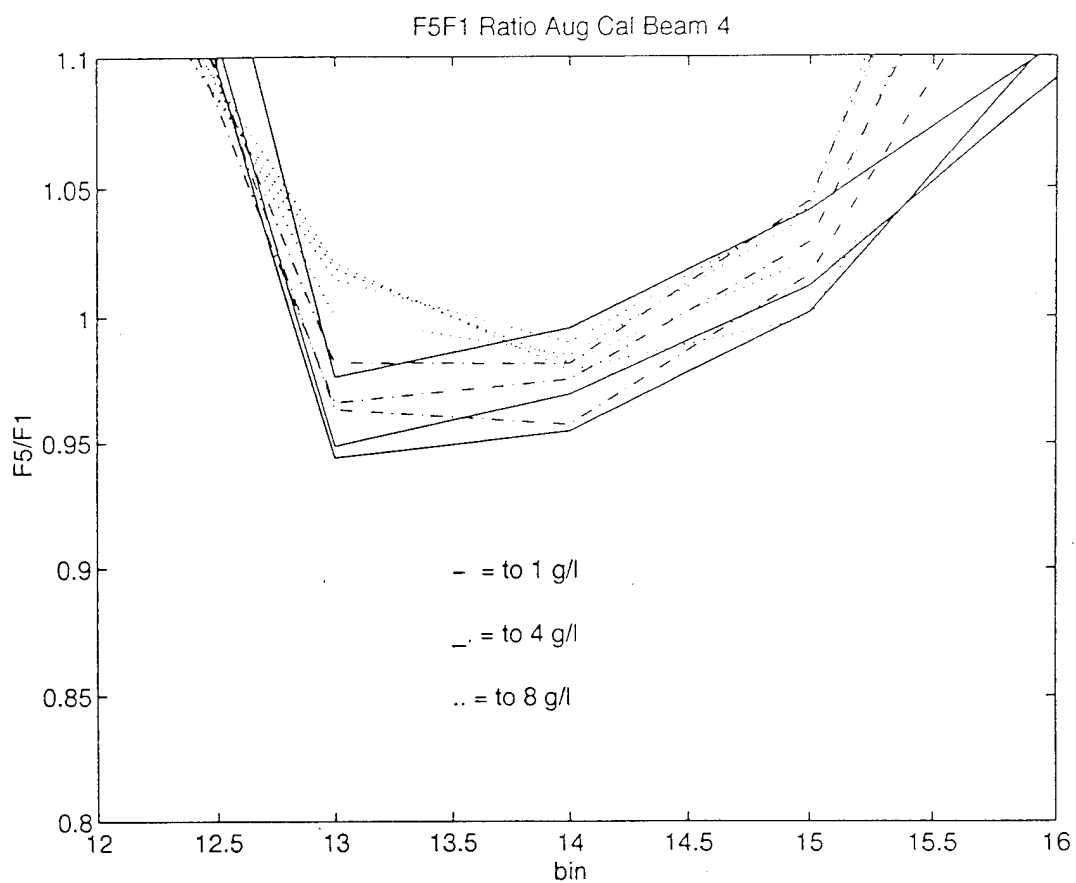


Figure 3.31 F5/F1 ratio for August calibration, Beam 1 and 4.

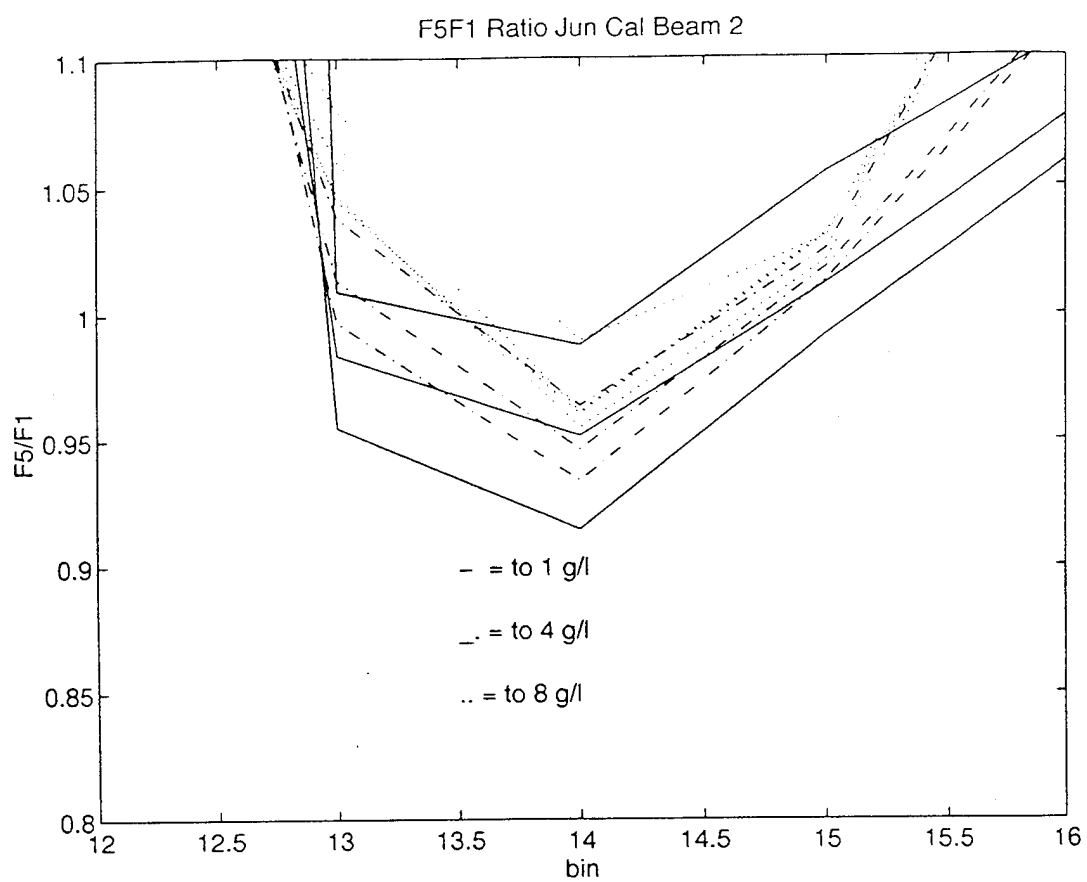


Figure 3.32 F5/F1 ratio for June calibration, Beam 1 and 2.

consistent to approximately 10% at concentrations less than  $8 \text{ kg m}^{-3}$  and distances less than 7 cm. It is reasonable to expect that the instrument will be able to detect mean grain size variations of more than approximately 0.03 mm in light sediment conditions.



## IV. FIELD DEPLOYMENT

### A. SITE DESCRIPTION

The CASP was deployed as part of a multi-instrument package installed on a movable sled during the DUCK 94 experiment in October 1994 at the U.S. Army Corps of Engineers' Field Research Facility (FRF) in Duck NC. Dr. E.B. Thornton and T.P. Stanton were co-principal investigators for the instrument sled. The CASP was mounted on a computer controlled hydraulic arm which allowed it to be positioned at selected heights from the bottom. The sled was deployed daily from 6 to 20 Oct along a cross-shore transect starting at or seaward of the sand bar and towed across the surf zone. Data were acquired by stopping at 4 to 8 stations along the transect each day as the sled was dragged shoreward. At each station, the CASP performed an approximately one hour profile which began by positioning the beam intersection point (25 cm from the face of the CASP) as closely as possible to the bottom, and stepping the instrument up in approximately one bin (1.68 cm) increments. Each increment, termed a substation, was two to ten minutes long. At each station, five to twenty substations were recorded.

Data records from Oct 20th were chosen to illustrate CASP capabilities because of its strong low frequency wave forcing and absence of bubble contamination. Of four stations recorded that day, the farthest station from the beach, Station 1, contained the most consistent substation records. The positions of the four stations are noted on a bathymetric profile of the experiment area, Figure 4.1. At Station 1 the sled was located on the shoreward slope of the offshore bar, on an incline of approximately 2 cm/m. The small scale bathymetry of the area, measured with altimeter and side scan sonar mounted on a specialized nearshore survey vehicle (CRAB), was relatively smooth, and consisted of one to two cm ripples approximately every five meters. Grain size analysis performed 10 meters south of the sled transect (Stauble, 1995) revealed a sand population with a slightly smaller

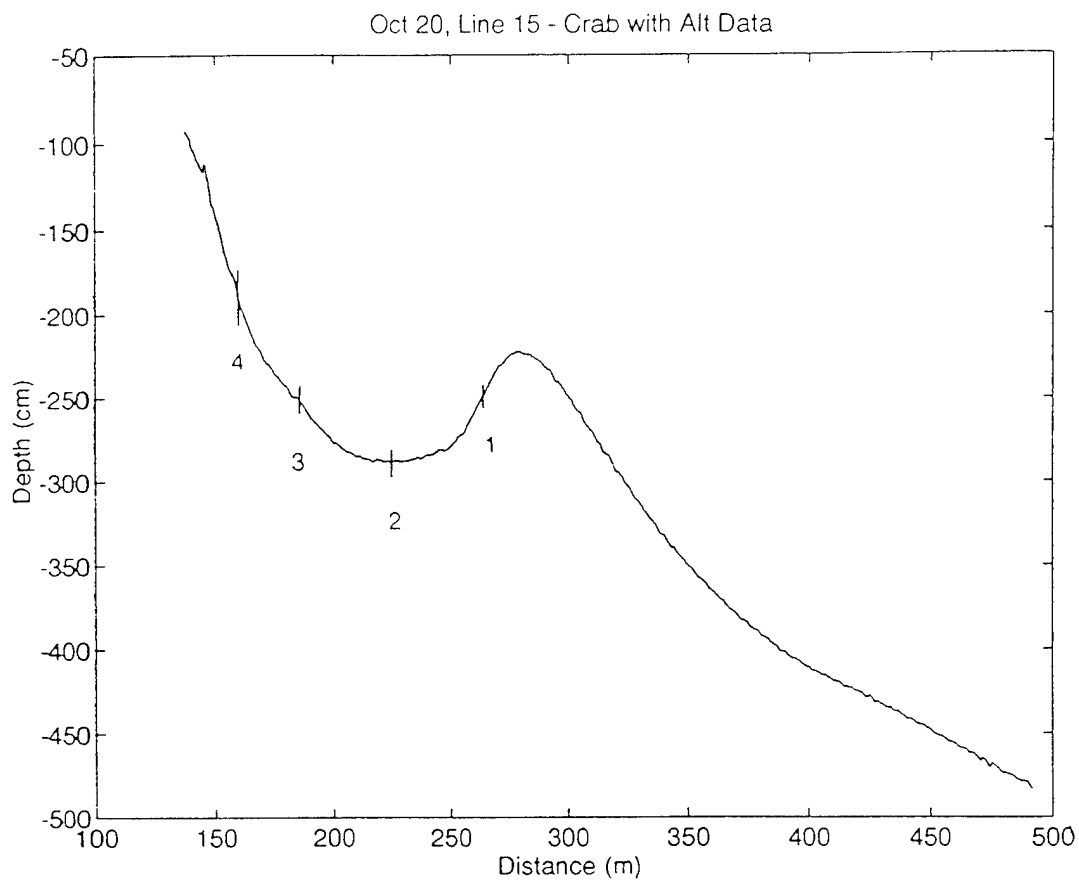


Figure 4.1 Bathymetric profile of the sled transect on 20 Oct 94. Data collection stations are numbered.

geometric mean radius than the calibration sand (Table 3.1). The narrow band wave field on October 20th had an incidence angle of  $4^\circ$ , with a regular period of 14 seconds, group period of approximately 2 minutes, and significant wave height of one meter at 8 meters depth. The wave frequency-direction spectrum for that day, Figure 4.2, illustrates the narrow banded directional spectrum. The longshore current was negligible and varied by  $\pm 0.2$  m/s.

## **B. SEDIMENT VS. VELOCITY PHASE ANALYSIS**

### **1. Background Theory**

An analysis of the correlation of sediment and cross-shore flow with height above the bed is presented for day 20 to illustrate the capabilities of the CASP. Current theory for suspended sediment distribution in pure oscillatory flow over a smooth bed hypothesizes that the maximum concentration just above the bed occurs simultaneously with the maximum bed shear stress. The time of this maximum bed shear stress has been calculated as a phase lag from the maximum wave velocity outside the boundary layer [Fredsoe and Diegaard, 1992]. Above the bed, maximum concentration lags the maximum bed shear stress to an increasing degree with height. Figure 4.3a [Justesen and Fredsoe 1985] shows the expected concentration relative to bed concentration at 1.8 cm above bed level for a full wave cycle as predicted by three hydrodynamic approaches described in Fredsoe and Diegaard [1992]. Each of these models assumes forcing by a symmetrical sinusoidal wave form, and predicts that the maximum concentration will be equal under both inshore and offshore flow conditions. Variation of concentration with wave phase at different heights above the bed was calculated by Fredsoe et al [1985] (Figure 4.3b) using time-variant eddy viscosity and bed concentration based on the Shields parameter [Fredsoe and Diegaard, 1992]. Using a grain diameter of 0.18 mm, the  $Z/K_n$  (depth/bed roughness) parameter equates to the

FRF 8-m Array Frequency-Direction Spectrum  
 Date: 20 Oct 94 at 1300 EST for 136.53 min with 160 dir  
 $H_{m0} = 1.13$  m  $f_p = 0.074$  Hz  $T_p = 13.56$  sec  $\theta_p = -4.0$  deg  
 depths: min = 7.73 m mean = 7.79 m max = 7.90 m at gage 191

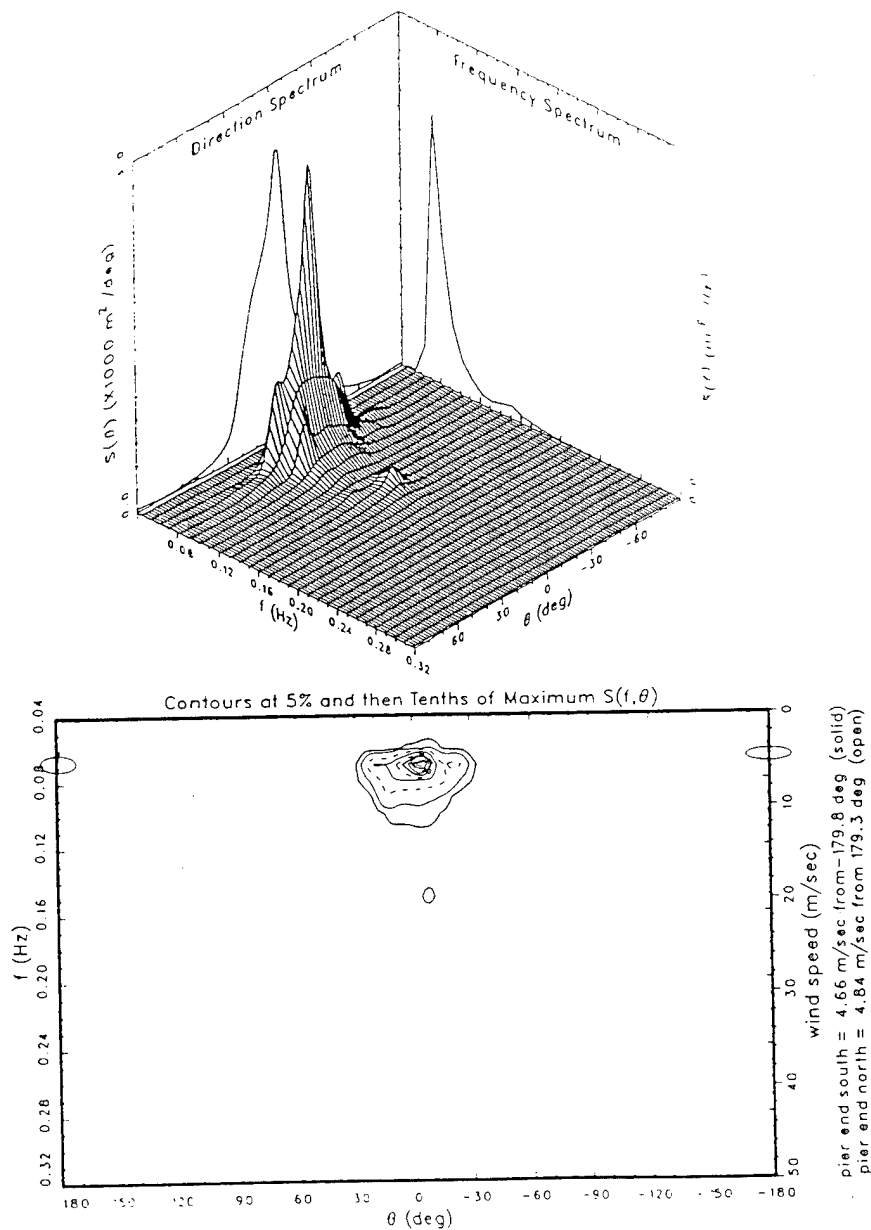
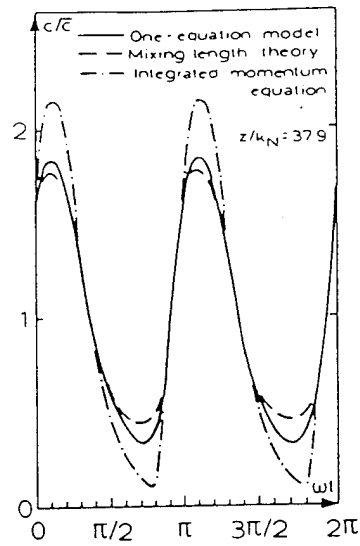
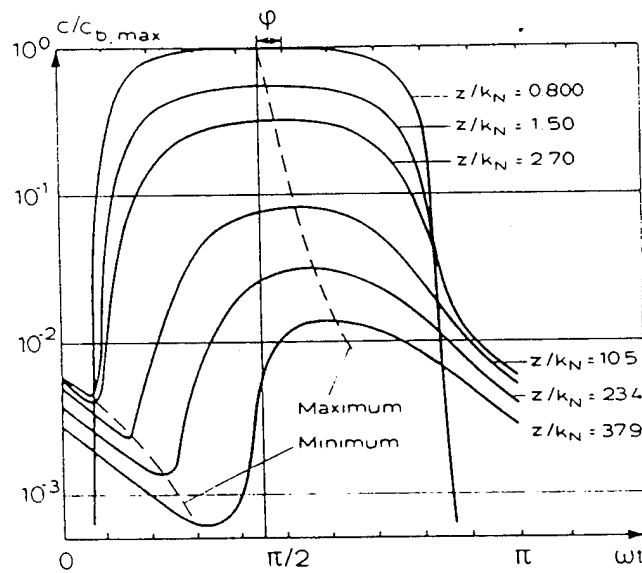


Figure 4.2 Wave spectrum data from Duck, N.C., for 20 Oct 94.



A



B

Figure 4.3 a) Comparison between three hydrodynamic approaches to estimating eddy viscosity. (From Justesen and Fredsøe, 1985). b) Variation in concentration with time at different heights from the bed. (From Fredsøe et al., 1985).

following heights (Table 4.1):

$Z/K_n$	0.800	1.5	2.7	10.5	23.4	37.9
$Z$ (cm)	.036	.067	.121	.47	1.05	1.70

Table 4.1  $Z$  for  $Z/K_n$  using grain diameter of 0.18 mm

With the addition of time variant eddy viscosity, the maximum concentration at 1.7 cm shifts to approximately  $\pi/2$ , or time of maximum cross-shore velocity.

Sediment behavior over a rippled bed becomes much more complex, and requires numerical solution of the flow equations. Using a discrete vortex model under symmetrical forcing, Hansen et al [1991, 1994] calculated the flow field over a ripple bed at various wave phases. Then, with a Lagrangian formulation, the paths of the individual sand grains were followed. The calculated pattern of suspended particles at two phases of a wave cycle are illustrated in Figure 4.4.

## 2. Phase Mapping Method

A typical time series of cross-shore velocity and sediment concentrations at one to three bins (2 to 7 cm) above the bottom at Station 1 is shown in Figure 4.5 (positive velocities are offshore). The correlation of maximum onshore velocity (therefore maximum bed stress) with concentration at the bottom (bin 1), and the decorrelation with height (bins 2 and 3 correspond to 3.4 and 5.1 cm above the bed), is readily apparent. In order to more quantitatively analyze this correlation, a phase mapping display is used. The velocity time series was broken into wavelengths using a zero-down crossing technique, so that a full period is defined as the beginning of onshore flow (negative  $v$ ) to the end (post-maximum) of offshore flow. The concentration (or  $u, v, w$  magnitude) time series can then be separated into these same time defined full periods, and the data ensemble averaged relative to phase.

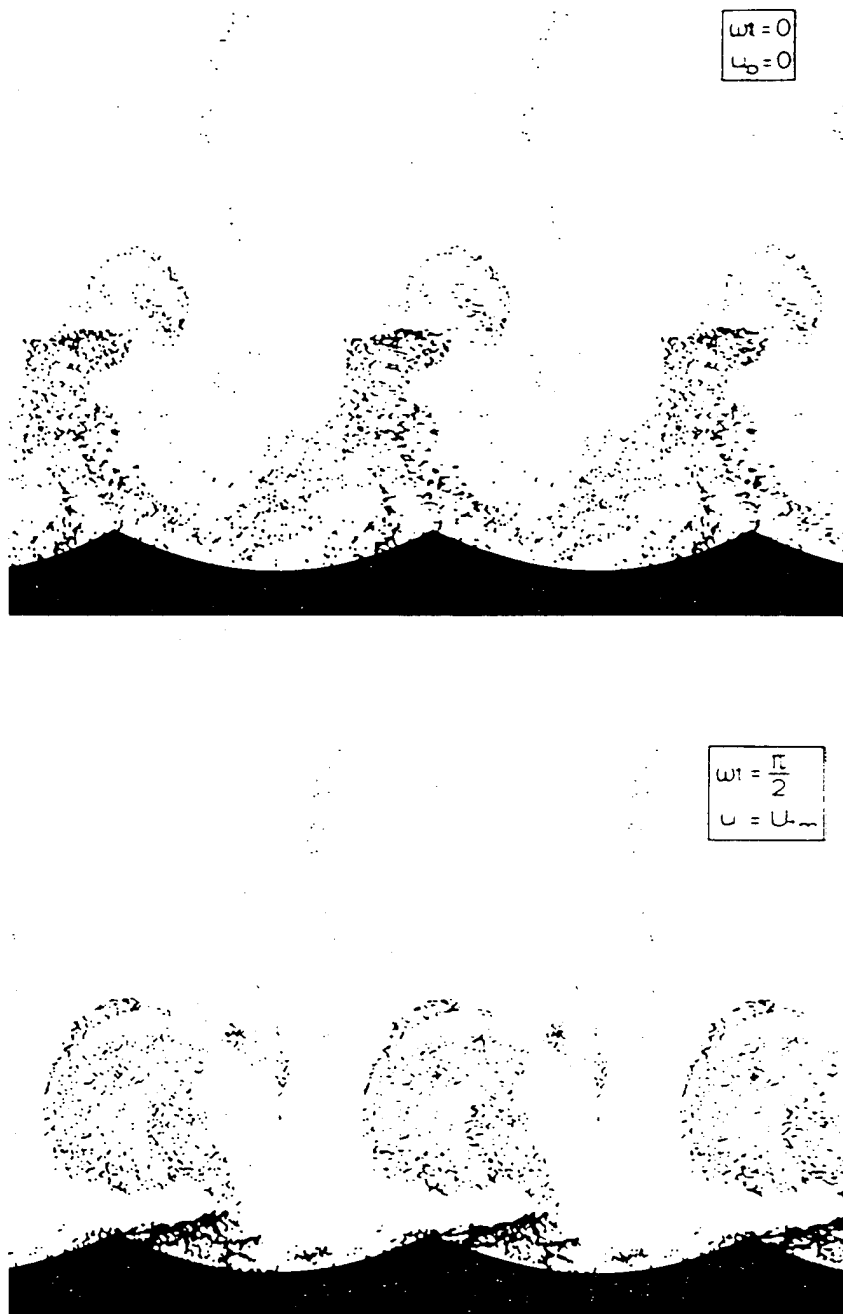


Figure 4.4 Modeled path of suspended sediment particles over a rippled bed at two phases of a wave period. (From Hansen et al., 1991).

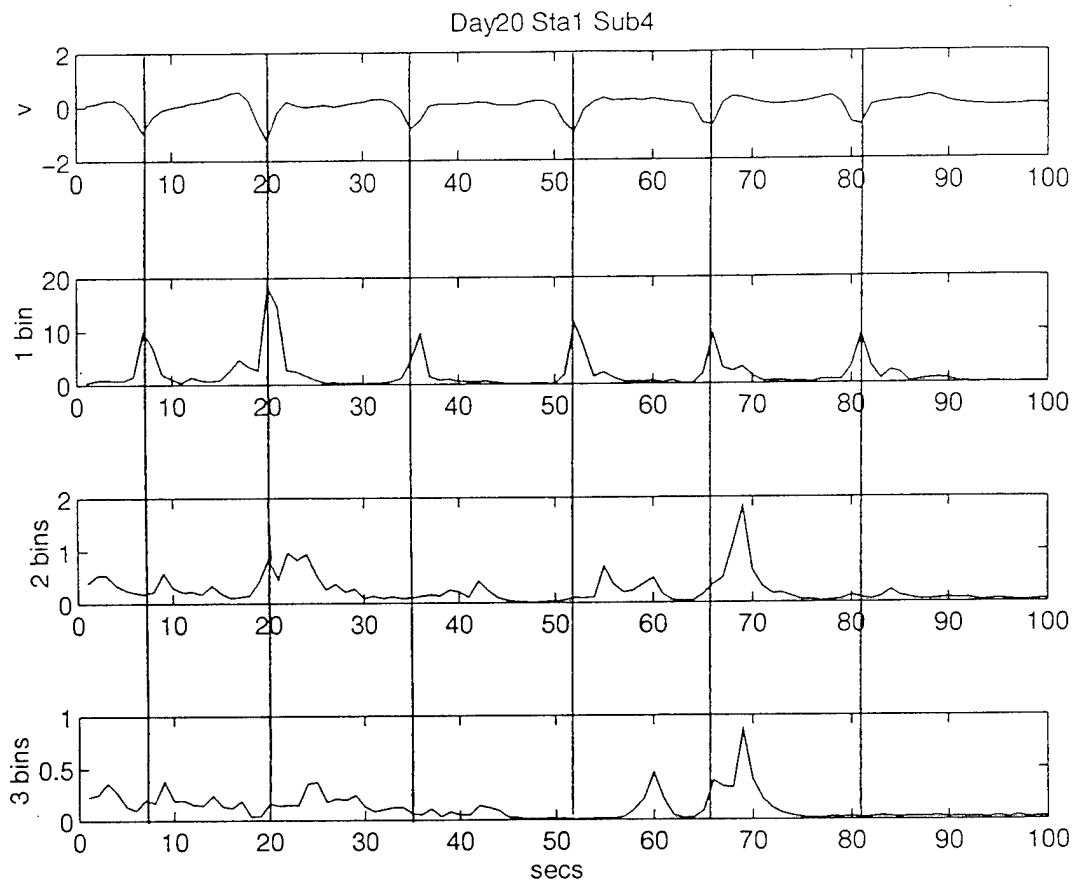


Figure 4.5 Cross-shore velocity and concentration at one, two, and three bins above the bottom for a segment of the Duck data record.



A typical 10 minute substation record consists of over 40 cycles for the 14 second period waves observed on the 20th of October. For this study, each 360 degree period was divided into 5 degree segments for averaging. The correlation of the cross-shore velocity magnitude with its own phase was first examined to determine the shape of the cross-shore wave, and to detect any variation of the velocity with elevation from the bed. At Station 1, six substation measurements were taken starting with velocity measurement at the bed (Bin 12, 25 cm from the face of the CASP), and at elevations of up to 12 cm from the bed. The shape of the velocity wave was consistent at each height (Figure 4.6). It is uniformly asymmetrical, with the offshore maximum at  $56 \text{ degrees} \pm 3 \text{ degrees}$  through the water column. The asymmetry of these narrow banded waves are indicative of strong nonlinearities in shallow water waves. The velocity magnitudes at the bed were somewhat less than those above, as expected.

### 3. Concentration Data

Results of the mapping of mass concentration as a function of wave phase are shown for four substations in Figures 4.7 to 4.10. At the bed, the maximum mass concentration is clearly correlated with the maximum onshore velocity, but consistently decorrelates one bin (3-4 cm) from the bed. Note that the concentration ranges span from  $O(50)$  to  $O(10^{-4}) \text{ kg m}^{-3}$ . The behavior observed in these plots can be related to a simple conceptual model in which sand is injected into the water column from the boundary layer as described by time-variant eddy viscosity theory (Figure 4.3b), except that, under these asymmetric waves, the injection only occurs at the onshore phase. Above the boundary layer, the sand distribution is controlled by advection and turbulence in the water column.

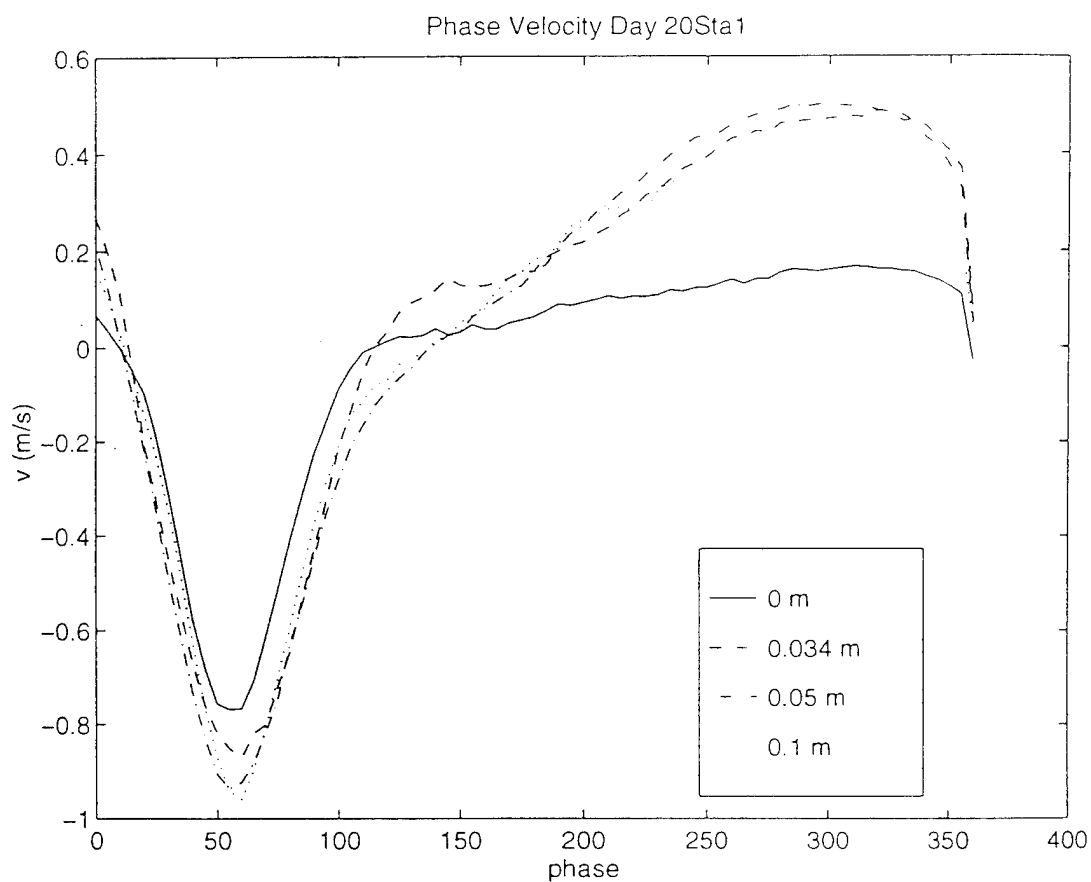


Figure 4.6 Cross-shore velocity magnitude mapped on its phase. The different line styles represent various elevations of the measurements (i.e. CASP beam intersection) above the bottom.

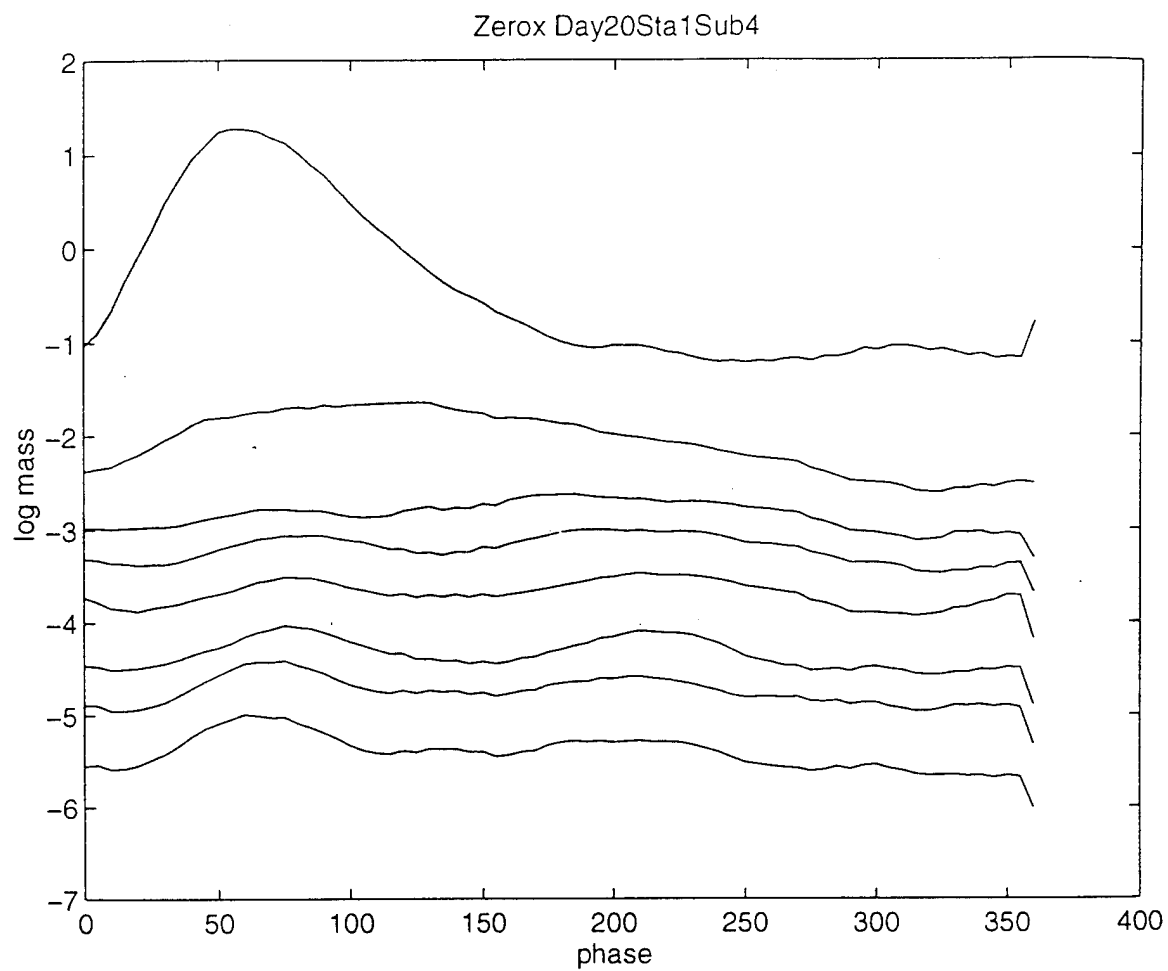


Figure 4.7 Log mass profiles of phase-mapped sediment from 20 Oct, Station 1, Substation 4. The upper profile is the bottom bin, with range from the bed increasing with decreasing log mass in one bin steps to an ultimate elevation of 18 cm.

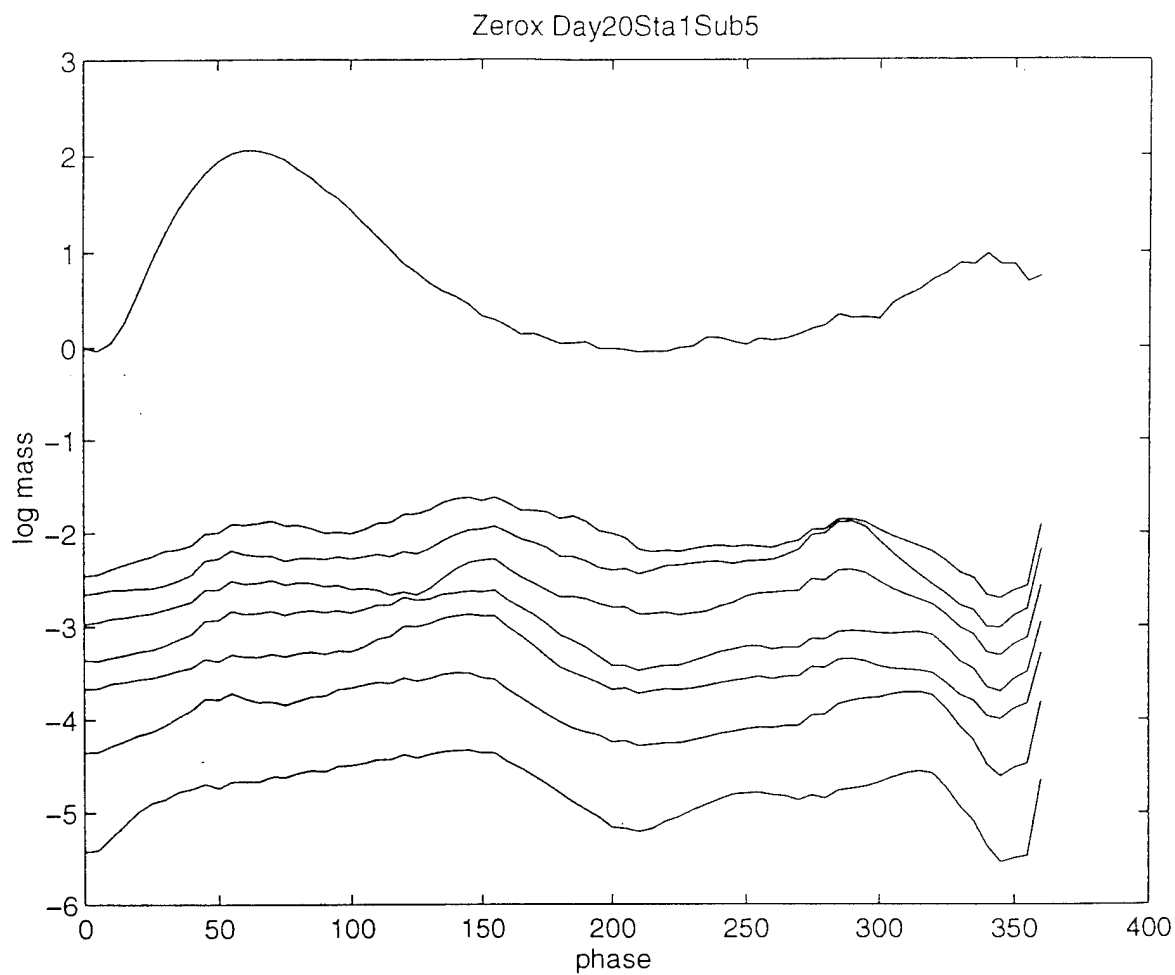


Figure 4.8 Log mass profiles of phase-mapped sediment from 20 Oct, Station 1, Substation 5. The upper profile is the bottom bin, with range from the bed increasing with decreasing log mass in one bin steps to an ultimate elevation of 18 cm.

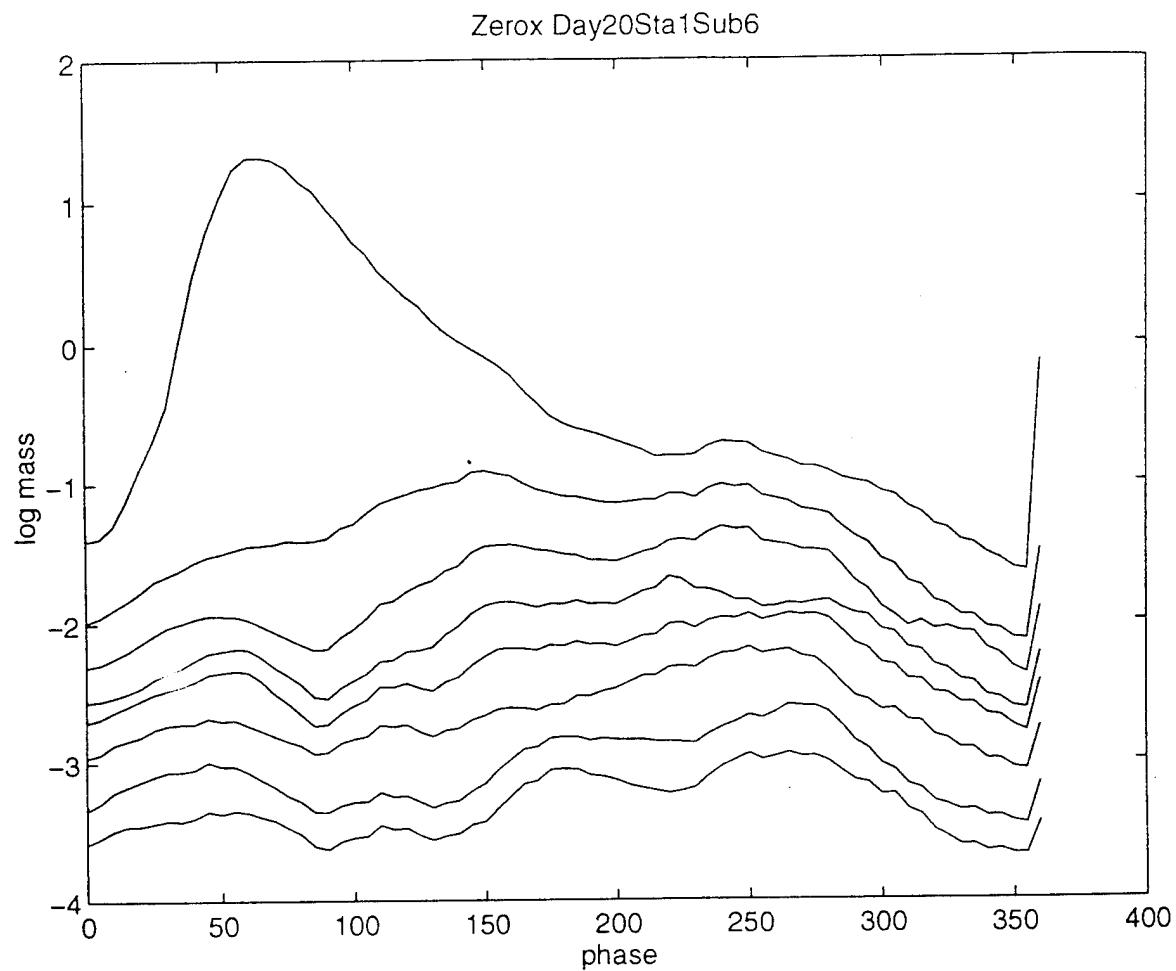


Figure 4.9 Log mass profiles of phase-mapped sediment from 20 Oct, Station 1, Substation 6. The upper profile is the bottom bin, with range from the bed increasing with decreasing log mass in one bin steps to an ultimate elevation of 18 cm.

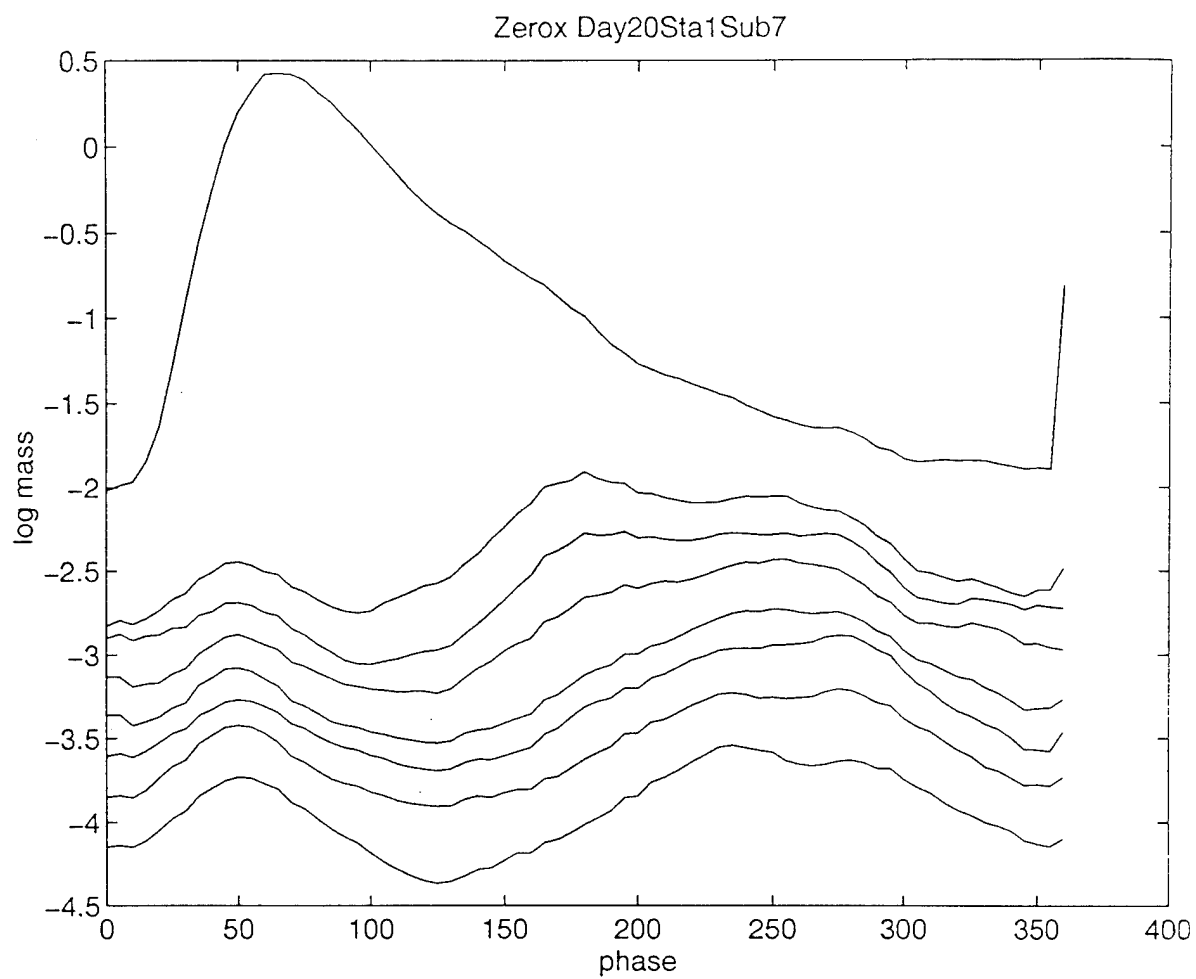


Figure 4.10 Log mass profiles of phase-mapped sediment from 20 Oct, Station 1, Substation 7. The upper profile is the bottom bin, with range from the bed increasing with decreasing log mass in one bin steps to an ultimate elevation of 18 cm.

#### 4. Sediment Flux

Sediment flux, the product of velocity and concentration, and can be calculated with elevation as the mean flux for a given time period (here, a substation), or represented in phase space. Mean fluxes for four substations of Station 1 are presented in Figure 4.11. For the phase space calculations, the difference in the velocity profile taken at the bottom bin and the profiles taken above the boundary layer (Figure 4.6), can be accounted for by using the boundary layer velocity profile to determine sediment flux at the bottom bin of each of the other stations. Figure 4.12 is an example of this calculation for substation 5. The majority of the transport occurs in the bottom boundary layer, with a small amount of onshore transport higher in the water column.

#### C. GRAIN SIZE DISCRIMINATION

As described by equation 3.1, the  $F5/F1$  value is proportional to the square root of the ratio of the mass measured by the 1.3 MHz sonar to the mass measured by the 5.3 MHz sonar. The proportionality coefficient, 0.65, derived in the calibration section, was applied to the calculated ratio so that a corrected  $F5/F1$  value of 1.6 indicates sediment of the same lognormal characteristics as the calibration sediment. Table 4.2 lists the corrected  $F5/F1$  ratios for each substation of Station 1, the height of the measurement above the bottom, and the max and mean sediment measured by the 1.3 MHz beam. Table 4.3 lists these same values for Station 2 data. When the intersection point is at the sediment bed, the magnitude of sediment concentration exceeds the expected limits for satisfactory performance by the grain size discriminator. The actual depth of the bottom bin within the boundary layer is also subject to an uncertainty of 1.68 cm, and is probably responsible for the difference between the ratios at substations 4 and 10 of Station 1. For these reasons, the ratios at the bottom bin are not considered reliable.

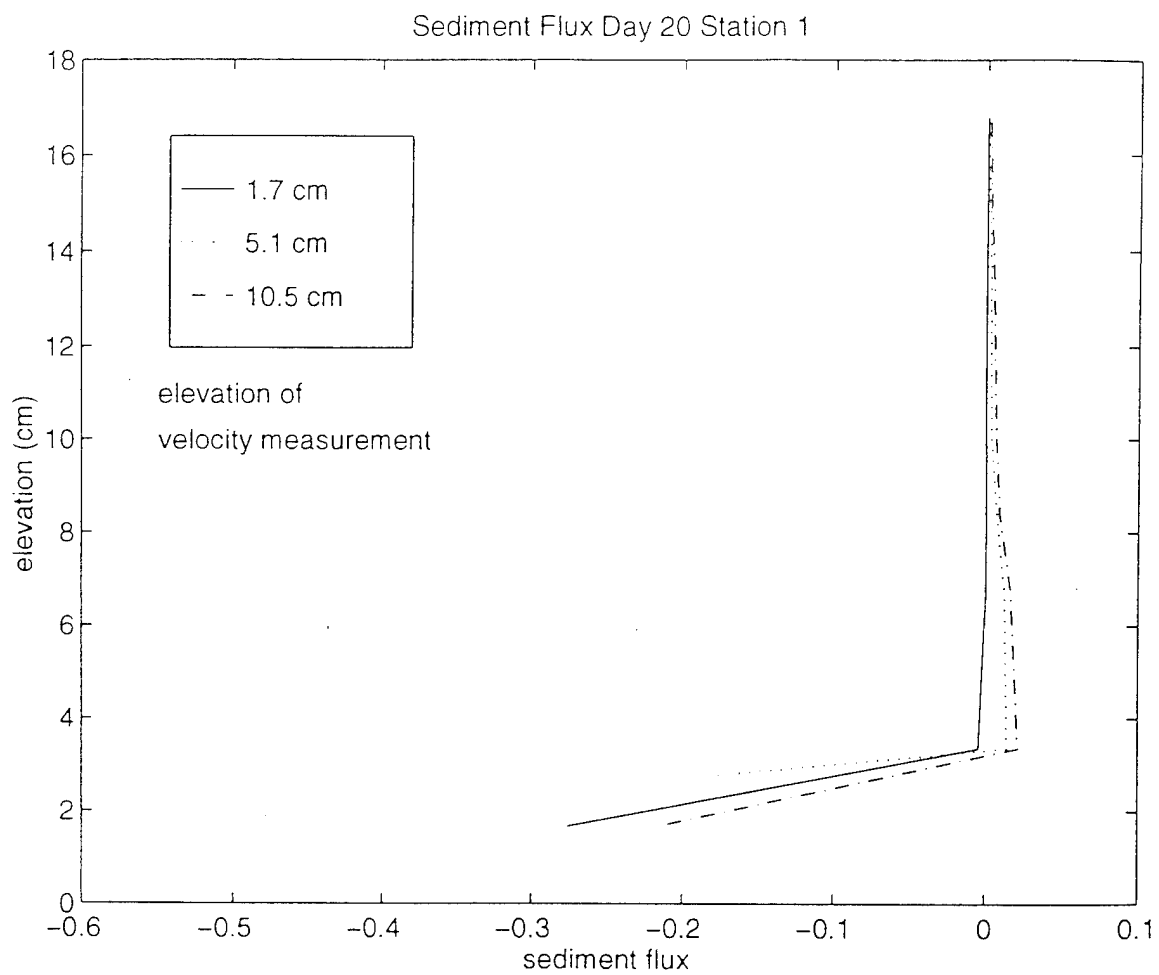


Figure 4.11 Mean sediment flux measurements at four substations of Station 1, Day 20.



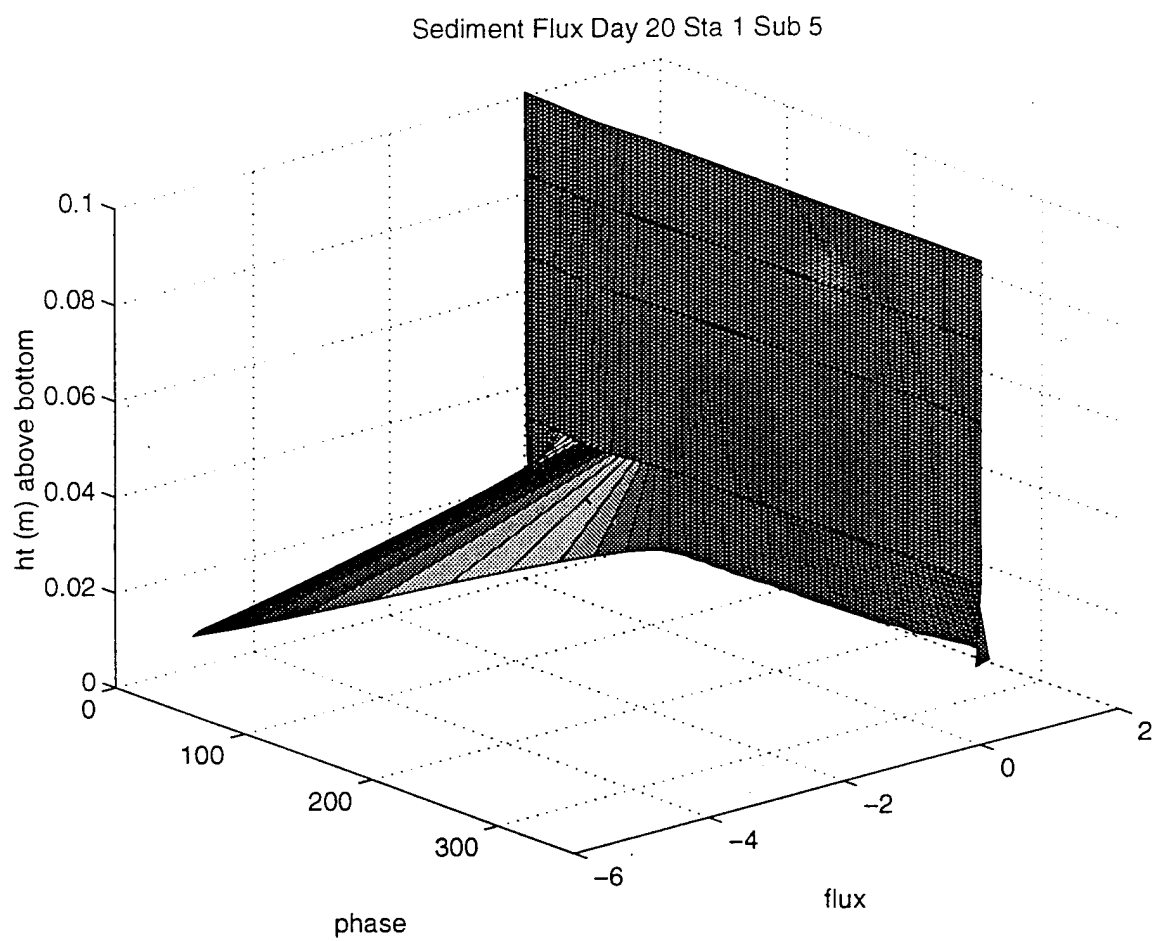


Figure 4.12 Phase space representation of sediment flux for substation 5 (intersection 0.05 m above sediment bed).

Substa	Height (cm)	Max (g/l)	Mean (g/l)	Beam 2 F5/F1	Beam 3 F5/F1	Beam 4 F5/F1
4	0	125.40	38.0	6.00	9.31	8.96
10	0	141.80	39.4	2.95	2.47	2.53
3	3.4	1.65	0.16	1.06	1.09	1.03
5	5.0	2.52	0.11	1.01	1.03	0.97
6	10.0	1.59	0.11	0.99	1.00	0.95
7	12.0	1.15	0.04	0.98	1.00	0.95

Table 4.2 F5/F1 ratios for Day 20, Station 1

Substa	Height (cm)	Max (g/l)	Mean (g/l)	Beam 2 F5/F1	Beam 3 F5/F1	Beam 4 F5/F1
2	0	127.10	18.01	927.01	2.40	2.38
6	3.4	15.72	1.04	1.88	2.03	1.90
3	5.0	1.37	0.20	1.96	1.94	1.82
4	10.0	1.52	0.38	2.38	2.37	2.23

Table 4.3 F5/F1 ratios for Day 20, Station 2

The F5/F1 values above the bed at Stations 1 and 2, where sediment conditions are well within those acceptable for discriminator performance, are notable for their consistency per station. Interpreted with Figure 3.30, these values indicate that the sediment seen at Station 1 is of a larger mean radius ( $>.1$  mm), and the suspended sediment at Station 2 is of a smaller mean radius ( $<.05$  mm), than that of the sand used for instrument calibration. This may be due to the higher wave energy level at Station 1 (bar) vs. Station 2 (trough), but

further investigation is required. Sediment at Station 2 also shows a general decrease in size with height, which is expected. Bubble entrainment differences would effect measurements from station to station, and work at the Naval Postgraduate School continues towards identifying and quantifying these effects.



## V. CONCLUSIONS

An empirical calibration of a Coherent Acoustic Sediment Profiler (CASP) has been performed with sediment sampled from the nearshore zone at Duck, N.C. The sediment is characterized by a lognormal distribution with a mean grain size diameter of 0.18 mm, and standard deviation of 1.2. The 1.3 MHz sonar measures sediment concentrations of  $O(1 \times 10^{-4} \text{ kg m}^{-3})$  to  $25 \text{ kg m}^{-3}$  at 10% accuracy. The 5.3 MHz sonar is similarly accurate for concentrations of  $O(1 \times 10^{-5} \text{ kg m}^{-3})$  to  $8 \text{ kg m}^{-3}$ . The high concentration limits,  $25 \text{ kg m}^{-3}$  and  $8 \text{ kg m}^{-3}$ , agree with previous semi-empirical work performed using similar frequencies and slightly smaller sand size (Sheng and Hay, 1988), and result from the onset of multiple scattering at the respective frequency. Estimation of the F5/F1 form factor ratio can be made by comparison of concentration measurements by both frequencies, and provides a grain size discrimination capability. This capability is accurate to within  $\pm 5\%$  of the F5/F1 ratio within the concentration and range limits of the 5.3 MHz beam.

The data storage bin map design and the effect of the partial inclusion of the test vessel window in the first bin for the 5.3 MHz beams were complicating factors for calibration. The bin map is being redesigned to minimize the number of blank storage bins in the string. To avoid the placement of the test vessel window partially within a bin, each beam should be calibrated separately. A real time analysis program has been implemented in the laboratory to allow more accurate positioning of the window bin for any beam with respect to the test vessel window.

Data from a day characterized by narrow banded waves and negligible longshore current during the DUCK94 experiment show that episodes of high sediment concentration correlate well with the maximum onshore velocities within 2 cm of the bottom, but decorrelate above this level. A phase mapping technique is used to create ensemble averages of velocity and concentration magnitudes. Four of these ensemble sets, consisting of values from 30 to 88 wave periods, are presented from a data collection station located on a smooth bottom on the shoreward slope of the offshore bar. All show the same strong correlation at the bottom bin,

and slightly different sediment patterns higher in the water column. Sediment flux calculations reveal strong shoreward transport at the boundary layer, and weaker seaward transport higher in the water column. The grain size discrimination indicates that the suspended populations differ at two of the data collection stations.

The CASP possesses additional capabilities to allow a more exhaustive analysis of the processes responsible for the sediment behavior presented here. Vertical velocities measured by the CASP are, as of this writing, corrected for any tilt of the CASP itself, but not for large and small scale bathymetry on which the sled might be resting. Currently, these measurements provide input for conceptual modeling, and will soon be available for more quantitative uses.

Reynolds stresses measured by the CASP will help model eddy viscosity and turbulence throughout the water column. Large and small scale bathymetry, which was recorded by the CRAB with side scan sonar and altimeter, and onboard the sled with a 675 KHz rotating side-scan sonar and a 2 MHz scanning altimeter, will allow for a more comprehensive analysis of ripple effects.

## LIST OF REFERENCES

- Faran, J.J.Jr., 1951, Sound scattering by solid cylinders and spheres. *J. Acoust. Soc. Am.*, 23, pp.405-418.
- Fisher, F.H., and Simmons, V.P., 1977, Sound adsorption in sea water, *J. Accoust. Soc. Am.*, 62(3), pp. 558-564.
- Fredsøe, J., 1993, Modeling of Non-Cohesive Sediment Transport Processes in the Marine Environment, *Coastal Engineering*, 21, 71-103.
- Fredsøe, J., Andersen, O.H., and Silberg, S., 1985, Distribution of suspended sediment in large waves, *J. Waterway, Port, Coastal and Ocean Eng. Div.*, ASCE, 111(6), 1041-1059.
- Fredsøe, J., and Deigaard, R., 1992, *Mechanics of Coastal Sediment Transport*, World Scientific Publishing Co. Pte. Ltd.
- Gaunard, G. C. , and H. Uberall, 1983, RST analysis of monostatic and bistatic acoustic echoes from an elastic sphere, *J. Acoust. Soc. Am.*, 73(1), 1-12.
- Hanes, D.M. and Huntley, D.A., 1986, Continuous measurements of suspended sand concentration in a wave dominated nearshore environment. *Continental Shelf Research*, 6, pp. 585-596.
- Hansen, E.A., Fredsoe, J., and Deigaard, R., 1994, Distribution of suspended sediment over wave generated ripples, *J. Waterw. Port Coastal Ocean Eng.* ASCE, (in press Jun 93).
- Hansen, E.A., Fredsoe, J., and Deigaard, R., 1991, Distribution of suspended sediment over wave generated ripples, *Int. Symposium on the Transport of Suspended Sediments and its Mathematical Modelling*, Florence, Italy, September 2-5, 1991, pp.111-128.
- Hay, A. E., 1991, Sound scattering from a particle-laden turbulent jet, *J. Geophys. Res.*, 90, 2055-2074.
- Hay, A. E., and D. G. Mercer, 1985, On the theory of sound scattering and viscous absorption in aqueous suspensions at medium and short wavelengths, *J. Acoust. Soc. Am.*, 78, 1761-1771.

Hay, A.E., and Sheng, J., 1992, Vertical Profiles of Suspended Sand Concentration and Size from Multifrequency Acoustic Backscatter, *Journal of Geophysical Research*, Vol. 97, No C10, p. 15,661-15,677.

Johnson, R. K., 1977, Sound scattering from a fluid sphere revisited, *J. Acoust. Soc. Am.*, 61(2), 375-377.

Justesen, P., and Fredsøe, J., 1985, Distribution of turbulence and suspended sediment in the wave boundary layer. *Progress Report No. 62, Inst. of Hydrodynamics and Hydraulic Engineering*,

Sheng, J., 1991, Remote determination of sediment size and concentration by multi-frequency acoustic backscatter, *PhD Thesis, Memorial University of Newfoundland, St. Johns, Canada*, 252 pp.

Sheng, J., and A. E. Hay, 1988, An examination of the spherical scatterer approximation in aqueous suspensions of sand, *J. Acoust. Soc. Am.*, 83, 598-610.

Stanton, T. P., 1993, The Coherent Acoustic Sediment Flux Probe (CASP), submitted to U. S. Army Corps of Engineers, Waterways Experiment Station.

Stauble, D. K., 1995, Personal communication, U. S. Army Waterways Experiment Station, Vicksburg, MS.

Tamura, T., and Hanes, D.M., 1986, Laboratory Calibration of a 3 Megahertz Acoustic Concentration Meter to Measure Suspended Sand Concentration, *University of Miami Rosenstiel School of Marine and Atmospheric Science Technical Report NO. 86-004*.

Thorne, P. D., C. E. Vincent, P. J. Hardcastle, S. Rehman, and N. Pearson, 1991, Measuring suspended sediment concentrations using acoustic backscatter devices, *Mar. Geol.*, 98, 7-16.

Thorne, P.D., P. J. Hardcastle, R. L. Soulsby, 1993, Analysis of acoustic measurements of suspended sediments, *J. Geophys. Res.*, 98 (C1), 899-910.

Young, R.A., Merrill, J.T., Clarke, T.L., Proni, J.R., 1982, Acoustic Profiling of Suspended Sediments in the Marine Bottom Boundary Layer, *Geophysical Research Letters*, Vol. 9, No 3, p. 175-178.



## INITIAL DISTRIBUTION LIST

1. Defense Technical Information Center ..... 2  
     Cameron Station  
     Alexandria, VA 22304-6145
  
2. Library, Code 52 ..... 2  
     Naval Postgraduate School  
     Monterey CA 93943-5101
  
3. Chairman, Department of Oceanography ..... 1  
     Code OC/Bo  
     Naval Postgraduate School  
     Monterey CA 93943
  
4. Timothy P. Stanton..... 3  
     Code OC/St  
     Naval Postgraduate School  
     Monterey CA 93943
  
5. Dr. Edward B. Thornton..... 2  
     Code OC/Th  
     Naval Postgraduate School  
     Monterey CA 93943
  
6. LCDR Karen M. Kohanowich ..... 2  
     PSC 473, BOX 68  
     FPO AP 96349-2902
  
7. Dr. Tom Kinder ..... 1  
     Coastal Sciences (Code 1121SS)  
     800 North Quincy Street  
     Arlington VA 22217
  
8. Dr. Tom White ..... 1  
     U. S. Army Corps of Engineers  
     Coastal Engineering Research Center  
     P.O. Box 631  
     Vicksburg MS 39180